

Manuel Auer, BSc

Studies of Novel Polymer and Dendrimer Materials for Application in Organic Light Emitting Devices

MASTER THESIS

For obtaining the academic degree
Diplom-Ingenieur

Master Programme of
Technical Physics



Graz University of Technology

Graz University of Technology

Supervisor:

Ao.Univ.-Prof. Dipl.-Ing. Dr.techn. Emil List-Kratochvil

Institute of Solid State Physics

Graz, October 2013

Deutsche Fassung:
Beschluss der Curricula-Kommission für Bachelor-, Master- und Diplomstudien vom 10.11.2008
Genehmigung des Senates am 1.12.2008

EIDESSTÄTTLICHE ERKLÄRUNG

Ich erkläre an Eides statt, dass ich die vorliegende Arbeit selbstständig verfasst, andere als die angegebenen Quellen/Hilfsmittel nicht benutzt, und die den benutzten Quellen wörtlich und inhaltlich entnommenen Stellen als solche kenntlich gemacht habe.

Graz, am

.....
(Unterschrift)

Englische Fassung:

STATUTORY DECLARATION

I declare that I have authored this thesis independently, that I have not used other than the declared sources / resources, and that I have explicitly marked all material which has been quoted either literally or by content from the used sources.

.....
date

.....
(signature)

Acknowledgement

I never thought this moment would come, but finally I can express my gratitude to everyone who helped me during my studies and especially during the time of my thesis!

First of all I want to thank my supervisor Emil J.W. List-Kratochvil, for giving me the possibility to write this thesis. He provided me with an interesting topic and a wonderful research opportunity at the NanoTec Center Weiz which allowed me to work together with extraordinary people. Also I want to thank him for the scientific support he gave me during this final part of my studies and for his patience if some result took a little bit longer than initially thought.

This work, however, would never have been possible without Roman Trattnig, my mentor and coworker. He always was on hand with help and advice and taught me almost everything I needed to know about OLEDs. Furthermore, I want to thank him for the many good advices in regard to scientific writing.

I also would like to thank my fellow lab rats Katrin Koren and Christoph Bauer for the many fruitful discussions we had and with whom I had lots of fun in the office as well as during the coffee breaks. Especially, I would like to thank Katrin Koren for being my secretary in the last months ;)! Furthermore, I want to express my gratitude to Michael Klemm for his assistance in performing the photophysical characterization of the dendrimer materials I received. Also, I want to thank the whole team at NanoTecCenter Weiz for all the help and support.

At this point I would also like to thank Christian Sommer and Heinz Pichler from Joanneum Research Materials who were on hand with help and advice for me when some of the equipment and installations once again failed on me or I failed on them. Also, I would like to thank Prof. Klaus Müllen, Guang Zhang and Leonid Pevzner from Max-Planck-Institute for Polymer Research, Mainz, Germany for providing the materials studied in this thesis.

I owe my deepest gratitude to my amazing girlfriend, Claudia Berger. She not only helped me to solve formulation problems, provided me with valuable comments and proofread my thesis, but more importantly provided me with moral support at every step of a sometimes difficult journey.

Last but by no means least, I want to express my deepest gratefulness to my family and my friends. Without them I would never have become the person I am today, would never have been able to see and experience what I have experienced and to achieve what I have achieved. Foremost, I would like to thank my family, especially my mother and my sister, for always supporting me in any possible way.

Abstract

The proliferation of consumer devices like smartphones and tablets brought the field of organic electronics its first noteworthy breakthrough in the form of Organic Light Emitting Diodes (OLED) employed in so called AMOLED displays. However, evaporation limits the display sizes which are commercially viable to those of smartphone applications. A possible solution for this problem is provided by roll-to-roll processing or inkjet printing, both of which fall into the category of solution-based processing. In order to reach commercial viability for solution-based processing, the manufacturing process itself and the organic semiconductors, especially the blue emitting ones which suffer from low lifetimes and efficiencies, still need to be improved. The aim of this thesis therefore is to address and to improve the two specified shortcomings in the field of blue OLEDs.

In the first part of this thesis it is attempted to do so by the application of dendrimers. Dendrimers are a special class of solution-processable materials, consisting of a high performance small-molecular core and different shell and surface groups. Detailed photophysical studies are carried out to reveal the impact of the different molecular assemblies on the absorption- and emission behavior. Finally, one of these dendrimers is optimized step by step in order to prove the usability of this promising material class in an efficient multi-layer device assembly.

Using polymers, another way of addressing the aforementioned shortcomings is presented in the second and in the third part of this thesis. The introduction of novel materials suitable for application in an orthogonal solvent approach – this effectively prevents the dissolution of preceding organic layers – enables a solvent based fabrication of OLEDs that also incorporate hole- and electron transport enhancing capabilities. The materials under investigation are polyfluorenes with perfluorinated- and pegylated side chain configurations, where the former is soluble in fluorinated solvents and the latter readily dissolves in polar solvents such as methanol. Photophysical properties are studied by means of absorption- and photoluminescence spectroscopy, while the suitability for application in OLEDs is determined by studying the performance in different device configurations.

Zusammenfassung

Das Forschungsgebiet der Organischen Halbleiter hat seinen ersten erwähnenswerten Durchbruch mit dem Aufkommen von Geräteklassen wie Smartphones und Tablets erlebt, in deren AMOLED Displays Organische Leuchtdioden (OLEDs) verbaut wurden. Allerdings limitieren heutige Aufdampfprozesse die wirtschaftlich realisierbaren Displaygrößen zu jener in der Größe von Smartphones. Eine mögliche Lösung für dieses Problem stellt die Verwendung von lösungsbasierten Verfahren in Form des Rolle-zu-Rolle Verfahrens oder des Inkjetdrucks dar. Doch auch diese erfordern für eine wirtschaftlich interessante Anwendung noch Verbesserungen im Bereich des Produktionsverfahrens und der organischen Halbleiter selbst. Dies gilt insbesondere im Fall der blau-emittierenden Halbleiter, welche bislang durch eine vergleichsweise niedrige Lebensdauer und durch geringe Effizienzen gekennzeichnet sind. Das Ziel dieser Arbeit ist es daher, die aufgeführten Defizite im Bereich der blauen OLEDs in Angriff zu nehmen und diese zu verbessern.

Im ersten Teil dieser Arbeit wird dies durch die Verwendung von Dendrimeren versucht. Dendrimere stellen eine spezielle Klasse von in Lösung verarbeitbaren Materialien dar, die sich aus einem leistungsstarken klein-molekularen Kern und verschiedenen Hüllen- und Oberflächengruppen zusammensetzen. Um den Einfluss verschiedener Molekülkonfigurationen auf das Absorptions- und Emissionsverhalten aufzuzeigen, werden detaillierte photophysikalische Untersuchungen durchgeführt. Zum Abschluss wird eines der Dendrimere schließlich Schritt-für-Schritt optimiert um die Verwendbarkeit dieser vielversprechenden Materialklasse in einem effizienten mehrschichtigen Aufbau zu belegen.

Im zweiten und im dritten Teil der Arbeit wird mit der Verwendung von Polymeren ein anderer Ansatz präsentiert um an die oben genannten Defizite der blauen OLEDs heranzugehen. Durch den Einsatz neuartiger Materialien, welche die Verwendung in orthogonalen Lösungsmitteln – diese verhindern ein Anlösen der vorhandenen organischen Schichten – zulassen, wird eine lösungsbasierte Herstellung von OLEDs mit eingebauten Loch- und Elektronentransport verbessernden Eigenschaften ermöglicht. Bei den untersuchten Materialien handelt es sich um Polyfluorene mit perfluorierten und pegylierten Seitenketten, wobei erstere in fluorierten Lösungsmitteln löslich sind und letztere sich leicht in polaren Lösungsmitteln, wie Methanol, auflösen. Die photophysikalischen Eigenschaften werden mittels Absorptions- und Photolumineszenz-Spektroskopie untersucht, während die Eignung für die Verwendung in OLEDs durch die Untersuchung der Leistung in verschiedenen Aufbauten eruiert wird.

Table of Contents

Acknowledgement	3
Abstract	4
Zusammenfassung	5
Table of Contents	6
Abbreviations	8
1 Introduction.....	11
2 Fundamentals.....	12
2.1 Organic Semiconductors	12
2.1.1 Small Molecules	13
2.1.2 Polymers	14
2.1.3 Dendrimers.....	16
2.2 Excited States and Recombination Dynamics	17
2.2.1 Polarons	18
2.2.2 Excitons.....	18
2.3 Basic Optical Processes in Organic Semiconductors	19
2.3.1 Photoluminescence	23
2.3.2 Electroluminescence	23
2.4 Charge Transport.....	23
2.5 Energy Transfer	24
2.5.1 Förster Transfer.....	25
2.5.2 Dexter Transfer	26
3 Working Principle of OLEDs	28
3.1 Interfaces between Metal and Organic Compounds.....	30
3.1.1 Metal-Organic Interfaces	30
3.1.2 Organic-Organic Interfaces.....	31
3.2 Charge Injection.....	32
3.2.1 Ohmic Contact.....	32
3.2.2 Injection Limited Contact	32
3.3 External Quantum Efficiency	33
4 Experimental Methodology	36
4.1 Sample Preparation	36
4.1.1 Substrate preparation	36
4.1.2 Layer Deposition	36
4.1.3 Electrode deposition	37
4.2 Photophysical Characterization	37
4.2.1 Absorption Measurements.....	37
4.2.2 Photoluminescence Measurements.....	38
4.2.3 PLQY Measurements	38
4.3 Device Characterization	39

Table of Contents

4.3.1	Current Density-Voltage-Luminescence Characterization.....	39
4.3.2	EL Spectra of OLEDs	39
4.3.3	Pulsed Characterization	40
4.4	Layer Characterization	40
5	Structure to Property Relationships in Pyrene Cored Dendrimers.....	41
5.1	Investigated Dendrimers	42
5.2	Photophysics of dendrimers	45
5.2.1	Effect of Different Surface Groups on the Absorption and Emission Profile	46
5.2.2	Effect of Different Shell Configurations on Photophysical Properties	49
5.2.3	Type of Energy Transfer	52
5.3	Performance of PYTPAG1 in a Device.....	56
5.4	Optimization of PYTPAG1	57
5.4.1	HIL Optimization.....	57
5.4.2	HTL Optimization.....	60
5.4.3	ETL Optimization.....	63
5.4.4	Cathode Optimization	65
5.4.5	Formation of Agglomerates	67
5.4.6	Optimization of PYTPAG1 - Summary	67
5.5	Conclusion	69
6	Polyfluorenes with Linear and Branched Semiperfluorinated Side Chains	70
6.1	Motivation and Investigated Compounds.....	71
6.2	Properties of PFO	72
6.2.1	Photophysical Properties	72
6.2.2	Device Performance	72
6.3	Photophysical Characterization	73
6.4	Wettability and Orthogonal Processing.....	76
6.5	Fluorinated PF as Active Layer in OLEDs	80
6.6	Charging Effects as Source for Spectral Instabilities	82
6.7	Conclusion	83
7	Investigations on Pegylated Polyfluorene	85
7.1	Photophysical Characterization	85
7.2	Device Characteristics in a Single Layer Assembly.....	86
7.3	Bilayer devices.....	87
7.3.1	Origin of the Current Density Dependent Change of the Emission Behavior.....	88
7.3.2	Factors that Impact the Location and Movement of the Recombination Zone	90
7.3.3	Consequence of the Movement of the Recombination Zone.....	93
7.3.4	Bilayer devices - Summary	93
7.4	Voltage Dependent Color Tuning	94
7.4.1	Orange – Blue Emitting PPDB Blend Systems	95
7.4.2	Red-Blue Emitting PtOEP Blend Systems	100
7.5	Conclusion	105
8	Conclusion.....	106
9	References.....	108

Abbreviations

ADS	American Dye Sources INC.
ADS129BE	Poly[9,9-dioctylfluorenyl-2,7-diyl] - End capped with Dimethylphenyl
ADS232GE	Poly[(9,9-dioctylfluorenyl-2,7-diyl)-co-(N,N'-diphenyl)-N,N'-di(pbutylphenyl)-1,4-diamino-benzene)]
AFM	Atomic Force Microscope
Ag	Silver
Al	Aluminum
Au	Gold
BPhen	Batho-phenanthroline
Ca	Calcium
CAB	Carbazole
CB	Conduction Band
CBP	4,4'-Bis(N-carbazolyl)-1,1'-biphenyl
CCD	Charge-Coupled Device
C ₆ F ₆	Hexafluorobenzene
CIE1931	Comission Internationale de l'Eclairage standard of 1931
Cs	Cesium
Cs ₂ CO ₃	Cesium Carbonate
CsCl	Cesium Chloride
CsF	Cesium Fluoride
CsF ₂	Cesium Difluoride
DLED	Dendrimer Light Emitting Diode
DMSO	Dimethyl Sulfoxid
EG	Ethylene Glycol
EL	Electroluminescence
EIL	Electron Injection Layer
EML	Emissive Layer
ETL	Electron Transport Layer
fPF	Fluorinated Polyfluorene
FRET	Förster Resonance Energy Transfer
FWHM	Full Width Half Maximum
HC	High Conductive
HCl	Hydrochloric Acid
HOMO	Highest Occupied Molecular Orbital
HIL	Hole Injection Layer
HTL	Hole Transport Layer

Abbreviations

ID	Interface Dipole
ISC	Inorganic Semiconductors
ITO	Indium-Tin-Oxide
J-V-L	Density-Voltage-Luminescence
LCD	Liquid Crystal Display
LiF	Lithium Fluoride
LUMO	Lowest Unoccupied Molecular Orbital
MeOH	Methanol
MgF ₂	Magnesium Fluoride
MM2	Second Generation Force Field
MPI	Max-Planck Institute of Polymer Research
NaCl	Sodium Chloride
NPA	N-phenyl-naphthaleneamine
OLED	Organic Light Emitting Diode
OX	Oxadiazole
PEDOT	Poly(3-4-ethylenedioxythiophene)
PEG	Poly(ethylene glycol)
PEGPF	Polar Soluble Polyfluorene
PF	Polyfluorene
PFO	Poly(9,9-dioctylfluorene)
PL	Photoluminescence
PLEXCORE	PLEXCORE OC RG-1100
PLQY	Photoluminescence Quantum Yield
PPDB	Poly(perylene-co-diethynylbenzene)
PSS	Poly(styrenesulfonate)
Pt	Platinum
PtOEP	Platinum(II) 2,3,7,8,12,13,17,18-octaethyl-21H,23H-porphyrin
PVK	Poly-(N-vinyl carbazole)
PYCAB	Pyrene cored dendrimer with one generation of polyphenylenes and CAB as surface groups
PYNPA	Pyrene cored dendrimer with one generation of polyphenylenes and NPA as surface groups
PYDTPAG1	Pyrene cored dendrimer with one generation of polyphenylene and two generations of TPA as surface groups
PYOXA	Pyrene cored dendrimer with one generation of polyphenylenes and OXA as surface groups
PYTPAG1	Pyrene cored dendrimer with one generation of polyphenylenes and TPA as surface groups

Abbreviations

PYTPAG2	Pyrene cored dendrimer with two generations of polyphenylenes and TPA as surface groups
PYTPG2	Pyrene cored dendrimer with two generations of polyphenylenes and TP as surface groups
PYTPG3	Pyrene cored dendrimer with three generations of polyphenylenes and TP as surface groups
SD	Surface Dipole
TFB	Poly[(9,9-dioctylfluorenyl-2,7-diyl)-co-(4,4'-(N-(p-butylphenyl))diphenylamine)]
THF	Tetrahydrofuran
TP	Triphenylene
TPA	Triphenylamine
TPBi	1,3,5-tris(2-N-phenylbenzimidazolyl)-benzene
TTP	Triphenyltriphenylen
UPS	Ultraviolet Photoelectron Spectroscopy
UV/VIS	UV Visible Spectroscopy
VB	Valence Band
(x,y)	CIE1931 coordinates x = ..., y = ...

1 Introduction

Organic light emitting diodes (OLED) have come a long way since the first successful demonstration of a thin film light emitting diode based on small molecules in 1987 by Tang et al.¹. Only three years later Burroughes et al.² demonstrated the viability of polymers for OLED applications. These discoveries led to a literal explosion of research interest in the field of organic semiconductors for display and lighting applications which ultimately led to the successful commercialization of organic semiconductors for this sector³. While at the time of the writing of this thesis the market for display technologies is still dominated by liquid crystal displays (LCDs), it is projected that OLEDs will experience significant growth over the course of the next years⁴. The driving forces behind increasing the percentage of OLEDs on the display market are on the one hand the possibility to employ low priced large-scale production technologies, such as roll-to-roll processing or inkjet printing, and to a lesser extend also wide viewing angles, high brightness, an impressive contrast ratio and fast response times offered by this display type. While organic semiconductors provide all these benefits, some drawbacks are still holding this technology back. Among those are the still rather poor performance of blue emitters with regard to life time and efficiency as well as the lagging performance of solution processed displays that are producible either via roll-to-roll processing or inkjet printing.

Consequently, there is a significant research interest in the field of solution processable organic light emitting devices, especially with regards to the realization of a cheap- and reliable way to manufacture solution processed OLEDs. Since the improvement or invention of a low priced large-scale production process was beyond the scope of this master thesis, it was attempted to improve the performance of solution processed OLEDs. This was done by the introduction of new materials that either allow the deposition of multiple layers without dissolving the preceding ones or are based on a new architecture that allows for increased performance.

After the depiction of the related theoretical background in the first chapters followed by the research methodology, a special approach for solution processable materials is demonstrated in chapter 5. Named dendrimer, this material class is studied by means of several different molecular configurations. Detailed photophysical examinations are accompanied by the successive improvement of one of these dendrimers via adding hole- and electron transporting layers as well as optimized hole- and electron injection layers. Following that, the suitability of several fluorinated polyfluorenes (fPF) for application in a solution processed OLED is studied and presented in chapter 6. This also includes the detailed examination of photophysical properties and the investigation of the suitability of the studied polymers in a solution based multi-layer device. Finally, in chapter 7, bilayer systems consisting of a hole-transport polymer and a pegylated polyfluorene (PEGPF) are investigated with regards to the possibility to tune the emission color depending on the applied voltage.

2 Fundamentals

2.1 Organic Semiconductors

Carbon constitutes the basic building block for organic semiconductors. The atomic shell of carbon consists of six electrons, two are located in the inner K-shell and the remaining four in the outer L-shell. In the ground state, obeying Hund's rule and Fermi's exclusion principle, two electrons are paired in the 2s orbital and the remaining two are located in the p_x and p_y orbital, cumulating in the electron configuration ($1s^1 2s^2 2p_x^1 2p_y^1$). When the ground state becomes perturbed, for example by the proximity of another carbon atom, the shape of the orbitals becomes perturbed as well. Therefore, the energy associated with the respective orbital changes. The first description of this reconfiguration upon a perturbation was given by Pauling (based on the Molecular Orbital Theory (MO) ⁵) as a mixing of atomic orbitals which results in the formation of new hybrid orbitals of equal energy ⁶. This explanation is commonly referred to as hybridization. Depending on the amount of participating p orbitals, different types of hybridization are possible. In terms of organic semiconductors, only sp^2 -hybridization is important and, therefore, detailed explanations of the sp^1 - and sp^3 hybridization mechanisms are omitted. In sp^2 -hybridization two of the three p-orbitals are involved and arrange themselves, as depicted in Figure 2.1, symmetrically in one plane. The remaining p-orbital (also referred to as p_z -orbital) is oriented perpendicular to this plane. The sp^2 -orbitals are able to form strong and highly directed covalent bonds at an angle of 120° . The remaining p_z -orbital is also able to interact with other p_z -orbitals depending on the overlap between these orbitals.

In that context it is important to note that hybridization can only be found in molecules and not in single atoms, since the necessary energy for the formation of the hybridized orbitals is gained from the, in general, very strong and directed bonds with other atoms.

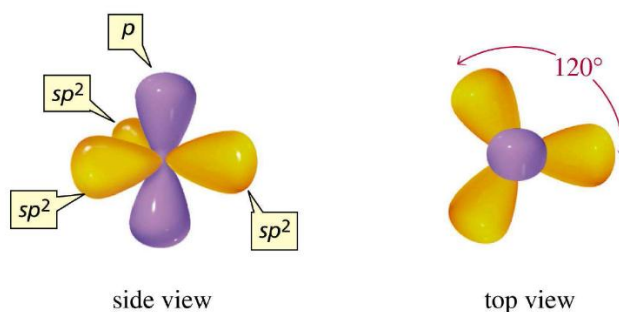


Figure 2.1: Side and top view of the hybrid orbitals resulting from the sp^2 hybridization of carbon (taken from Ref ⁷)

The described sp^2 -hybridization enables conjugated small molecules and conjugated polymers to exhibit the desired semiconducting properties. Besides these two material classes, dendrimers^{8,9} – a hybrid between small molecules and polymers – gained attraction among the science community. These three classes are presented in more detail in the following subchapters.

2.1.1 Small Molecules

The class of small molecules is going to be explained on the basis of benzene which consists of six interconnected carbon atoms (see Figure 2.2). Bonding between the individual carbon atoms is established through sp^2 -hybridized states of the carbon atoms at an angle of 120° .

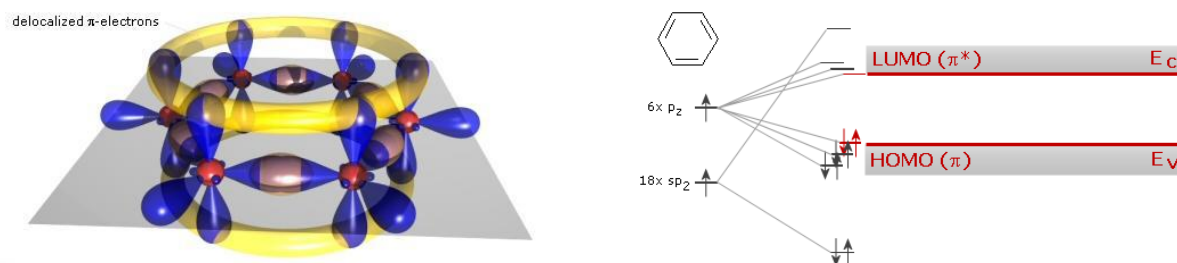


Figure 2.2: Schematic visualization of σ - and π -orbitals prevalent in benzene (left) and schematic energy level structure of benzene (taken from Ref¹⁰).

According to MO-theory, the molecular orbitals (MOs) are representable by a linear combination of the respective atomic orbitals. Therefore, the combination of the atomic s- and p_z -orbitals leads to the formation of bonding (σ , π) and antibonding (σ^* , π^*) orbitals (see Figure 2.3). The distribution of the electrons in these MOs has to follow Pauli's law and, therefore, two electrons with antiparallel spin can occupy one MO. Since every carbon atom in benzene contributes three electrons to the formation of σ -bonds and one electron that forms π -bonds, 12 σ -orbitals and 3 π -orbitals are filled. The respective antibonding σ^* - and π^* -orbitals remain unpopulated. As depicted in Figure 2.3, the π -orbitals exhibit a lower binding energy and as a result are located at higher absolute energy values than the σ -orbitals. In contrast, the antibonding σ^* -orbital is energetically higher than the π^* -orbital in terms of absolute energy. Consequently, the π - and π^* -orbitals represent the highest molecular orbital (HOMO) and the lowest molecular orbital (LUMO), respectively. Importantly, the individual π - and π^* -orbitals are associated with different energies. This causes larger molecular systems to develop band like structures where the bonding- and antibonding orbitals approximate the conduction- and valence band structures in inorganic semiconductors. Semiconducting properties arise from the existence of a band gap, since no partially filled bands exist in benzene, and from the presence of band like structures¹¹. The size of the band gap, in other words the size of the energy difference between the HOMO and the LUMO, is directly influenced by the amount of

participating atomic p_z -orbitals and therewith by the extend of the delocalization of the π -electrons. This means that stronger delocalization results in the appearance of more individual π - and π^* -orbitals within the band gap, causing the band gap to shrink. One effective way to lower the band gap of small molecules is to link two benzene rings covalently so that their π -systems overlap.

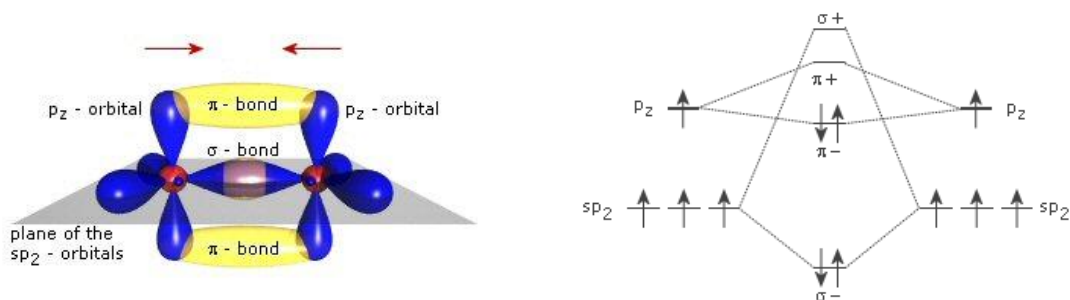


Figure 2.3: σ - and π -bonds exemplified in plane of the sp^2 orbitals of two carbon atoms (left) as well as a qualitative representation of the binding energies of the respective MOs (taken from Ref ¹⁰)

2.1.2 Polymers

Polymers are large molecules with high molecular weight composed of numerous – 10^2 to 10^5 – linked repeating carbohydrate units, called monomers. If a polymer consists of only one type of monomer it is called a homopolymer, while copolymer is the proper term when the polymer consists of at least two types of monomers. The amount, the structure and the arrangement of the monomers governs important chemical and physical parameters like solubility, polarity, glass transition temperature and so forth. Therefore, the properties of a polymer can be influenced by changing the structure of the monomers or by the attachment of side chains to the monomer units. Concerning this thesis, side chains will turn out to be crucial in regard to the solubility of the polymer.

Like in conjugated small molecules, bonds formed in conjugated polymers are the result of the overlap between the sp^2 -orbitals of neighboring carbon atoms. Electrons not participating in the highly directional σ -bond, participate in bonding in the form of overlapping p_z orbitals as π -bonds. The delocalization observed in the case of small molecules takes place in polymers as well and in ideal polymers (infinite in size and perfect in structure) even stretches across the whole polymer chain. As a rule of thumb it can be stated that the more electrons are taking part in this delocalized π electron cloud, the smaller the band gap becomes (see Figure 2.4). At an energy density high enough, the highest occupied bonding π -orbital and the lowest unoccupied antibonding π^* -orbital merge into one continuous and half-filled orbital and, therefore, metallic behavior can be expected. While simpler theories, like the free electron

molecular orbital model where all π -electrons are located in a one-dimensional box, also yield a merging of the HOMO and the LUMO at a certain amount of participating π -electrons, experiments were unable to find metallic behavior in large conjugated polymers such as polyparaphenylene or polythiophene ¹².

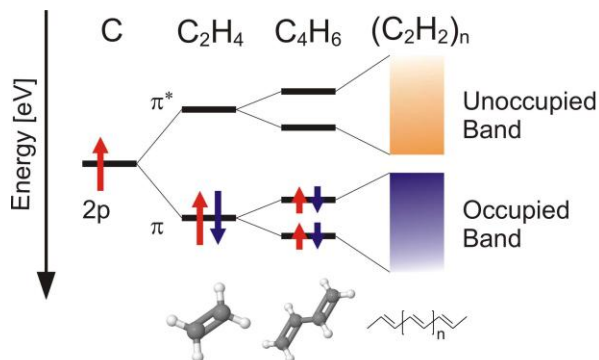


Figure 2.4: Evolution from discrete energy levels to a band like structure starting from a single carbon all the way to polyacetylene (taken from Ref ¹³)

The reason why only insulating- or semiconducting behavior was found in these polymers is the Peierls transition, an effect named after R. Peierl who showed that a 1D atom chain is more stable when the spacing between these atoms alternates between longer and shorter distances at low temperatures ¹⁴. The result is a transition from metal to insulator. Indeed, this alternation in bonding length formed by alternating double and single bonds was found for polyacetylene ¹⁵. The result of the alternation is demonstrated in Figure 2.5 where the formation of two bands separated by an energy gap is observable when the Peierls transition is considered.

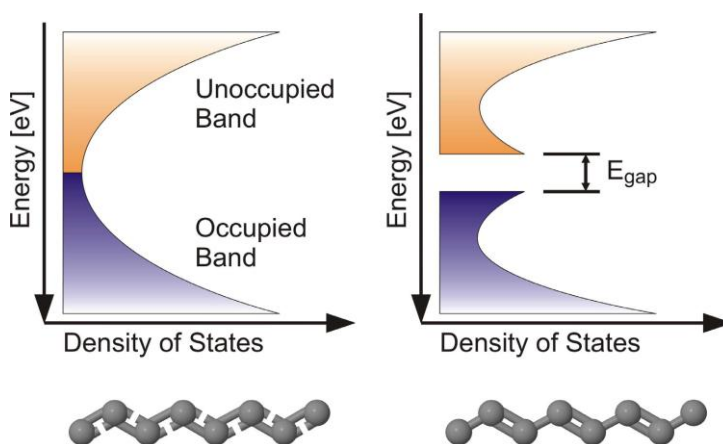


Figure 2.5: Band structure of polyacetylene with (right) and without (left) the Peierls distortion taken into account (taken from Ref ¹³)

So far, the evolution of the band structure and the band gap was considered in the case of an ideal polymer. Real polymers, however, can contain impurities added on purpose or as a contamination during the synthesis. Furthermore, in case of ideal polymers the structure was assumed to be free from any kinks, bends or twists. Also, possible steric hindrance as a consequence of electrostatic repulsion between two molecular segments was excluded. All these perturbations can severely restrict the above mentioned delocalization of the π -electrons to segments of different conjugation length. Consequently, it is reasonable to introduce a quantity called effective conjugation length, which is the average of the different conjugation lengths.

2.1.3 Dendrimers

Small molecules benefit from relatively easy to understand structure-to-property relationships and, due to their small size, the constraint of being monodisperse is inherently satisfied. At the same time, however, solution processability in general ¹⁶ as well as operational stability, being severely impacted by lower glass transition temperatures ¹⁷, are severe drawbacks of this otherwise promising material class. High glass transition temperatures as well as solution processability are, however, a major and inherent advantage of organic materials belonging to the class of conjugated polymers. Unfortunately, controlling the polydispersity, molecular weight and the amount of backbone defects of conjugated polymers often represents a major obstacle. Additionally, more complicated structure-to-property relationships cause the class of conjugated polymers to continuously lag behind small molecules in terms of performance.

Dendrimers combine the advantages of small molecules and conjugated polymers. They are branched macromolecules which are readily soluble and therefore solution processable, while the dendritic architecture allows for independent control of processing and optoelectronic properties ¹⁸. These advantageous properties arise from the stepwise generation-by-generation growth that enables controlled synthesis of highly defined three-dimensional shape persistent structures comprised of functional molecular units at defined positions ¹⁸. To synthesize dendrimers suitable for application in light emitting diodes, which then are called Dendrimer Light Emitting Diodes (DLEDs), properties like photoluminescence quantum yield (PLQY), emission color, stability as well as the ability to facilitate charge carrier injection, need to be tuned. Charge carrier injection and capture is usually enabled by adding redox-active moieties to the surface, while also placing a chromophore in the core of the dendrimer (schematically depicted in Figure 2.6) ^{19,20}. Additionally, due to the spherical nature of the molecule, the chromophore can be effectively shielded, allowing efficient emitters of the small molecule class like pyrene ²¹ to be utilized. The redox-active moieties and the chromophore at the center of the dendrimer constitute a donor - acceptor system (see chapter 2.5.1) that can be fine-tuned by choosing appropriate moieties on the surface to display an efficient molecular

energy transfer from the surface to the core. That way, control over the emission color and high PLQY are achievable²². At the same time, the shell of the dendrons can provide high solubility without the addition of further side chains²³.

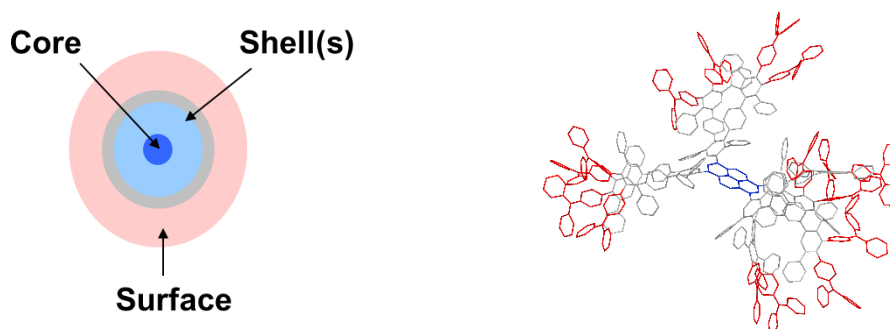


Figure 2.6: Schematic representation of the structure of dendrimers (left) and PYTPAG2 a pyrene cored dendrimer (right)

2.2 Excited States and Recombination Dynamics

To understand the physics of organic semiconductors it is useful to first take a look at inorganic semiconductors (ISC) and then to compare them to the physical realities present in their organic counterparts. In ISCs, electronic and electro-optical processes are the direct result of the excitation of an electron from the valence band (VB) into the conduction band (CB). The same is true for organic semiconductors. However, where these two material classes start to diverge is in the way the charge carriers interact with the lattice they are located in. ISCs exhibit a three dimensional lattice in which electrons promoted to the CB are able to move freely without causing significant distortions to their host lattice. In contrast, it is usually impossible to assign a periodic lattice structure to organic semiconductors. Instead, the delocalization of the π -system usually only extends over a single molecule or in some cases via interactions to neighboring molecules²⁴. Furthermore, as opposed to ISC, organic semiconductors are subject to pronounced electron-lattice (in this case lattice refers to the individual organic molecule) interactions as a result of the induced changes of the electronic potential of the molecule upon excitation. As a consequence of the changed electronic configuration and electronic potential, the atoms in the molecule undergo a structural relaxation in order to achieve an energetically favorable configuration.

Hence, the excited states in an organic semiconductor, in contrary to their ISC counterparts which are for the stated reasons highly delocalized, exhibit a more or less pronounced localization and are not able to move freely through the material²⁴. Consequently, excited states in organic semiconductors are described as quasi-particles that consist of the localized excitation and the resulting structural distortion. The two for this thesis most important quasi particles, the polaron and the exciton, are detailed in the following subchapters.

2.2.1 Polarons

Removing a charge carrier from the HOMO or adding one to the LUMO of a molecule causes the molecule to change its molecular structure in accordance to the changed electrostatic potential. The resulting structural relaxation causes the HOMO or the LUMO of the monomer where the polaron is located to shift into the region of the band gap. Usually, this relaxation does not extend far beyond (a few monomer units) the location where the charge carrier was added or removed. Therefore, it is useful to introduce a quasi particle that takes the observed distortion into account. In case an electron is added, the associated quasi particle is termed as a negative polaron, while the removal of an electron is associated with a positive polaron. In general, positive- and negative polarons are called holes and electrons, respectively.

A special form of polaron is the bipolaron, where two polarons reside on the same conjugated molecule. Even though two charges with the same sign would repulse each other, the formation of a pair of charges can be energetically favorable. A bipolaron causes similar but more extended deformations as a single polaron. The progression of the energy shift the HOMO and LUMO levels experience is depicted qualitatively in Figure 2.7.

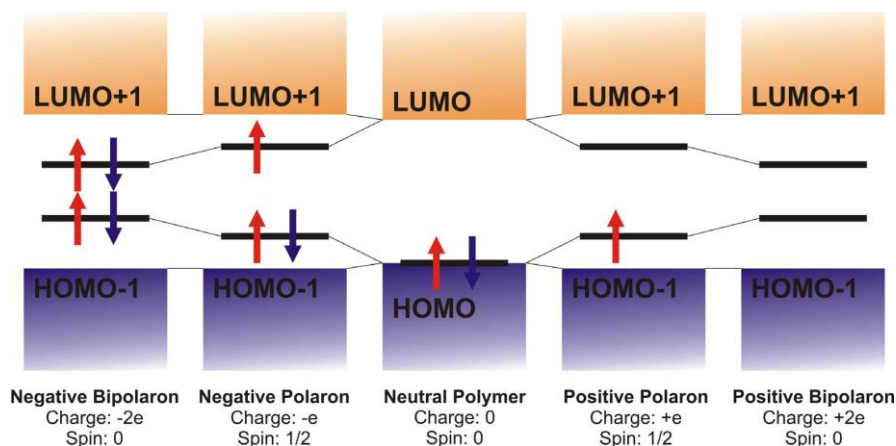


Figure 2.7: Typical polaron states in conjugated materials (taken from Ref ¹³)

2.2.2 Excitons

Excitons are neutral excited states that appear in the electronic system of a conjugated organic material. They form a neutral entity that consists of an electron-hole pair bound by Coulomb interaction (Coulomb-correlated electron-hole pair). Two exciton formation processes are possible. Firstly, an electron can be promoted from the HOMO to the LUMO upon photoexcitation thereby creating a hole in the LUMO. These two charge carriers are then bound by the Coulomb force and form the aforementioned neutral exciton. Secondly, after injection from the electrodes and a subsequent charge transport, positively and negatively charged polarons can form electron-hole pairs due to the Coulomb interaction.

Depending on the interaction range, two types of excitons exist, namely the Frenkel and the Wannier excitons. The former has a small radius and, therefore, usually resides on one monomer unit. The binding energies of this type of excitons are in the range of 1 eV. Wannier excitons are more delocalized with a radius often larger than the size of an individual monomer. Compared to the Frenkel excitons, the binding energies are quite low with only about 0.1 eV. A property both types of excitons share is the ability to have a total spin of the electron-hole pair of 0 or 1. In case that the total spin equals 0, the total spin wave function is antisymmetric and the exciton possess an anti-parallel spin arrangement. Consequently, it is termed singlet exciton. If the total spin equals 1, the spin wave function is symmetric. The resulting exciton is then called a triplet exciton based on the three-fold degeneration of the magnetic moment. Both types of excitons are demonstrated schematically in Figure 2.8.

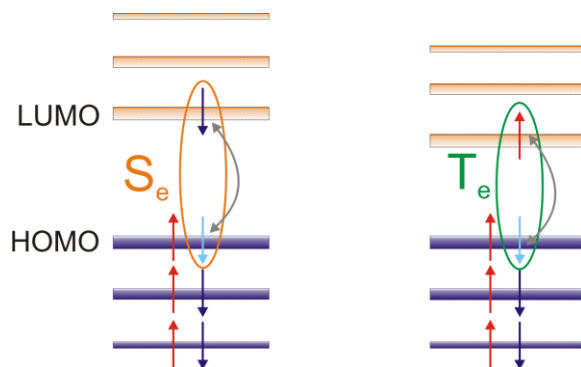


Figure 2.8: Singlet excitons (left) and triplet excitons (right). The arrows indicate the spin orientation (taken from Ref ²⁵)

2.3 Basic Optical Processes in Organic Semiconductors

It is known that electronic transitions between the π - π^* gap is accompanied by a change in the structural disorder of the atoms in organic semiconductors. The electronic transition usually takes place within a timescale of femtoseconds (10^{-15} s), while the atomic structure needs about 10^{-13} s to respond to the change of the electronic state. This difference in timescale is commonly exploited in quantum mechanics where the Born-Oppenheimer approximation is employed to describe a process where multiple particles with different transition timescales are involved. Hence, an electronic transition can be considered as a two-step process: First, the electron wavefunction is determined under the condition that the atomic nuclei of the molecule are fixed. Subsequently, the change of the position of the nuclei caused by the change in the electronic configuration is evaluated using the average potential of the electron distribution. According to the basic working principles of organic semiconductors, transitions between the π - π^* - or HOMO-LUMO transitions always involve antibonding π^* -states, which increase the bonding length in comparison to the π -states as a consequence of their

antibonding character and, in turn, result in elevated equilibrium distances for the nuclei. As a result, the potential energy curves associated with the ground- and excited states display an offset with respect to their spatial position, commonly associated with a configurational coordinate. These potential curves for the ground- and excited state and their respective equilibrium configuration coordinates $Q_0^{(0)}$ and $Q_0^{(1)}$ are depicted in Figure 2.9.

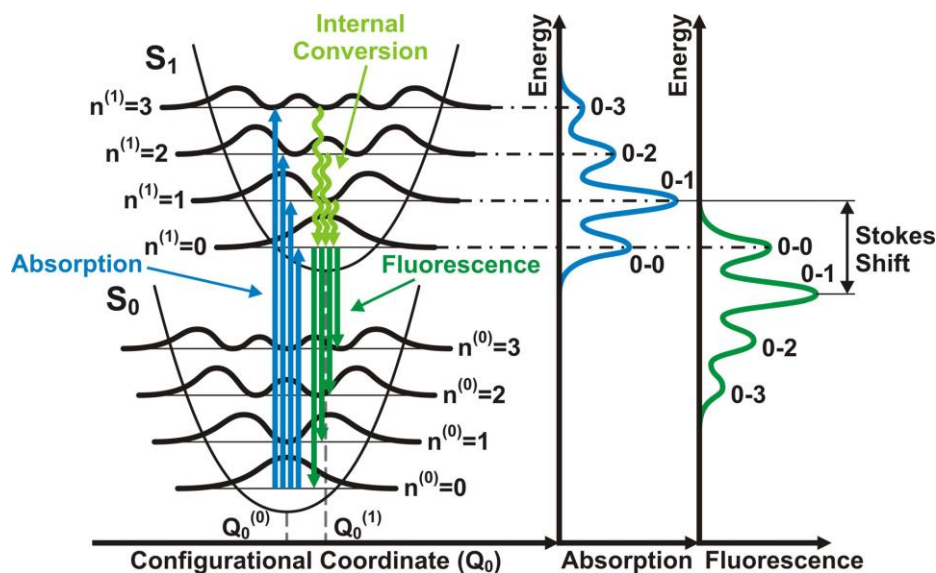


Figure 2.9: Schematic of the transition possibilities between different vibronic levels of the singlet ground state and the first excited singlet state as well as the corresponding absorption and emission spectra (taken from Ref ¹³)

An accurate description of the excitation- or deactivation processes is possible via the Franck-Condon-principle ^{26,27}, which takes the different equilibrium distances as well as the difference in timescales for excitation and atomic rearrangement into account. Hence, electronic transitions are in most cases coupled to vibrational modes of the molecule ²⁸. The energy difference between two vibrational levels is usually in the range of 0.1 eV. According to $E = k_B T$, where k_B is the Boltzmann's constant and T is the temperature, 1200 K are required to populate $n^{(0)} = 1$. Consequently, electronic transitions of an electron from the lowest vibrational state can also populate higher lying vibrational states in the final electronic state as depicted by the blue lines in Figure 2.9. The intensity of an individual transition is described by the Franck-Condon factor which is proportional to the absolute square of the overlap integral of the participating wavefunctions. The coupling between the electronic- and vibrational transitions is dependent on the displacement of the atoms in the beginning compared to the final state and can be described by the Huang-Rhys factor S ²⁹

$$S = \frac{1}{2} \frac{M\omega^2}{\hbar\omega} (Q_n^{(0)} - Q_n^{(1)})^2 = \frac{\Delta E}{\hbar\omega} \quad (2.1)$$

Here M represents the effective mass, $\hbar\omega$ is the transition energy and $Q_n^{(0)}$ and $Q_n^{(1)}$ describe the corresponding coordinates of the starting- and the final states. ΔE is the energy difference between the main vibrational state of the final state and the lowest vibrational state of the starting state. Obviously, when the molecule shows no structural reconfiguration, the strongest transitions are from a vibrational ground state to a vibrational ground state. Significant displacements, however, shift the transitions from the vibrational ground state to higher lying states, which causes pronounced sidebands to appear in the spectra. Therefore, a large S is observed for molecules that exhibit a high degree of freedom with regards to deformation. Following the transition, the molecule relaxes to the lowest vibrational state (Kasha's rule³⁰) in a process commonly referred to as internal conversion (IC).

The above described processes are now considered on the basis of a molecule in the lowest vibrational state of the ground state. An incident photon with an energy above the bandgap is absorbed and promotes an electron from an occupied π -orbital to an unoccupied π^* -orbital, thus lifting the molecule to a higher vibrational level of the excited state. It should be noted that the ground state is a singlet state with a total spin of zero. Therefore, according to spin selection rules for optical transitions that dictate that the total spin must be conserved ($\Delta S = 0$), only singlet states can be generated by the absorption of photons. After the excitation, a relaxation to the lowest vibrational state takes place via internal conversion at timescales typically in the range 10^{-12} - 10^{-13} s. From this level, after an average lifetime of 10^{-9} s, a relaxation back to a vibrational level of the ground state can take place either by emitting the excess energy as a photon (fluorescence) or by a non-radiative decay path where the excess energy is converted into a phonon. In case a photon is emitted, it is obvious that due to IC, a difference in energy between the absorbed- and emitted photon exists. It is noticeable as a shift of the absorption- and emission maxima which is known as the Stokes shift³¹. From these considerations, the absence of a Stokes-shift for molecules with predominating transitions between the vibrational ground states of the electronic ground- and excited state is evident.

Finally, it should be noted that many organic semiconductors exhibit a similar potential in the S_0 and S_1 state and, therefore, show a mirror symmetry between the absorption- and emission spectra. In some cases, however, this mirror symmetry becomes blurred or even vanishes completely when torsional freedom between individual conjugated segments exists. A good example for a broken mirror symmetry are oligo- or poly(para-phenylene)s and polyfluorene (PF)³². Besides the aforementioned transition process, which due to the prevalent spin selection rules only allowed transitions in the singlet-manifold to take place, a transition to the triplet-manifold is also possible via intersystem crossing (ISC) (see Figure 2.10). While the transition probability is not zero, the radiative transition from an excited triplet state to the ground state is nonetheless forbidden by the aforementioned spin selection rules. Thus, the deactivation of the formed triplet-excitons has to occur by means of non-radiative

recombination where the excitation energy is converted into phonons. One way to alleviate the spin selection rules is by means of strong spin-orbit coupling which in organic semiconductors can be induced by the incorporation of heavy metal atoms like platinum, iridium, or bromine³³⁻³⁵. While these semiconductors feature significant radiative decay from the triplet- to the ground-state (phosphorescence), the average lifetime of the triplet-state is much higher (10^{-6} - 10^{-3} s) than the lifetime commonly observed for singlet states (10^{-9} s).

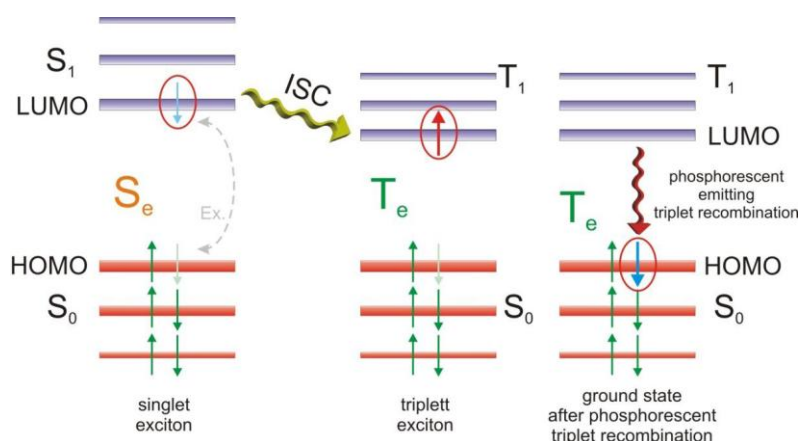


Figure 2.10: Generation of a triplet exciton via intersystem crossing (taken from Ref³⁶)

The described optical processes can be represented graphically as seen in Figure 2.11, which is a so called Jablonski diagram³⁷. This diagram schematically depicts the energetics and the vibrational levels of the different possible singlet- and triplet states, as well as the possible transition processes. S_n and T_n represent the respective singlet- and triplet manifolds, where the index n labels the individual states within the manifold.

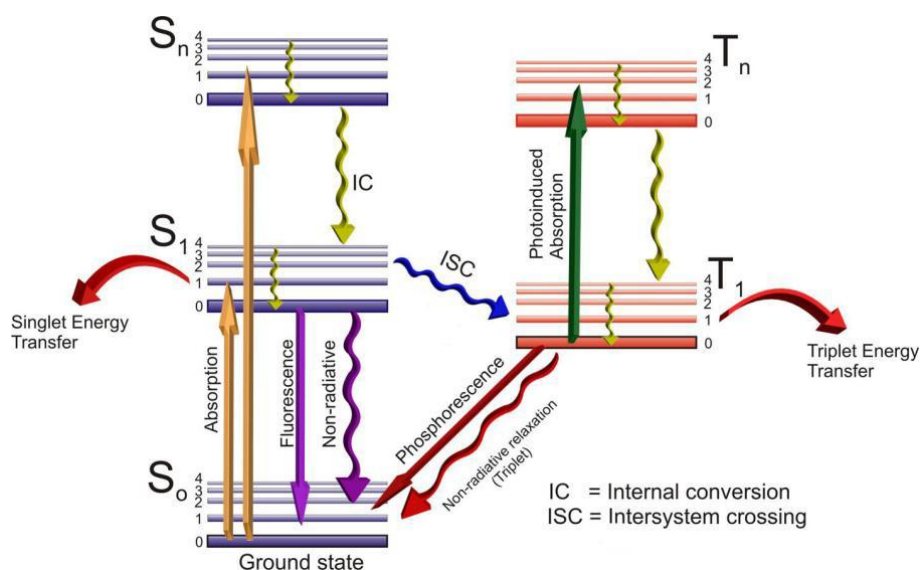


Figure 2.11: Radiative and non-radiative processes in a molecule presented in a Jablonski diagram (taken from Ref²⁵)

2.3.1 Photoluminescence

The formation of excitons and the subsequent emission of a photon upon absorption of light is called photoluminescence (PL). Since the aforementioned spin selection rules apply, only singlet excitons are formed. The PLQY η_{PL} is the ratio of excitons that recombine radiatively and is dependent on the availability and probability of non-radiative deactivation pathways. Further decreasing η_{PL} are singlet excitons, which transition to a triplet-state via ISC and, in the absence of radiative decay channels due to negligible spin-orbit coupling, cannot contribute to the luminescent decay. In general η_{PL} is expressed as

$$\eta_{PL} = \frac{k_r}{k_r + k_{nr}} \quad (2.2)$$

where k_r and k_{nr} denote the radiative and non-radiative rate constants.

2.3.2 Electroluminescence

In contrast to PL described in 2.3.1, excitons are formed by injected charge carriers and correspondingly this process is called electroluminescence (EL). Importantly, electronic excitation is not limited to the generation of singlet excitons and thus, according to simple quantum mechanical spin statistics, 75% of the generated excitons are triplet in nature, while only 25% are in a singlet state. In this context, however, it should be noted that the singlet-triplet ratio is still under heavy debate among the science community^{38,39}. In the absence of spin-orbit coupling, the maximum efficiency achievable for EL is limited to 25%. Analogously to PL, a ratio for the amount of generated photons per injected charge carrier can be defined as

$$\eta_{EL} = \eta_{PL} \cdot r_{ST} \cdot \gamma_{cap} \cdot k \quad (2.3)$$

Here, η_{PL} represents the PLQY introduced in chapter 2.3.1, r_{ST} is the ratio of singlets formed per exciton, γ_{cap} signifies the amount of excitons formed per charge carrier and k is a proportionality factor that ensures that various losses like quenching effects are accounted for.

2.4 Charge Transport

As already mentioned, organic semiconductors exhibit a great amount of structural disorder compared to inorganic semiconductors causing the disappearance of a continuous band found for the single crystal structures of inorganic semiconductors. Instead, many individual HOMO and LUMO states localized on individual molecules appear. As demonstrated in Figure 2.12,

the distribution of these states with respect to the energy can be described by a Gaussian distribution. Clearly, any charge transport happens between localized states and, therefore, the charge carriers have to overcome the potential barrier resulting from the localization. In addition, kinks and twists of the polymer backbone, as well as impurities incorporated during the synthesis further lower the observed charge carrier mobilities (from 10^{-5} cm²/Vs to 10^{-1} cm²/Vs)⁴⁰.

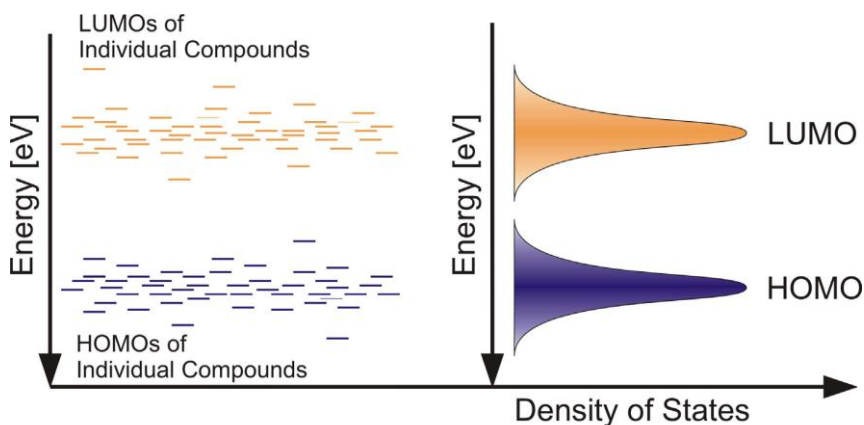


Figure 2.12: HOMO and LUMO states on individual compounds following a Gaussian distribution (taken from Ref¹³)

As a consequence, the charge carriers are not able to move freely through the material and the transport can be described by a thermally activated (phonon assisted) hopping process from one state localized at one molecule to the next state localized at a neighboring one. R.A. Marcus developed the Marcus theory⁴¹ which provides a first approximation for the charge transfer rates of the prevalent hopping process:

$$k_{et} = \left(\frac{4\pi}{h}\right) t^2 \left(\frac{1}{\sqrt{4\pi\lambda k_B T}}\right) e^{\frac{\lambda}{4k_B T}} \quad (2.4)$$

In the formula for the charge transfer rates, T denotes the interchain transfer integral that links the dependence of the charge carrier mobility with the electronic coupling between HOMO and LUMO levels. λ describes the structural reorganization while T stands for the temperature, h is the Planck constant and k_B is Boltzman's constant.

2.5 Energy Transfer

One mechanism for the migration of excitation energy is the non-radiative energy transfer which basically can be described as energy exchange between an excited donor that relaxes to the ground state and thereby transfers the excitation energy to an acceptor in the ground state. This process can again be divided into dipole-dipole coupling and exciton tunneling. The

transfer rate for this radiationless energy migration between a donor D and an acceptor A is given by

$$k_{DA} = \frac{2\pi}{\hbar} |U_{DA}|^2 J_{DA} \quad (2.5)$$

with

$$U_{DA} = U_{DA}^C + U_{DA}^{Ex} \quad (2.6)$$

U_{DA}^C represents the dipole-dipole interaction and U_{DA}^{Ex} the interaction between donor and acceptor via exciton tunneling.

The spectral overlap J_{DA} is defined as

$$J_{DA} = \int \varepsilon_A(\lambda) f_D(\lambda) \lambda^4 d\lambda \quad (2.7)$$

where ε_A is the molar extinction coefficient of the acceptor, f_D represents the normalized emission spectrum of the donor and λ denotes the wavelength.

2.5.1 Förster Transfer

The coulomb interaction U_{DA}^C in (2.6) in the limit that the distance between donor and acceptor is sufficiently large can be described by a so called Förster type energy transfer⁴². In this case, the transfer process is represented by an emission and subsequent absorption of a virtual photon. Due to the dipolar nature of the transfer, the spin selection rules for optical transitions also apply and cause the Förster transfer U_{DA}^C to be unequal zero only when singlet excitons are involved (see Figure 2.13).

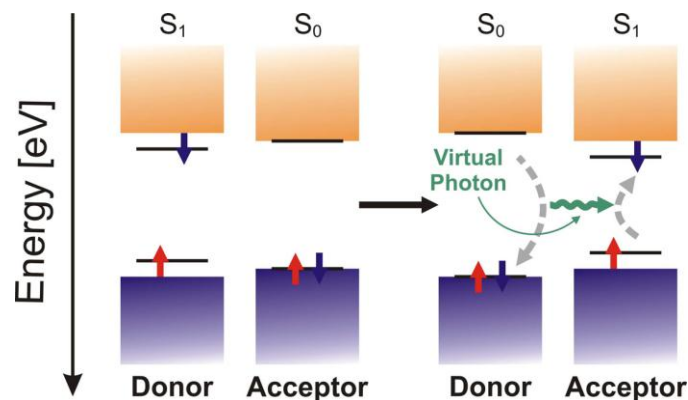


Figure 2.13: Mechanism of the non-radiative Förster energy transfer (taken from Ref¹³)

The transfer rate for the Förster type energy transfer is given by

$$k_{ET} = \frac{1}{\tau_0} \left(\frac{R_0}{R} \right)^6 \quad (2.8)$$

where τ_0 represents the life time of the excited donor, R the distance between donor and acceptor and R_0 , which is also called Förster radius. R_0 , is defined as

$$R_0 = \frac{9000 \ln 10}{128\pi^2 N_A} \frac{f^2 \eta_{PL} J_{DA}}{n^4} \quad (2.9)$$

with N_A as the Avogadro number, f defining the orientation between donor and acceptor and therefore called orientation factor, η_{PL} as the PLQY of the donor, n as the refractive index of the solvent and J_{DA} representing the spectral overlap integral defined in (2.7).

From (2.8) it is evident that the transfer rate of the Förster type energy transfer is proportional to R^{-6} . Furthermore, R_0 depends on the spectral overlap J_{DA} and therewith the transfer rate k_{ET} as well. From Figure 2.14 it can be seen that R_0 is the distance between a donor and an acceptor where the probabilities for a radiative decay of the donor or a transfer of the excitation energy to the acceptor are equal.

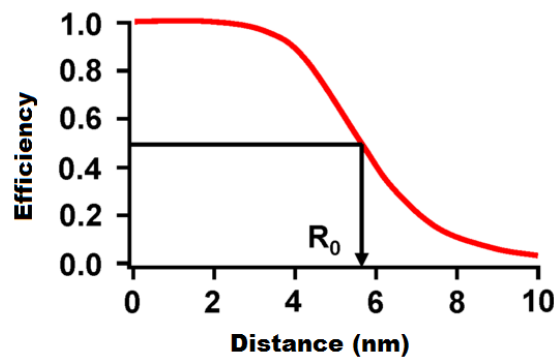


Figure 2.14: Dependency of the transfer efficiency on the distance (taken from Ref ⁴³ and modified)

2.5.2 Dexter Transfer

The contribution from U_{DA}^{Ex} in (2.6) refers to an energy transfer process that happens via an exchange interaction. This transfer mechanism, termed Dexter transfer ⁴⁴, involves the exchange of an excited electron from the donor with one in the ground state from the acceptor (see Figure 2.15). Compared to the Förster type transfer, the conservation of the spin for both,

donor and acceptor, is not demanded but the conservation of the total spin is required. For this reason a Dexter type energy transfer is allowed for singlet- as well as triplet excitons.

Regarding the transfer rate, an exponential dependence on the distance between donor and acceptor is evident:

$$k_{ET} = K J_{DA} e^{-\frac{2R}{R_{VDW}}} \quad (2.10)$$

K is an experimental factor and related to orbital interactions, J_{DA} as before represents the spectral overlap integral, R is the distance between donor and acceptor and R_{VDW} is the van der Waals radius.

The reason for the exponential dependence on R is directly related to the quantum mechanical nature of this exchange interaction which represents a tunneling process from the donor to the acceptor. Due to that, the wave functions of the donor and the acceptor are required to overlap significantly in order to achieve an efficient energy transfer. Hence, the contribution from a Dexter type energy transfer is only significant for distances up to 1 nm⁴⁵.

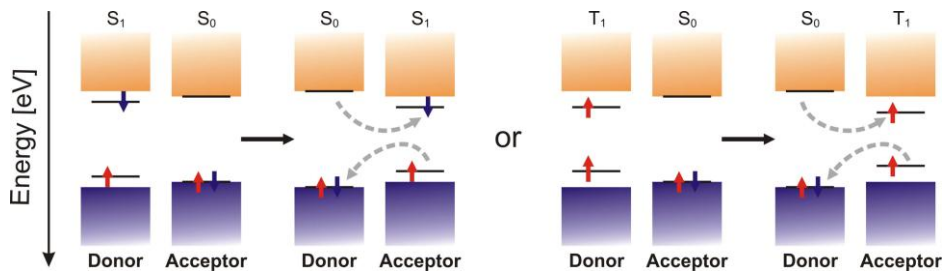


Figure 2.15: Scheme of the Dexter transfer mechanism (taken from Ref¹³)

3 Working Principle of OLEDs

Ever since the first successful demonstration of an OLED by Tang et al. ¹, who used a sandwich structure of one organic layer enclosed by two electrodes built on top of a substrate, this basic device setup is the assembly of choice for OLEDs, even if today it is usually enhanced by including more organic layers. Figure 3.1 shows a basic device set-up, where the sandwich structure of the OLED is built on top of a glass substrate. The sandwich structure itself consists of a transparent electrode, commonly indium-tin-oxide (ITO), onto which a layer of an organic semiconductor is applied, either via a solution based process or an evaporation process, completed by a second electrode, usually applied via evaporation, on top of it.

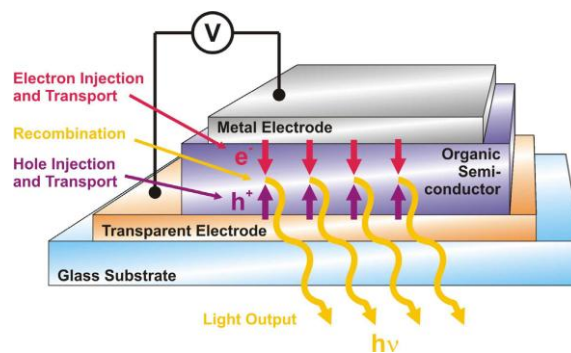


Figure 3.1: Schematic picture of the sandwich structure employed in OLEDs (taken from Ref ¹³)

From Figure 3.1, it is clearly evident that an OLED functions by injecting charge carriers from the electrodes into the organic layer. Upon injection, these charge carriers are describable as polarons whose transport is driven by the applied external field. Finally, positive and negative polarons can form excitons and recombine radiatively in the organic semiconductor.

The description given above is very basic. In order to get a better understanding of the processes that occur in an OLED, the flat band model and a single layer OLED under forward bias are visualized in Figure 3.2. The flat band model can be drawn under the assumption that no external bias is applied. Under this circumstance, it is possible to name the quantities that have a substantial impact on the injection and transport of the charge carriers. The work function of the anode is labeled ϕ_A , while ϕ_C denotes the work function associated with the cathode. The barriers resulting from the difference in energy for electrons and holes between the organic layer and the electrodes are ΔE_e and ΔE_h , respectively. In order to maximize the injection efficiency and, therewith, the device performance, the energy barriers have to be decreased by selecting appropriate electrode materials with a work function close to the HOMO/LUMO level of the organic semiconductor.

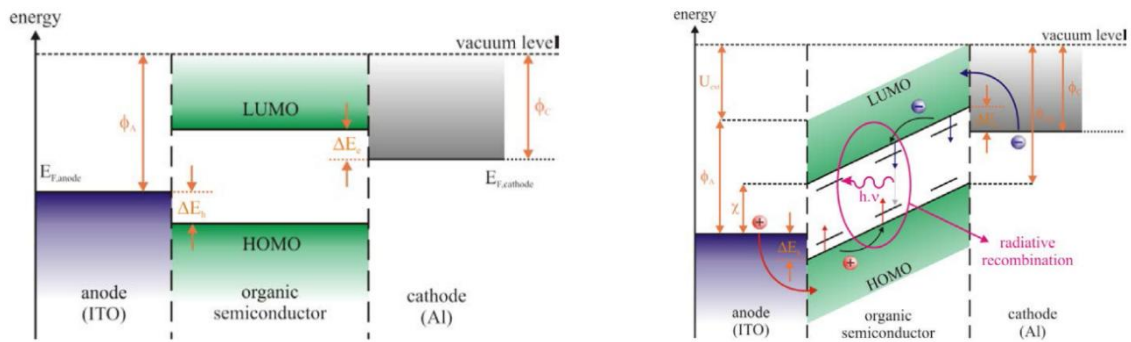


Figure 3.2: Flat band model (left) and working principle (right) of a single layer organic light emitting diode biased in forward direction (taken from Ref ⁴⁶)

While the flat band model allows for the identification of existing energy barriers, the dynamics of an OLED can only be explained when an external bias U_{ext} is applied. Because of the external bias, the work function ϕ_A of the anode increases. The occurring alignment of the Fermi levels of all materials tilts the HOMO and LUMO levels of the organic semiconductor which causes the shape of the effective potential barrier to change from a step to a triangle. This allows the charge carriers to tunnel through this barrier and, therefore, facilitates the injection into the organic semiconductor. After injection, the formed polarons drift through the organic semiconductor, directed by the applied external bias, until they either meet an oppositely charged polaron and form an exciton or reach the opposite electrode and leave the organic semiconductor. In case that an exciton is formed, it can relax radiatively or via any other decay as described in chapter 2.3. However, since there is no barrier preventing polarons to exit the organic semiconductor in this single layer geometry, in most cases only a small amount of polarons form an exciton, which leads to low luminous efficiencies usually observable for single layer devices.

One solution to improve upon the presented single layer OLED constitutes the introduction of additional layers. One possibility for such a multilayer structure is depicted in Figure 3.3, where a hole transport layer (HTL) and an electron transport layer (ETL) are introduced. The former facilitates hole injection by lowering the effective injection barrier by means of an additional energy step between the anode and the emissive layer (EML), while at the same time adding an energy barrier ΔE_e for electrons. The ETL, which is added between the EML and the cathode, facilitates the injection of electrons into the emissive layer, while it can also add a barrier for holes ΔE_h under certain circumstances. It is clearly evident that by choosing the ETL and HTL accordingly, large barriers that prevent the extraction of charge carriers from the EML are realizable. The combination of the lowered effective injection barrier for charge carriers and the blocking capabilities can result in a greatly increased polaron density within the EML and, thus, enhanced exciton formation probability finally resulting in improved device efficiencies.

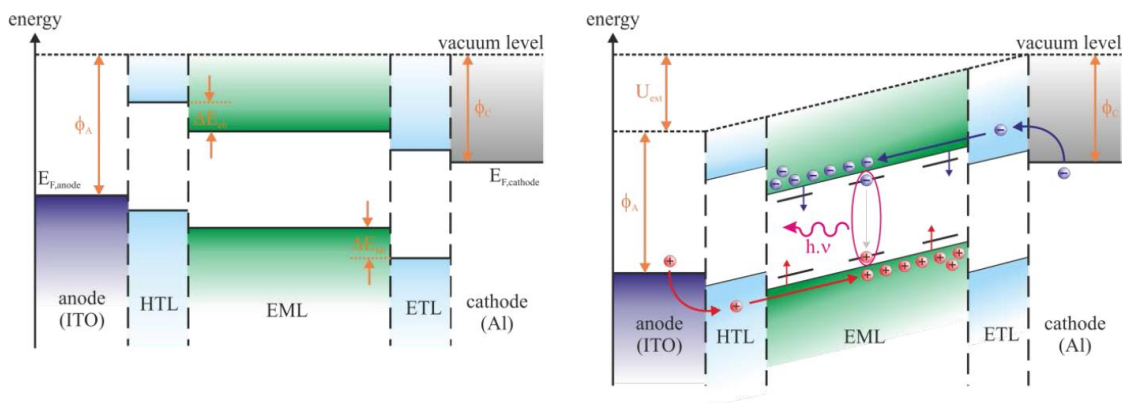


Figure 3.3: Flat band model (left) and working principle (left) of a multilayer OLED consisting of an HTL/EML/ETL structure with an applied forward bias (taken from Ref ⁴⁶)

3.1 Interfaces between Metal and Organic Compounds

When designing OLEDs the processes occurring between the interfaces of different materials are very important in order to achieve high efficiencies. The reason can be traced back to the possible formation of charge carrier blocking energy barriers at the interface between different materials. Depending on the types of materials that interface each other, different processes can occur. Therefore, the first of the following subchapters deals with the interface between metals and organic semiconductors, while the second considers the effects observable in the case of two organic semiconductors.

3.1.1 Metal-Organic Interfaces

In earlier works, the alignment of the energy levels between organics and metals was described in terms of the Mott-Schottky-rule ^{47,48}, which basically assumes that the vacuum levels of the participating materials align. However, experimental results demonstrated conclusively that this assumption is not true and an abrupt change of the work function of a clean metal was observed for the great majority of metal-organic combinations. These so called vacuum level shifts are explained by a change in the electron distribution at the interface between the metal and the organic. The corresponding change of the surface dipole of the metal then leads to a shift of the electric potential above the surface of the metal ⁴⁹. This modification is demonstrated in Figure 3.4, on the left where the work function ϕ_m of the metal is a combination of the bulk chemical potential (μ_{bulk}) and the surface dipole (SD) before these two materials were brought into contact. As a consequence of a reduced surface dipole, the work function ϕ'_m is reduced after a contact is formed (Figure 3.4, right). In literature, this reduction is commonly termed as the formation of an interface dipole (ID) that should not be confused with a physically present dipole but more like a pushing-back of the electron distribution to the bulk of the material which leads to a lowered SD. The formation of such an

ID can then lead to the formation of an injection barrier that would not have existed according to the Mott-Schottky-rule.

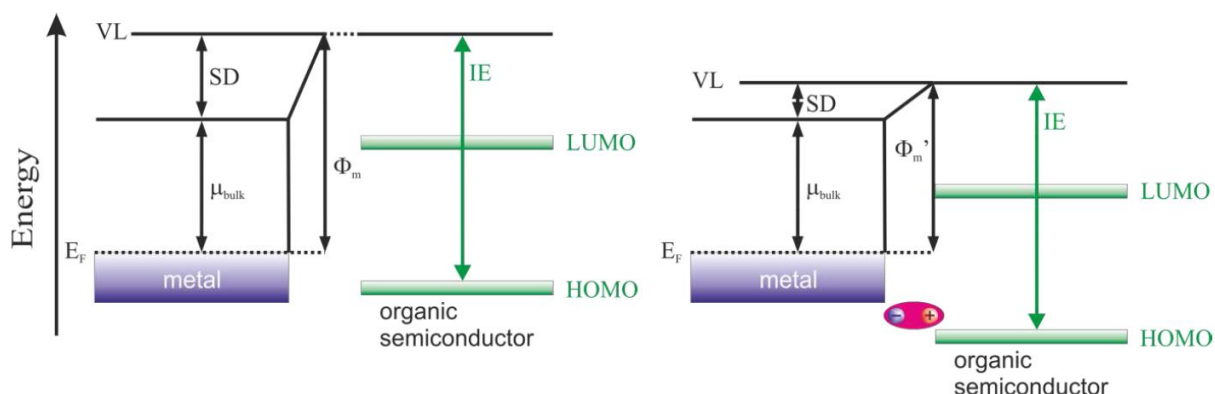


Figure 3.4: Energy levels in a metal-organic contact before (left) and after (right) the formation of an interface dipole (taken from Ref ⁴⁶)

As long as only weak electro-chemical interactions occur, the explanation that the SD is lowered by the confined electron distribution is valid. However, in case of strong electro-chemical interactions, several mechanisms that lead to the formation of physical interface dipoles were identified ⁵⁰:

- Intrinsic dipoles present in the organic semiconductor
- Image charges present in the metal that cause a polarization of the electron cloud of the organic semiconductor molecules close to the metal interface
- Formation of electronic interface states as a result of a mixture of the energy states of the participating compounds
- Change in the chemical structure as a consequence of interfacial reactions

3.1.2 Organic-Organic Interfaces

In the second section about organic-metal interfaces, the formation of an interfacial dipole caused by a reduction of the surface dipole of the metal is explained. While in general the same effects as in case of metal-organic interfaces can occur in organic-organic interfaces, the impact these effects have on the interface energetics is quite different. For instance, the formation of a SD due to a possible confinement of the electron distribution to the bulk can be disregarded in many cases. At the same time, charge transfer, permanent dipoles and interfacial electronic states are often the major contributors to the formation of an ID.

3.2 Charge Injection

For efficient device operation, it is imperative to consider under which circumstances efficient charge carrier injection can occur. Depending on the interface energetics prevalent at the metal-organic interface (see chapter 3.1.1) two different contact types, particularly an ohmic contact and an injection limited contact, can be formed. The type of contact depends on the energy difference between the work function of the metal and the HOMO/LUMO level of the organic semiconductor.

3.2.1 Ohmic Contact

The formation of an ohmic contact at the cathode side can take place when the work function of the metal is lower than the LUMO level of the organic semiconductor ($\phi_m < E_{LUMO}$). A similar situation arises in case of the anode, when the work function of the metal is larger than the HOMO level of the organic semiconductor ($\phi_m > E_{HOMO}$). The absence of an energy barrier and the potential difference cause charge carriers to transfer to the organic semiconductor until it aligns with the work function. This effect is commonly referred to as Fermi-level pinning⁵¹.

3.2.2 Injection Limited Contact

The injection limited contact arises when $\phi_m > E_{LUMO}$ in the case of electrons or $\phi_m < E_{HOMO}$ is true. In this case, the charge carriers move from the organic semiconductor to the interface region and form an interface dipole. This consequently leads to the formation of a potential barrier ΔE_a which spawns an electric field that repels the charge carriers from the junction and, therefore, less efficient transition from and to the organic semiconductor is possible. ΔE_a can in first approximation be expressed as

$$\Delta E_a = \phi_m - E_{LUMO} \text{ or } \Delta E_a = E_{HOMO} - \phi_m \quad (3.1)$$

However, for a real device the resulting potential (see Figure 3.5) turns out to be lower than the first estimation in (3.1). This becomes evident when the formed electric field required to overcome the potential caused by generated image charges is taken into account as well. These image charges are of opposite polarity to the injected charges and, therefore, also lower the effective injection barrier. The potential of the resulting injection barrier is then given by

$$\phi(E, x) = \Delta E_a - eEx - \frac{e^2}{16\pi\epsilon\epsilon_0 x} \quad (3.2)$$

ΔE_a is given by (3.1), E characterizes the applied electric field and the last term represents the potential created by the image charges close to the interface where x is the distance from the interface.

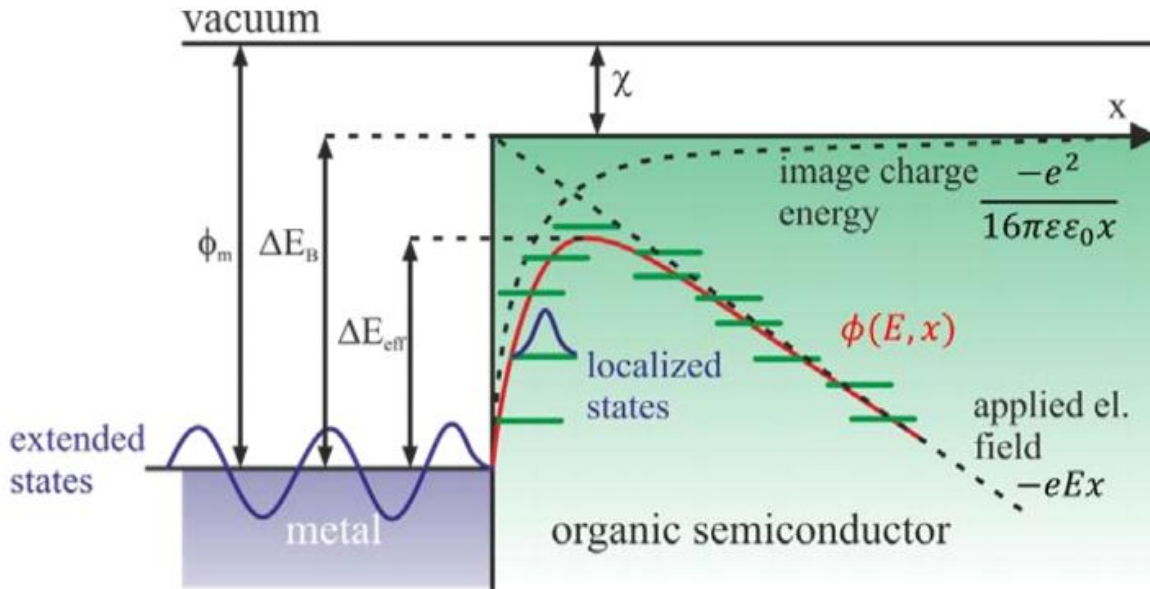


Figure 3.5: Dependence of the electronic potential Φ on the distance from the metal-organic interface. The dependence of the effective energy barrier on generated image charges and the applied electric field is clearly visible (taken from Ref ⁴⁶)

3.3 External Quantum Efficiency

The efficiency of an OLED is defined as the ratio between the amount of injected charge carriers and the amount of photons that are generated and able to leave the device. This so called external quantum efficiency η_{ext} is defined as:

$$\eta_{ext} = \eta_{eff} \cdot r_{st} \cdot \gamma_{cap} \cdot k \cdot g \quad (3.3)$$

Here η_{eff} defines the effective PLQY of the organic semiconductor in a microcavity, r_{st} specifies the ratio of singlet excitons formed per exciton, γ_{cap} indicates the amount of excitons formed per injected electron, k accounts for all possible loss effects occurring in the active layer and g denotes the losses induced by the device assembly (plasmon-generation and substrate-absorption are attributable to these losses).

The reason why the effective PLQY η_{eff} instead of the PLQY of the homogeneous medium η_{PL} needs to be considered is a consequence of the fact that OLEDs have to be treated as so called microcavities ⁵²⁻⁵⁴. In a microcavity, η_{PL} , which depends on the rate of the spontaneous

emission k_r , is now highly dependent on the surrounding environment (Purcell-effect) ⁵⁵. The effective PLQY η_{eff} is specific for every OLED assembly. Since only the radiative decay rate k_r is affected by the microcavity structure, the effective PLQY η_{eff} can be expressed as

$$\eta_{eff} = \frac{k_r^*}{k_r^* + k_{nr}} \quad (3.4)$$

k_r^* represents the altered radiative recombination rate and k_{nr} constitutes the non-radiative decay rate. k_r^* is defined as

$$k_r^* = \frac{p_{tot}^{cav}}{p_{tot}^{hom}} k_r \quad (3.5)$$

where p_{tot}^{cav} and p_{tot}^{hom} constitute the total radiative power in the microcavity system and the homogeneous medium, respectively ⁵².

Regarding r_{st} in (3.3) it is already known from chapter 2.3 that in materials, where a radiative recombination of triplets is not allowed, only singlet excitons contribute to the generation of photons, yielding $r_{st} \approx 0.25$ in the statistical limit. However, significantly higher values for r_{st} are attainable in small molecular organometallic complexes, where a radiative triplet decay is allowed ³³. The impact of an imbalanced charge carrier injection is clearly visible in single layer structures, where γ_{cap} is significantly below 1. An increase of γ_{cap} close to 1 can be realized in properly tuned multilayer structures. The factor k in (3.3) includes loss mechanisms that are called luminescence quenching. For example, singlet excitons can become quenched by impurities in the material, by field induced dissociation at high bias voltages or by singlet-triplet annihilation.

Losses attributable to the device assembly are accounted for in the factor g and include absorption of light in the materials, generation of plasmons at the organic-metal interfaces by emitted photons, total reflection at interfaces between layers with different refractive indices as well as waveguiding of the emitted light in the device. Of all of the mentioned effects, absorption plays a minor role. Losses stemming from the generation of plasmons can be minimized by increasing the distance between the recombination zone and the metal-organic interface which can be achieved by increasing the thickness of the transporting layers ⁵². Minimization of the losses stemming from waveguided modes can be accomplished by the application of grating foils to the substrate or simpler by the utilization of substrates with a high refractive index ⁵⁶. The influence of all of the aforementioned loss mechanisms on the external quantum efficiency is depicted in Figure 3.6. Due to the various factors inhibiting an efficient out coupling, until today only 40-50% of the generated light inside the OLED can be extracted in devices with a geometry specifically optimized for out coupling ^{53,54}.

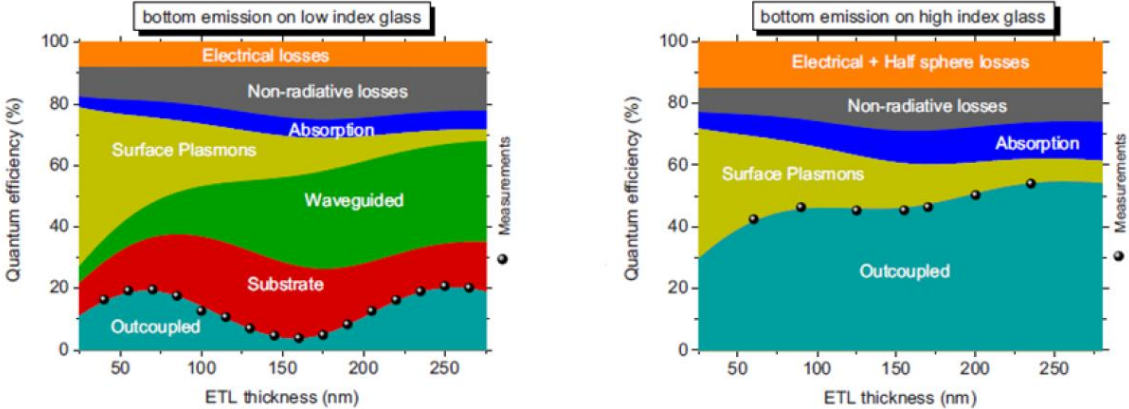


Figure 3.6: Different loss mechanisms affecting the amount of light extractable from an OLED as a function of thickness of an ETL. The situation for glass with a low- (left) and high (right) refractive index is depicted (taken from Ref ⁴⁶)

4 Experimental Methodology

This chapter covers sample preparation, the photophysical methodology employed for individual compounds as well as the routines for characterizing the manufactured OLED substrates. Finally, the instruments that were used for determining layer thickness and layer morphology are presented.

4.1 Sample Preparation

4.1.1 Substrate preparation

If not stated otherwise, experiments were conducted using ITO coated glass substrates. The plates were square in shape, displaying an edge length of 25.4 mm (1 inch) and a thickness of about 1 mm. The ITO-covered glass substrates (KINTEC Company) were structured by means of an etching process in concentrated hydrochloric acid (37% HCl). Structuring was performed by covering the areas that were to remain by adhesive tape. The etching was accelerated with process zinc powder (Sigma-Aldrich) deposited on the uncovered areas of the substrate. Following the etching processes, which took 25s to complete, the substrates were rinsed by deionized water. The adhesive tape was removed mechanically using acetone and isopropanol. Subsequently, the substrates were subdued to various supersonic treatments in toluene and isopropanol for 15 min each. The cleaning procedure was concluded by a dry cleaning step in oxygen plasma for 5 min at a pressure of 3×10^{-1} mbar with a partial pressure of oxygen of 1×10^{-1} mbar.

For absorption- and PL measurements in thin films, quartz substrates (DELTA TECHNOLOGIES, LTD) were used. These substrates were mechanically cleaned first, followed by consecutive rinsing of the substrate with isopropanol and acetone.

4.1.2 Layer Deposition

A layer of PEDOT:PSS (poly(3,4-ethylenedioxythiophene) : poly(styrenesulfonate)) with a thickness of approximately 50 nm was spin cast on the substrate in a laminar flow box under ambient conditions and dried under dynamic vacuum ($p < 5 \times 10^{-3}$ mbar) at 120°C for 45 min. The samples then were cooled down to room temperature for approximately 45 min. The active organic materials were dissolved in the respective solvents and spin coated on the previously applied PEDOT:PSS layer under argon atmosphere and dried at 60°C-100°C for 45 min in vacuum ($p < 1 \times 10^{-5}$ mbar).

Organic thin films for spectroscopy were prepared on substrates treated as described in chapter 4.1.1. Solutions with concentrations in the range of 2 g/L up to 4.5 g/L were spin coated onto the quartz substrates under inert conditions with a spinning rate between 100 rpm and 1500 rpm for 15 s to form the film and concluded by a drying step with 3000 rpm for 40 s.

4.1.3 Electrode deposition

After the deposition of the organic layers, the substrate was placed in a custom build vapor deposition unit which was located in an argon box in order to ensure the substrates never get in contact with atmospheric conditions. The deposition unit then was evacuated until the pressure reached a value below $p < 10^{-6}$ mbar. At this point, the evaporation process commenced and the layers were deposited from tungsten boats via a shadow mask. Each of the so formed eight devices featured an area of 10 mm². The top cathode was a combination of a low work function material and an aluminum layer. For the low work function materials either Calcium (Ca) or Cesiumcarbonate (Cs₂CO₃) was evaporated with Ca amounting to a 10 nm layer at a rate of 2 Å/s and Cs₂CO₃ constituting either 1.5 Å or 1.5 nm in thickness at a rate of 0.1 Å/s. The evaporated aluminum thickness amounted to 100 nm and was deposited at a rate of 5 Å/s. Monitoring of the deposited layer thickness and current evaporation rates was done by a quartz microbalance monitor and controller (Sigma Instruments Inc.).

4.2 Photophysical Characterization

4.2.1 Absorption Measurements

In a first approximation the attenuation of a light beam that passes through matter can be described by the Beer-Lambert law

$$I = I_0 \cdot e^{-\alpha \cdot d} \quad (4.1)$$

I_0 is the intensity of the light beam before travelling through matter, I is the intensity after the passing, α is the absorption coefficient of the sample and d the length of the optical path in the material.

Absorption spectra of solutions as well as of thin films were measured by a PERKIN ELMER LAMBDA 900 UV/VIS and a SHIMADZU UV-1800 spectrophotometer. Both spectrophotometer feature a double beam design, where one acts as the reference beam and the other becomes attenuated by the material under investigations. The reference beam allows for the automatic subtraction and correction of the absorption spectrum of the solvent in case of solutions and of the substrate in case of thin films. The determination of the absorption

coefficient α was easily possible in case of solutions since it was the only unknown parameter as the solutions were measured in quartz cuvettes (HELMA) with a specified diameter of $d = 10$ mm. In this thesis all absorption spectra were measured in absorbance, which is defined by

$$Absorbance = \log\left(\frac{I_0}{I}\right) \quad (4.2)$$

Furthermore, it has to be mentioned that in case of solutions concentrations in the range of 10^{-5} g/L to 10^{-1} g/L were prepared. All measurements were performed under ambient conditions.

4.2.2 Photoluminescence Measurements

Photoluminescence spectra were acquired by a SHIMADZU RF-5301PL spectrofluorophotometer, which had a custom made sample holder for thin films as well as for solutions. To identify and avoid self-absorption and inner filter effects³⁷, the concentrations for solutions ranged between 10^{-5} g/L and 10^{-1} g/L, depending on the material under investigation. All PL spectra were corrected with the corresponding response curve of the instrument.

4.2.3 PLQY Measurements

The PLQY was introduced in chapter 2.3.1 and is defined as the ratio of emitted and absorbed photons:

$$\eta_{PL} = \frac{\text{number of emitted photons}}{\text{number of absorbed photons}} \quad (4.3)$$

Evidently, a direct measurement of the amounts of photons absorbed and emitted is not a trivial task. Therefore, an indirect method for the determination of η_{PL} was established and is highly accepted^{57,58}. Following this, the absolute PLQY of a material is determined by the absorbance and emission characteristics of the sample and related to a reference material with known PLQY.

All PLQY determinations were carried out using quinine sulfate (Sigma Aldrich) as the reference material. The absolute value of the PLQY is 0.546 when dissolved in 0.5 M H_2SO_4 ⁵⁹. In order to determine the PLQY of the material under investigation, absorption and PL spectra of the compound as well as of quinine sulfate were measured in solution at different material concentrations. The PL spectra were multiplied by the respective wavelengths and a subsequent integration over the whole range of the emission yielded the total luminous

intensity. Since different concentrations were measured, it was possible to calculate the gradient for the integrated emission over the absorbance (determined at the excitation wavelength of the PL spectra). The obtained gradients were then used in

$$\eta_{PL} = \eta_{Ref} \cdot \left(\frac{grad_X}{grad_{Ref}} \right) \cdot \left(\frac{n_X}{n_{Ref}} \right)^2 \quad (4.4)$$

to obtain the absolute PLQY of the compound, where the index *X* and *Ref* denote the material under investigation and quinine sulfate dehydrate, respectively. η_{Ref} is the PLQY of the reference compound quinine sulfate dihydrate, $grad_X$ and $grad_{Ref}$ are the obtained gradients, n_X and n_{Ref} represent the refractive indices of the used solvents. When performing this indirect method of determining the PLQY, self-absorption effects resulting from too high concentrations of the solutions need to be avoided. Self-absorption becomes evident, when the measured data points in the integrated fluorescence intensity versus absorbance plot start to deviate from the expected linear relationship. In general, an error of about 10% should be assumed when the PLQY is determined using this method⁶⁰.

4.3 Device Characterization

4.3.1 Current Density-Voltage-Luminescence Characterization

Current density-voltage-luminescence (J-V-L) characterization was performed using a custom built, sealed measuring cell. The measurement cell was connected to a KEITHLEY 2612 SMU which itself was controlled by a computer. Luminance values were recorded simultaneously to the I-V values by a Keithley 6485 Picoamperemeter using a silicon photo diode calibrated with a MINOLTA LS-100 luminance meter. The current density *J* was calculated from the recorded current *I* through the active area of 10 mm² via

$$J = \frac{I[A]}{10 \cdot 10^{-6}} = I[mA] \cdot 10^2 \frac{A}{m^2} \quad (4.5)$$

4.3.2 EL Spectra of OLEDs

The EL spectrum of the light emitted by the OLED was determined by an ANDOR Shamrock 163 spectrometer with an attached calibrated charge-coupled device (CCD) detector (ANDOR DU970N-UV). The acquired spectra were then corrected for the varying sensitivity of the CCD at different wavelengths. EL spectra with different parameters were acquired. The first was a current density depended spectrum, where the spectral change depended on the applied

current density was measured. To this end, the applied current density was systematically increased. The second was a voltage depended spectrum and the third and last was a time dependent spectrum, where the change of the emission over time at a fixed current was investigated.

4.3.3 Pulsed Characterization

Compared to standard characterization, where EL properties were captured in one sweep, it is now attempted to investigate if charging effects take place and impact the device performance. This was accomplished by recording the relative luminescence and current after a 20 ms -10V rectangular shaped discharge pulse provided by an Agilent 33220A Function / Arbitrary Waveform Generator.

4.4 Layer Characterization

Layer thicknesses were determined using either a VEECO Dektak 150 profilometer or a VEECO Dimension V atomic force microscope (AFM). Furthermore, AFM was used to acquire three dimensional images of the surface topographies.

5 Structure to Property Relationships in Pyrene Cored Dendrimers

Back in 2003, Müllen and his coworkers demonstrated fluorescent polyphenylene dendrimers and the energy transfer in polyphenylene dendrimers consisting of out-of-plane twisted phenyl units with a perylenediimide core⁶¹. They observed strong fluorescence with quantum yields ranging from 20% to 50%, dependent on the dendrimer generation. For dendrimers containing perylenediimide, efficient intermolecular energy transfer between the shell and the core was confirmed, while the dendrons were also effective steric shields for the perylenediimide core.

Based on this work, Bernhardt et al.²¹ exchanged the perylenediimide core with pyrene, a high PLQY blue light emitting chromophore. The usually observed excimer emission, exciton quenching and poor solubility of pyrene caused by intermolecular stacking⁶² was addressed by the shielding provided by the polyphenylene dendrons. High quantum yields (> 92%) and effective shielding (verified via Stern-Volmer quenching experiments³⁷) were achieved at a second generation dendrimer shell⁶².

In 2008, Qin et al. reported the successful synthesis of blue light-emitting polytriphenylene dendrimers up to second generation which showed promising brightness and luminous efficiency values⁶³. The molecules were synthesized via non-catalytic Diels-Alder cycloaddition, resulting in a pure compound and thus potentially better LEDs. While triphenylene (TP) was found to be a suitable building block for the shell of the dendrimer, PLQY remained low with only 35.2% achieved at a third generation shell. The cause for the low yields were the employed phenyl substituted twisted non-planar TP units which only had a PLQY of 3.8%⁶³, a value even lower than the 9% found for planar TP⁶⁴.

With TP added as another building block for dendrimer design, several second generation dendrimers with a pyrene-core and TP added in different positions in the shell were synthesized⁶⁵. An effective energy transfer from TP to pyrene was possible and led to an increase of the PLQY from 27% to 88% when compared to TP dendrimers presented in the work by Qin et al.⁶³. The introduction of polyphenylene into the dendrimer shell led to a blue-shift of the fluorescence. The last research effort by Qin et al.⁶⁵ focused on combining TP and polyphenylene as a building block for the shell, pyrene as a highly efficient core and triphenylamine⁶⁶ as surface groups. This study verified the importance of a carefully core-, shell- and surface-optimized design.

All Dendrimers investigated in this chapter were synthesized at the Max-Planck Institute of Polymer Research in Mainz (MPI) by the group of Prof. Klaus Müllen.

5.1 Investigated Dendrimers

The work carried out by Qin et al.⁶⁵ clearly evidenced that optimization needs to be done not only with respect to the emissive core, but also with respect to charge trapping and energy transferring surface groups of the dendritic molecules. In order to assess the impact of TP units in the shell and the difference the amount of generations have on the performance of the dendrimers, several different pyrene-cored dendrimers were synthesized. In the following, the eight investigated dendrimers are outlined in short, including illustrations of their structure.

PYTPAG1, PYTPAG2 and PYDTPAG1

The first series of compounds were titled PYTPAG1, PYTPAG2 and PYDTPAG1 (see Figure 5.1). All dendrimers incorporated triphenylamine (TPA) as the surface group. TPA is a well-known redox-active moiety incorporated in small molecules or polymers where it functions as a very efficient hole transporter⁶⁶⁻⁶⁹. Most hole transporting and hole injecting materials that incorporate TPA have their HOMO somewhere between 5.3 eV and 5.5 eV, while the LUMO ranges somewhere between 2.3 eV and 2.5 eV^{70,71}. While PYTPAG2 merely differed from PYTPAG1 in the added polyphenylene generation, PYDTPAG1 had another generation of TPA added instead of polyphenylene.

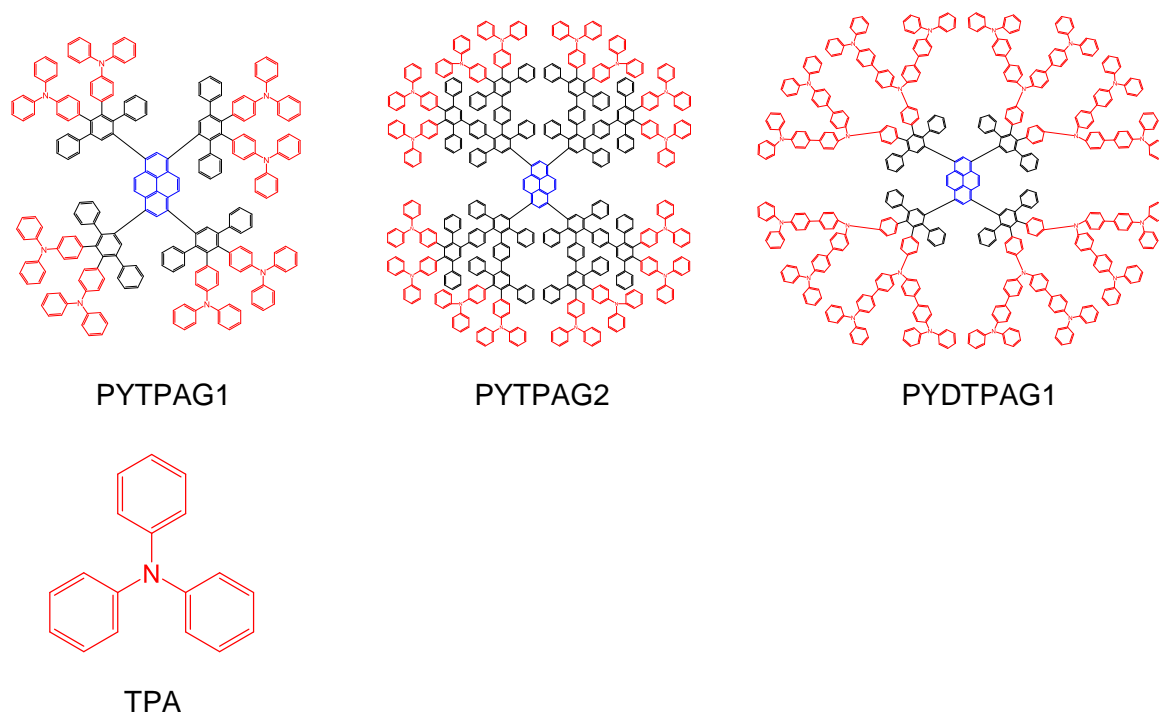


Figure 5.1: PYTPAG1, PYTPAG2 and PYDTPAG1 – Dendrimers with an emissive pyrene core, different shell configurations containing polyphenylene and TPA surface groups

PYTPG2 and PYTPG3

For the next series (see Figure 5.2) triphenylene (TP) was used as the surface group. So far Qin et al.⁶³ used TP either as the emissive group or as an energy transferring group in the shell⁶⁵. With TP being used as a surface group it was intended to determine the nature of the energy transport from the surface group to the emissive pyrene core. The PLQY of TP was found to be rather poor with only 3.8%⁶³ because of the stacking tendency of TP which is caused by its planar conformation⁷². The HOMO level of TP was determined via UPS measurements and was found to be at 6.2 eV, while its LUMO level was located at 2.8 eV⁶⁵.

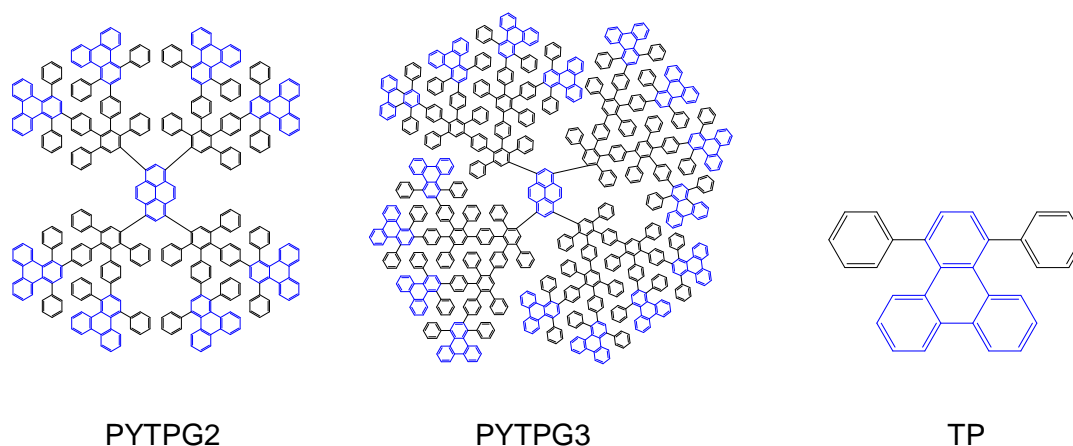


Figure 5.2: PYTPG2 and PYTPG3 – Dendrimers with an emissive pyrene core, shells with different amount of generations of polyphenylene containing TP surface groups

PYOXA

The following compound, PYOXA, was synthesized with a similar shell configuration, but with different surface groups. PYOXA, which is presented in Figure 5.3, had a shell consisting of one generation of polyphenylene and oxadiazole (OX) as the redox-active surface moiety. OX itself is a very good electron transporting moiety which is why it is often found in electron transporting small molecular or polymeric materials^{73–77}. Concerning HOMO and LUMO, values in the range of 6.0 eV to 6.5 eV and 2.2 eV to 2.8 eV, respectively, were observed⁷⁵.

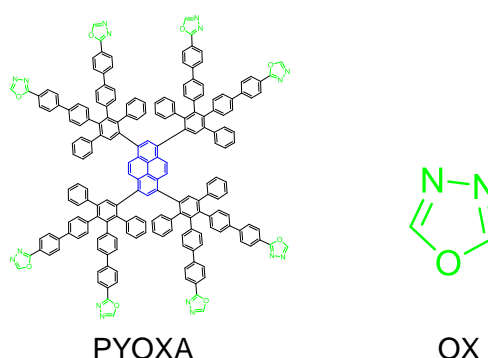


Figure 5.3: PYOXA – Dendrimers with an emissive pyrene core, one generation of polyphenylene acting as the shell and OX surface groups.

PYCAB

The next dendrimer, PYCAB (see Figure 5.4), followed the same design principle as the former ones with a pyrene core and a one generational polyphenylene shell. However, it differed in the surface group, which this time consisted of a carbazole (CAB) moiety. CAB is often used as a hole transporting moiety, but also as a host for phosphorescent materials due to its high triplet energy. 4,4'-Bis(N-carbazolyl)-1,1'-biphenyl (CBP), for example, consists of two CAB moieties and has a triplet energy of 2.55 eV⁷⁸. As far as its hole transporting capabilities are concerned, HOMO values ranging from 5.30 eV to 5.74 eV and LUMO values of 1.98 eV up to 2.22 eV were reported⁷⁸⁻⁸⁰.

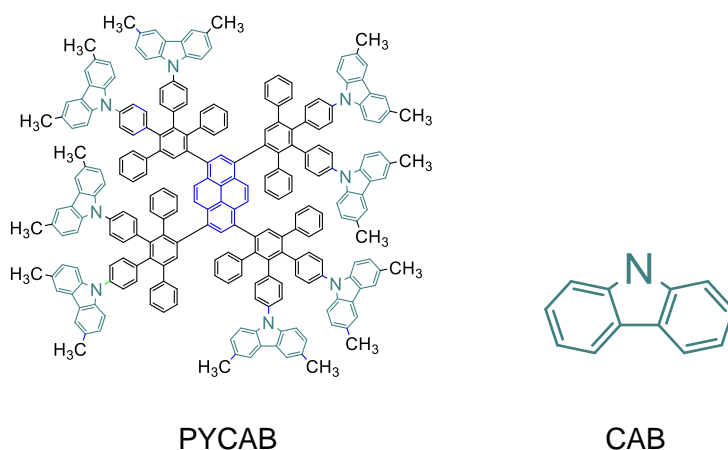


Figure 5.4: Dendrimer PYCAB with an emissive pyrene core, one generation of polyphenylene acting as the shell and CAB surface groups.

PYNPA

The last dendrimer that was investigated included an N-phenyl-naphthaleneamine (NPA) moiety as the surface group as depicted in Figure 5.5. Being very similar to TPA, NPA is also a suitable hole transporting moiety^{50,81-83}. According to literature data^{17,50,84,85}, the energy for HOMO and LUMO ranges from 5.2 eV to 5.7 eV and 2.2 eV to 2.6 eV, respectively.

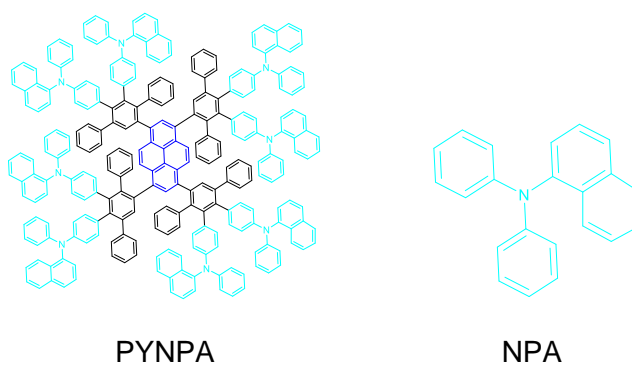
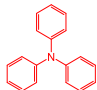
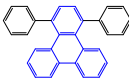
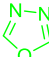
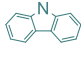
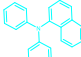


Figure 5.5: Dendrimer PYNPA with an emissive pyrene core, one generation of polyphenylene acting as the shell and NPA surface groups.

5.2 Photophysics of dendrimers

In this subchapter, the photophysical properties exhibited by the dendrimers are investigated in detail. Basic photophysical properties, like absorption and emission maxima and the PLQY of all dendrimers introduced in Chapter 5.1 in THF solution and in thin film are summed up in Table 5.1. The results listed in the table are explained in detail in Chapter 5.2.1 and 5.2.2. While Chapter 5.2.1 illustrates the effect of the different surface groups on the photophysical properties of dendrimers with pyrene cores, Chapter 5.2.2 examines the impact of different shell configurations (different generations, different shell groups) and end-capping of the surface groups on aforementioned properties. Finally, in Chapter 5.2.3 it is attempted to reveal the nature of the observed energy transfer.

Table 5.1: Photophysical properties of investigated dendrimers in THF and thin film

Surface group	Name	In solution					Thin film		
		λ_{PY}^{abs} [nm]	λ_{SUR}^{abs} [nm]	λ^{em} [nm]	ϕ_{PY}^b [%]	ϕ_{SUR}^b [%]	λ_{PY}^{abs} [nm]	λ_{SUR}^{abs} [nm]	λ^{em} [nm]
 TPA	PYTPAG1	390	310	428	71	65	395	310	450
	PYTPAG2	390	310	424	63	32	395	310	438
	PYDTPAG1	-	-	428	73	65	-	-	452
 TP	PYTPG2	390	295	427	77	53	390	295	450
	PYTPG3	390	295	424	72	39	390	295	455
 OXA	PYOXA	390	310	427	73	39	394	310	455
 CAB	PYCAB	390	297	426	75	59	393	300	435
 NPA	PYNPA	-	257	427	54	59	-	264	446

PY, SUR pyrene and surface group

$\phi_{PY}^b, \phi_{SUR}^b$ Fluorescence quantum yield determined at excitation wavelength coinciding with absorption maximum of pyrene and surface group, respectively.

5.2.1 Effect of Different Surface Groups on the Absorption and Emission Profile

Figure 5.6 shows the UV-Vis and PL spectra of PYTPAG1, PYTPG2, PYOXA, PYCAB and PYNPA in diluted THF solution (0.005 g/l) and in thin film. Additionally, key parameters like absorption and emission maxima as well as PLQY of all dendrimers characterized in Figure 5.6 are listed in Table 5.1.

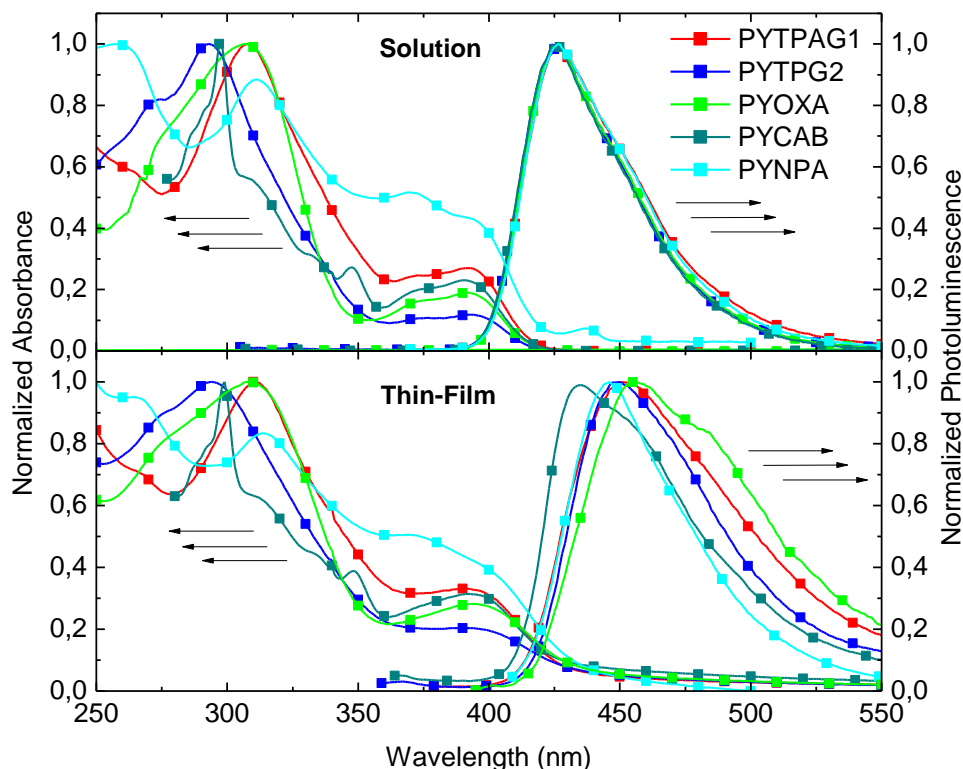


Figure 5.6: Absorption and emission profile of PYTPAG1, PYTPG2, PYOXA, PYCAB and PYNPA in solution (THF) and thin film

The absorption spectra in solution were characterized by contributions from the redox-active moieties attached to the surface of the dendrimers as well as by features stemming from the pyrene core. It was possible to observe two different groups of absorption spectra, one group consisting of PYTPAG1, PYTPG2, PYOXA and PYCAB and one group consisting of only one dendrimer, namely PYNPA.

Looking at the absorption spectra of PYTPAG1, PYTPG2, PYOXA and PYCAB it was possible to identify two intersecting zones with the first one – for a better understanding it is called Zone A in this context – ranging from well ahead of 250 nm to 360 nm and the second one – Zone B – ranging from about 355 nm to approximately 405 nm. While all four dendrimers showed a similarly structured absorption spectrum in Zone B, with a local maximum at 390 nm and a

shoulder at about 370 nm, their absorption spectra clearly differed from each other in Zone A, showing different peaks, shoulders and local minima. In detail, the absorption range of PYTPAG1 with TPA on the surface featured a local minimum at 275 nm wherefrom it rose to its peak value at 310 nm followed by a steady decline until the crossover to Zone B. PYTPG2, in contrast, showed an increase from well ahead 250 nm until it reached its maximum at 297 nm, with a shoulder at 270 nm. As with PYTPAG1, the absorption spectrum of PYTPG2 featured a steady decline after its peak till it reached the crossover to Zone B at about 360 nm. The absorption spectra of PYOXA in Zone A in turn was characterized by a steady increase and decline before and after its absorption maximum which was located at 310 nm. However, contrary to PYTPAG1 and PYTPG2, the crossover section to Zone B was located at about 350 nm. In contrast to the rather slightly structured absorption spectra of PYTPAG1, PYTPG2 and PYOXA, the absorption spectrum of PYCAB was heavily structured in Zone A. It first featured a sharp increase starting from 270 nm until it reached its peak at 297 nm, followed by a sudden and sharp decline and a shoulder at 308 nm, proceeding to a more moderate decline with another shoulder around 328 nm, followed by a local minimum at 340 nm, a local maximum at 347 nm and another decline until it reached the transition area to Zone B at about 355 nm.

Since PYNPA featured a strongly diverging absorption spectrum, it represents an own group for the purpose of this analysis. In contrast to the other investigated dendrimers, the spectrum of PYNPA with NPA moieties showed one continuous structured absorption spectrum that started ahead of 250 nm and extended to 420 nm. The maximum absorbance was observed at 257 nm, while local maxima were located at 310 nm and 369 nm. Beyond a shoulder at 396 nm absorbance declined rapidly.

The following conclusions were drawn as a result of the information obtained from the analysis of the absorption spectra. Since PYTPAG1, PYTPG2, PYOXA and PYCAB all featured the described characteristic absorption spectrum in Zone B and only PYNPA was featuring diverging characteristics, it was safe to assume that this section of the absorption spectrum could be ascribed to pyrene where the absorption maximum at 390 nm corresponded to the π - π^* transition of the tetra-substituted pyrene core^{86,87}. As a consequence, the observed characteristics of the absorption spectrum of PYTPAG1, PYTPG2, PYOXA and PYCAB located in Zone A was assigned to the redox-active moieties as well as the polyphenylene shell⁸⁸. The occurring differences in the absorption spectra of the four dendrimers were accredited to their varying redox-active moieties, which of course all resulted in manifestations typical for them. In case of PYNPA it became explicit that there was an overlap in the effects of pyrene and NPA, since the absorption spectrum was a continuous one and could not be divided into two zones as in case of the other dendrimers.

In contrast to the absorption spectra, the PL spectra of all dendrimers were characterized by a similar structureless emission profile starting at 400 nm and stretching to about 525 nm, with the maximum for PYTPAG1, PYTPG2, PYOXA, PYCAB and PYNPA being located at 428 nm, 427 nm, 427 nm, 426 nm and 427 nm, respectively.

The absence of any vibrational features in the section of the absorption spectra assigned to pyrene and in the emission spectra could be attributed to the attachment of polyphenylene dendrons at the 1,3,6,8 position of pyrene²¹. Furthermore, the presented results indicate that the observed emission stemmed exclusively from the pyrene core, being the result of an energy transfer from the surface, as well as the shell, to the core. The slight variations of the emission maxima observed for PYTPAG1, PYTPG2, PYOXA, PYCAB and PYNPA probably resulted from slightly different molecular conformations as a consequence of different sterical stress⁸⁹ exerted by the attached dendrons leading to either a slightly reduced or extended conjugation length. However, varyingly effective shielding provided by the different dendrons is also a possible source for the observed variations of the emission maxima.

In solid state the absorption characteristics of the redox-active surface groups remained almost the same. However, the absorption section ascribed to pyrene (named Zone B earlier) experienced a slight bathochromic shift of 3-5 nm in case of PYTPAG1, PYOXA, and PYCAB which resulted in shifted absorption maxima being located at 395 nm, 394 nm and 393 nm, respectively. At the same time, the shoulder observed at 370 nm in solution vanished.

While comparing the absorption spectra in solution to those in thin film only revealed minor changes, the same was not true for the emission characteristics. Figure 5.6 illustrates that the emission was noticeably impacted by the different surface groups. In case of PYTPAG1 the emission profile in thin film was characterized by being broader than in solution, stretching from about 400 nm to beyond 550 nm. This characteristic was accompanied by a shift of its maximum to 450 nm (compared to 428 nm in solution). A similar broadening was observed for PYTPG2, PYOXA as well as PYCAB. PYTPG2, PYOXA, PYCAB and PYNPA also displayed bathochromic shifts from 427 nm, 427 nm, 426 nm and 427 nm to 450 nm, 455 nm, 455 nm and 446 nm, respectively. Compared to their emission spectra in solution, PYCAB and PYNPA showed the formation of shoulders at 483 nm and 454 nm, respectively.

While the bathochromic shift that occurred with the change from solution to solid state in general is explained by the increased interactions between individual dendrimer units, the magnitude of this shift also depended on the amount of shielding the dendrons attached to pyrene provide. Less effective shielding as provided by PYOXA, and to a lesser extent by PYTPAG1 as well, might therefore be a likely reason for a more pronounced red shift as well as a more broadened emission profile compared to the other dendrimers.

Two PLQYs were measured in THF solution for all dendrimers according to the procedure outlined in Chapter 4.2.3. The excitation wavelength was set to coincide with the absorption maximum of the surface moieties first, yielding ϕ_{SUR} . The second PLQY ϕ_{PYR} was then measured by exciting pyrene itself at a wavelength of 390 nm. Values of 71%, 77%, 73%, 75% and 59% for ϕ_{PYR} were determined for PYTPAG1, PYTPG2, PYOXA, PYCAB and PYNPA, respectively, while exciting at the surface groups (ϕ_{SUR}) yielded 65%, 53%, 39%, 39%, 59% and 54% for PYTPAG1, PYTPG2, PYOXA, PYCAB and PYNPA, respectively.

The fact that PYOXA demonstrated the lowest PLQY of all dendrimers, followed by PYTPAG1, supports the proposed poor shielding effect of the shell of these dendrimers. As expected, direct excitation of pyrene resulted in higher PLQY compared to an excitation taking place at the surface groups. This was the consequence of the ongoing energy transfer from the surface groups to the core, which of course is not lossless.

5.2.2 Effect of Different Shell Configurations on Photophysical Properties

Designing new dendritic materials, it was important to know the effects the implemented design rules were going to have on important photophysical properties, such as emission maximum or PLQY. For this purpose, two different design choices were made and investigated. First, the effect of an additional generation of polyphenylenes was studied, using dendrimers based on TPA and TP surface groups. The results of UV-Vis measurements as well as the PL spectra for dendrimers with TP and TPA groups are shown in Figure 5.7, illustration a) and b), respectively. Key parameters, like absorption peak, emission maximum and PLQY, are summarized in Table 5.1 which was presented earlier.

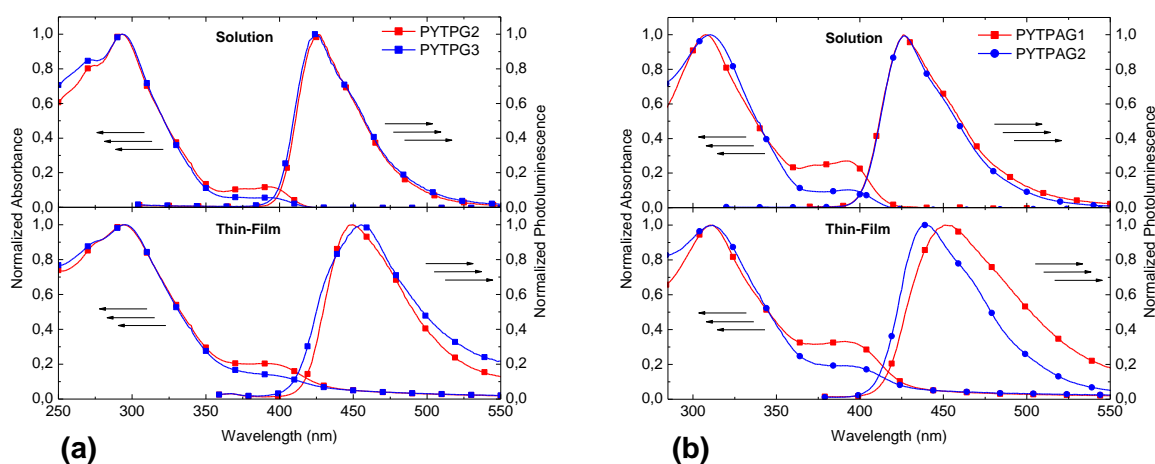


Figure 5.7: Absorption and emission profile of (a) PYTPG2 and PYTPG3, as well as (b) PYTPAG1 and PYTPAG2 in solution (THF) and thin film

In chapter 5.2.1, insufficient shielding was identified as a cause for a more pronounced bathochromic shift in solid state as well as for lower PLQY values for pyrene in PYTPAG1 and in PYOXA. Therefore, it was reasonable to expect that another generation of polyphenylenes provides a denser shell and, hence, adding another generation of polyphenylene to the shell of PYTPAG1 and PYTPG2 should provide better shielding ²¹. A detailed description of the photophysical behavior of PYTPAG1 and PYTPG2 was already given in Chapter 5.2.1. For this reason only the photophysical properties of PYTPAG2 and PYTPG3 and their changes with respect to the materials with lower generations are illustrated in the following.

In solution as well as in thin film both, PYTPAG2 and PYTPG3, displayed a quite similar absorption behavior as their lower generational counterparts, with the exception of a noticeable decrease in the pyrene absorption band. This decrease was explainable by the doubling of the surface groups on the surface of PYTPAG2 and PYTPG3 that caused higher absorbance in lower wavelength ranges of the absorption band. Pyrene as the core, however, experienced no increase in unit count which was apparent as a reduction in absorbance in the normalized absorption spectrum.

Photoluminescence experienced a minor hypsochromic shift in the solution spectra of PYTPAG2 and PYTPG3 to 424 nm and 427 nm compared to PYTPAG1 at 428 nm and the 427 nm of PYTPG2. This could have been attributed to increased steric stress the large dendrons exerted on the core, causing a lowering of the effective conjugation length of pyrene ^{90,91} or to better shielding from the environment provided by the larger dendrons.

In thin film PL spectra, the shape of the emission remained unaltered. However, PYTPAG2 experienced an even larger hypsochromic shift of 12 nm compared to PYTPAG1 with the respective PL maxima being located at 450 nm for PYTPAG1 and 438 nm for PYTPAG2. Contrary to PYTPAG2, PYTPG3 experienced a deformation of its solution based PL characteristics, featuring a broadened emission profile with its maximum being shifted to 455 nm. This represented a bathochromic shift of 5 nm compared to PYTPG2. In the case of PYTPAG2, stronger interactions between the TPA surface groups were probably responsible for the severe hypsochromic shift observed. The origin of the distortion of the emission profile of PYTPG3 is still unknown, but it was evidenced already for dendrimers consisting of pyrene bearing only polyphenylenes in the shell and surface ²¹.

Concerning the PLQY, a decrease with the added generation of the polyphenylene shell was observed. In case of PYTPAG2 only 63% PLQY versus 71% PLQY in case of PYTPAG1 were measured while exciting the respective molecules at the pyrene core. A similar trend was evident for dendrimers of the PYTPG series, since there was a decrease from 77% to 72% PLQY determined at the core after another shell of polyphenylenes was added. The fact that

the PLQY of the pyrene core was lower for PYTPAG2 compared to PYTPAG1 confirmed that the reduction in conjugation length was caused by sterical stress that distorted the planar structure of pyrene and thereby introduced additional non-radiative pathways^{90,91}. Evidence of better shielding of the core from the environment however could not be found, probably because the beneficial effect it would have on the PLQY might be negated to some extent by the structural distortion of the core.

The second design rule was to replace one generation of polyphenylenes with TPA groups in a second generation dendrimer design. This dendrimer labeled PYDTPAG1 was already introduced in Chapter 5.1 and was compared to the first generation dendrimer PYTPAG1 with TPA groups on the surface. UV-Vis and PL spectra in THF solution as well as in thin film are depicted in Figure 5.8

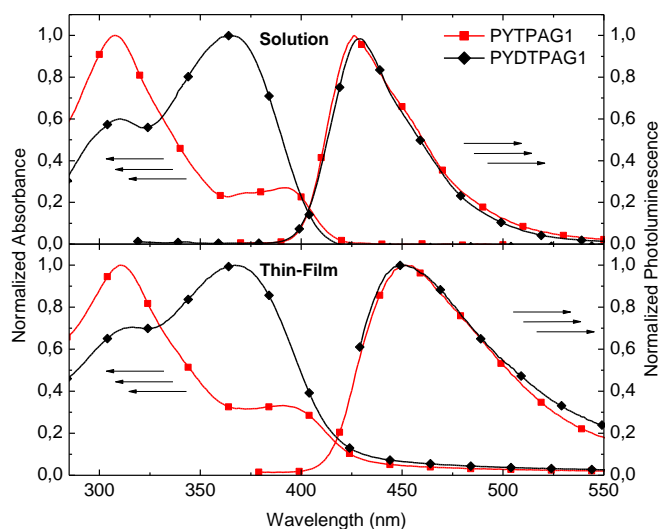


Figure 5.8: Absorption and emission profile of PYTPAG1 and PYDTPAG1 in solution (THF) and thin film

While PYTPAG1 and PYDTPAG1 showed virtually identical emission spectra in solution with an emission maximum of 428 nm, the absorption behavior changed dramatically by the substitution of one generation of polyphenylene with TPA groups. For PYTPAG1 two absorption sections were observable, one belonging to the TPA moieties and the other to the pyrene core. In case of PYDTPAG1, however, these two clearly distinguishable TPA and pyrene absorption sections disappeared. In addition, a striking difference in the location of the absorption maxima appeared, with PYDTPAG1 having its maximum at 365 nm compared to PYTPAG1 having its maximum at 310 nm. In solid state the absorption spectrum remained the same without experiencing a bathochromic shift. The latter, however, was observed for the emission spectrum of PYDTPAG1. The emission maximum was red-shifted by about 24 nm and still very similar to the emission profile of PYTPAG1 observed in thin film.

The quite dramatic change in the absorption spectrum could be explained by the interaction of two generations of TPA molecules that resulted in a possible extension of the effective conjugation length, which caused the absorption maximum to move to 365 nm up from 310 nm. The persistence of the emission behavior was not surprising since a FRET transferred the excitation energy from the TPA moieties to the core, resulting in exclusive emission by pyrene.

Concerning PLQY, excitation of both molecules at 310 nm resulted in the same PLQY of 65%. Furthermore, by exciting PYDTPAG1 at 365 nm a PLQY of 73% was determined. This was remarkably similar to the 71% obtained at 390 nm excitation wavelength. The fact that an excitation at 310 nm resulted in the same PLQY for PYTPAG1 as well as PYDTPAG1 indicated that the TPA surface moieties were excited and, in turn, transferred the excitation energy to the core from an equal distance. Interestingly, an excitation of PYDTPAG1 at 365 nm resulted in a PLQY of 73% opposed to 71% for PYTPAG1 excited at the core. An electronic interaction as observed with TTP units in the first generation⁶⁵ could be excluded as a source of this high PLQY because a bathochromic shift was not observed. Another reason for this high PLQY might have been that only the first generation of TPA units became excited. Combined with shielding provided by the second generation and, therefore, an increased PLQY of TPA units in the first generation, a highly efficient energy transfer took place.

5.2.3 Type of Energy Transfer

In this subchapter, the nature of the observable energy transfer from the donating functionalities on the surface of the respective dendrimers is investigated. For most dendrimer designs it was shown that the nature of this ongoing energy transfer was a FRET transfer^{61,92-95} (see chapter 2.5.1). In order to verify that the same type of energy transfer took place in the designs under investigation, the overlap integral J , the extinction coefficient ϵ_A , the quantum yield of the donor Φ_D as well as the refractive index n of the solvent had to be determined. The parameter governing the orientation of the chromophores between each other, κ^2 , was in first approximation set to $2/3$ for the usually assumed random orientation³⁷. All measurements were performed in THF and, therefore, $n = 1.407$. Two groups of dendrimers, PYTPG and PYTPAG – the former incorporated TP groups in its shell, the latter had TPA groups attached to the surface – were investigated. PYTPG was investigated in second and third generation, while PYTPAG was available as a first and second generational dendrimer.

The extinction coefficient ϵ_A was calculated via the following relation:

$$\epsilon_A = \frac{\log_{10} \frac{100}{\%T}}{0.1 \cdot \frac{\rho_i}{M}} \quad (5.1)$$

$\%T$ is the percentage of light transmitted through the sample, M is the molar mass of the absorbing substance and ρ_i is the mass concentration. In the case of pyrene, 202.26 g/mol were calculated for M . The extinction coefficient of pyrene then was $\epsilon_A = 17320 M^{-1}cm^{-1}$ at a wavelength of 395 nm. In order to minimize the error, the values were averaged over the values for the extinction coefficient mass concentrations 5E-2, 1E-3 and 5E-3.

Emission spectrum and PLQY of TPA were taken from Penzkofer et al.⁹⁶, while for TP the aforementioned quantities were determined in our group. The Φ_D (PLQY) of TP amounted to 3.8%, while Penzkofer et al. measured only 1.2% (using quinine sulphate dihydrate as a reference)⁹⁶. The spectral overlap between the pyrene absorption band exhibited in the dendrimers under investigation and the donating surface groups is detailed in Figure 5.9. Clearly, the overlap between the respective absorption and emission spectra was better in case of TPA than in case of TTP. This was quite well reflected in the values for the overlap integral J , as $J_{TTP} = 1.53407 \times 10^{14} M^{-1}cm^{-1}nm^4$ for TTP was lower than $J_{TPA} = 1.71823 \times 10^{14} M^{-1}cm^{-1}nm^4$ for TPA. The Förster Radii were then calculated with (2.9) and amount to $R_0 = 2.10 nm$ and $R_0 = 1.75 nm$ for TTP and TPA, respectively.

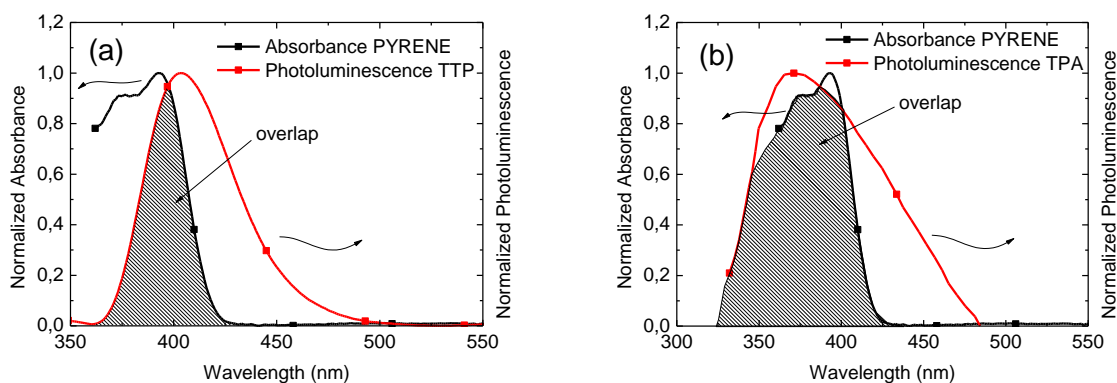


Figure 5.9: (a) Overlap of fluorescence spectrum of TTP with the absorbance spectrum of pyrene; (b) Overlap of fluorescence spectrum of TPA with the absorbance spectrum of pyrene. Data for emission spectrum of TPA taken from⁹⁶

Even though the overlap integral yielded a larger value for TPA than for TTP, the Φ_D of TPA was about half of the one for TTP. To verify the origin of the energy transfer, the distances between the accepting pyrene core and the donating surface moieties were determined via the MM2 optimized three dimensional structure by averaging over the measured distances

between the core and all donors. The optimized molecular structures are pictured in Figure 5.10. It should also be noted that the choice to set $\kappa^2 = 2/3$ seemed to be a justified one, as the MM2 optimized structures clearly demonstrated an on average random orientation of the donors with respect to the core ³⁷.

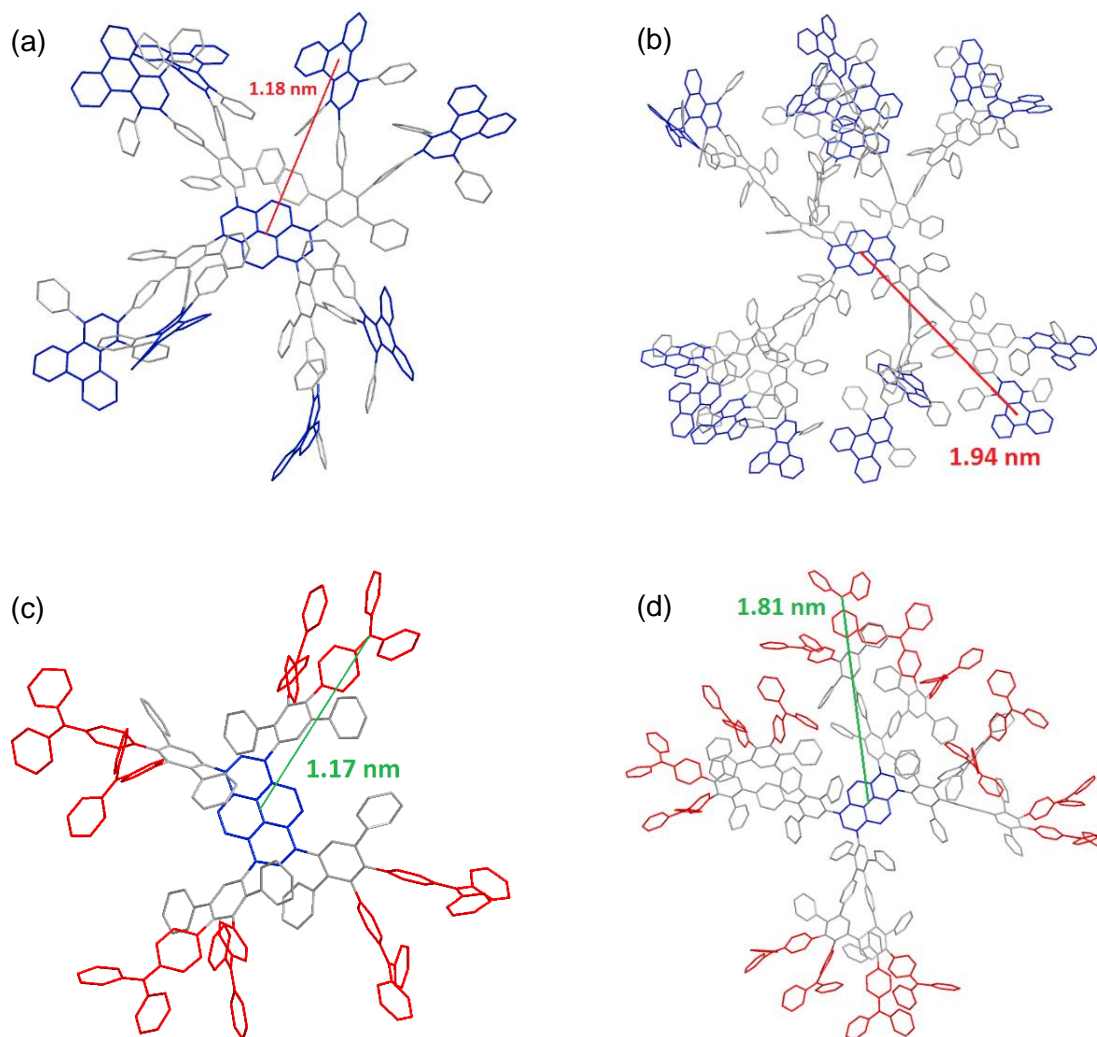


Figure 5.10: MM2 optimized structure of (a) PYTPG2, (b) PYTPG3, (c) PYTPAG2 and (d) PYTPAG3. Distances from center of the pyrene chromophore to the center of the donors were averaged over all surface groups. The average distances were (a) 1.18 nm, (b) 1.94 nm, (c) 1.17 nm and (d) 1.81 nm

From chapter 2.5.1 it is known that FRET displays an R^{-6} relationship between the distance of the donor-acceptor pair and the efficiency of the energy transfer. Expressed in terms of Förster Radii this yields the following expression ³⁷

$$E = \frac{R_0^6}{R^6 + R_0^6} \quad (5.2)$$

In Chapter 5.2.1 the PLQY of the PYTPG- and PYTPAG series was determined to be 77% and 71%, respectively, when direct excitation at the pyrene core took place. This values represented the maximum achievable PLQY of the chromophore and, therewith, of the dendrimer under investigation. Extending the equation above to yield the maximum attainable quantum yields with respect to distance results in

$$PLQY = \Phi_{PYRENE} \cdot \frac{R_0^6}{R^6 + R_0^6} \quad (5.3)$$

R represents the distance between donor and acceptor, Φ_{PYRENE} denotes the PLQY attained by direct excitation at the pyrene core and R_0 is the previously determined Förster Radius.

In Figure 5.11, the observed PLQY of dendrimers from the PYTPG and PYTPAG series are plotted against the average distance attained via the MM2 optimized molecular structures between the chromophore in the center and the donors on the surface depicted in Figure 5.10. Additionally, the results of (5.3) and a linear fit of the two data points with the intercept fixed at Φ_{PYRENE} for PYTPG and PYTPAG are included in these figures as well. For PYTPAG, perfect agreement between Förster's Theory and the experimental results was attained and, therefore, a FRET was the likely occurring energy transfer process.

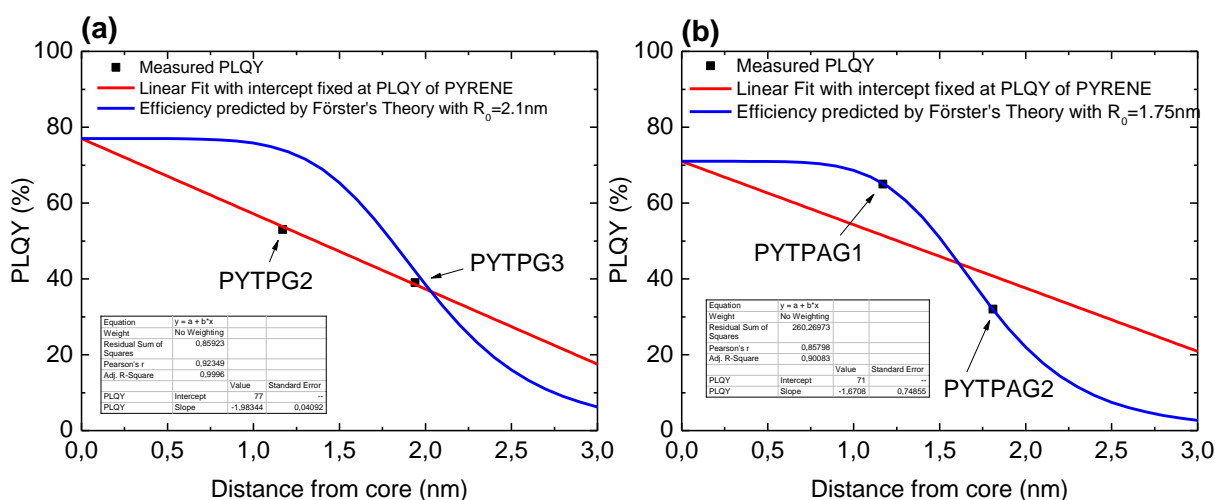


Figure 5.11: Dependence of the PLQY on the distance of the donating surface groups from the emissive pyrene chromophore when excitation occurred at the surface groups. PYTPG (a) displayed a linear relationship between distance and PLQY, while PYTPAG (b) follows a Förster-type dependence of the transfer efficiency with the distance

A different conclusion could be reached in the case of dendrimers of the PYTPG family. A comparison between the calculated results and experimental data revealed that even though one data point fitted the calculated results within the margin of error, the second data point for the second generation dendrimer PYTPG2 did not fit at all. Of course a measurement error

could be the cause for this data point being out of line with the Förster theory, however, a linear fit with the intercept fixed at 77% showed almost perfect agreement with the PLQY collected experimentally. Even though a linear fit with only two data points is almost pointless, it was remarkable that the fitted line ran through the collected data points with very good agreement, while also hitting the maximally attainable PLQY of pyrene. It is therefore very likely that either a different type of energy transfer like intramolecular energy hopping was occurring⁹⁷ or the point dipole approximation was a wrong approximation for dendrimers of the PYTPG type⁹⁸.

Concluding this subchapter it was found that for dendrimers of the PYTPAG class the energy transfer followed a distance - transfer efficiency relationship as predicted by Förster's theory, while PYTPG dendrimers displayed a linear distance - transfer efficiency dependence. For both investigated dendrimer classes the sample size (only two different shell configurations were available) was too low to allow for a definite conclusion of the observed transfer mechanisms, but nevertheless the perfect agreement attained justifies the synthesis of additional dendrimers of this class with higher generational count to confirm the obtained results.

5.3 Performance of PYTPAG1 in a Device

In Chapter 5.2 the photophysical properties of several dendrimers were investigated and analyzed. Even though the photophysical properties of a compound are important for the performance in an OLED, the efficiency of the compound is not only impacted by photophysical processes but also by exciton quenching^{99–101}, chemical degradation¹⁰² and trap sites^{103–105}. Therefore, the performance of PYTPAG1 in an ITO/PEDOT:PSS/PYTPAG1/Ca/Al structure was investigated. The data is illustrated in Figure 5.12.

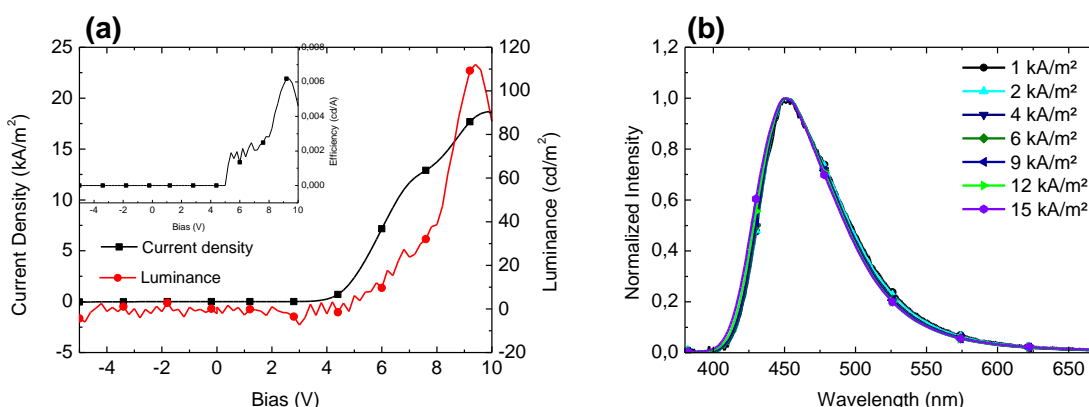


Figure 5.12: (a) Current density, luminance as well as the luminous efficiency in the inset and (b) the current dependent spectra acquired at different current densities of PYTPAG1 in an ITO/PEDOT:PSS/PYTPAG1/Ca/Al

The current density was characterized by a shoulder at about 8 V and a maximum value attained at 10 V. From a recorded onset at approximately 5 V, a continuous rise until 8 V was observed before a drastic jump to 112 cd/m² occurred. Correspondingly, the luminous efficiency also experienced a drastic increase to a maximum of 0.006 cd/A. All these observations combined indicated that a degradation took place at about 8 V, resulting in skewed efficiency values above 8 V. Therefore, the proper maximum for the luminous efficiency was about 0.003 cd/A. Electroluminescent spectra taken at different currents showed an emission profile similarly structureless as the PL spectra displayed in Figure 5.6. The emission corresponded to the Commission Internationale de l'Eclairage standard of 1931 (CIE1931) coordinates (x,y) of (0.161,0.155). The maximum attained efficiency of about 0.003 cd/A of PYTPAG1 in a single layer indicated that there is room for further optimization.

5.4 Optimization of PYTPAG1

In chapter 5.3 PYTPAG1 was embedded in an OLED in a single layer structure. While the exhibited spectral stability over time was quite excellent, other performance characteristics, like luminous efficiency and maximum luminance values, were found to be rather lacking. As already noted in chapter 3, one way to improve important performance characteristics, such as maximum luminance and luminous efficiency values, is to incorporate the emissive material in a heterostructure.

In this chapter it is demonstrated how to improve the obtained single layer values of PYTPAG1 by carefully selecting each functionality, like hole injection layer (HIL), hole transport- / electron blocking layer (HTL), electron transport- / hole blocking layer (ETL) and electron injection layer (EIL), via a benchmarking process. Additionally, all layers, except the EIL, were deposited from solution instead. The resulting OLEDs were of an ITO/**HIL**/**HTL**/PYTPAG1/**ETL**/**EIL**/Al configuration, where the elements in bold were optimized step by step.

5.4.1 HIL Optimization

The first element of the aforementioned structure to be optimized was the HIL. Three compounds were identified as suitable candidates. Clevios PH 1000 (HC-PEDOT) and Clevios PVP AL 4083 (PEDOT:PSS) were purchased from H.C. Stark, while PLEXCORE OC RG-1100 (PLEXCORE) was purchased from Sigma Aldrich. All of the introduced compounds were based on poly(3,4-ethylenedioxythiophene (PEDOT) : poly(styrenesulfonate) (PSS), which was a mixture of two ionomers. PSS was a sulfonated polystyrene that carried negative charges, while PEDOT, a conjugated polymer, carried positive charges ¹⁰⁶.

Of these three HILs, PEDOT:PSS is by far the most commonly used one in literature for application in OLEDs, owing its popularity to easy processability as well as a to a good cost-performance ratio (conductivities in the range of $0.2 - 2 \text{ S m}^{-1}$)¹⁰⁷. Conductivities for PLEXCORE are in the range of $4 - 40 \text{ S m}^{-1}$ ¹⁰⁸, about an order of magnitude higher than for PEDOT:PSS. Significantly better conductivities are achievable with HC-PEDOT, which are specified to be about $850\,000 \text{ S m}^{-1}$ ¹⁰⁹. While PEDOT:PSS and PLEXCORE were used as received, a high boiling point additive, like dimethyl sulfoxid (DMSO) or ethylene glycol (EG), was required for HC-PEDOT. In this case, 5 vol% EG was added to HC-PEDOT. From experience within our group, wettability issues during the filter process needed to be countered by further adding 50 vol% of isopropyl alcohol to the HC-PEDOT and EG solution. Then all HILs were processed as specified in Chapter 4.1.2. Before the performance could be assessed it had to be verified that the film thickness of the resulting HIL layer was at least 50 nm. For this reason, ITO substrates were coated at different rotation speeds, while the other parameters, wetting and spin time in particular, remained the same. Thicknesses of the resulting films were determined using a profilometer. The results of this experiment are demonstrated in Figure 5.13

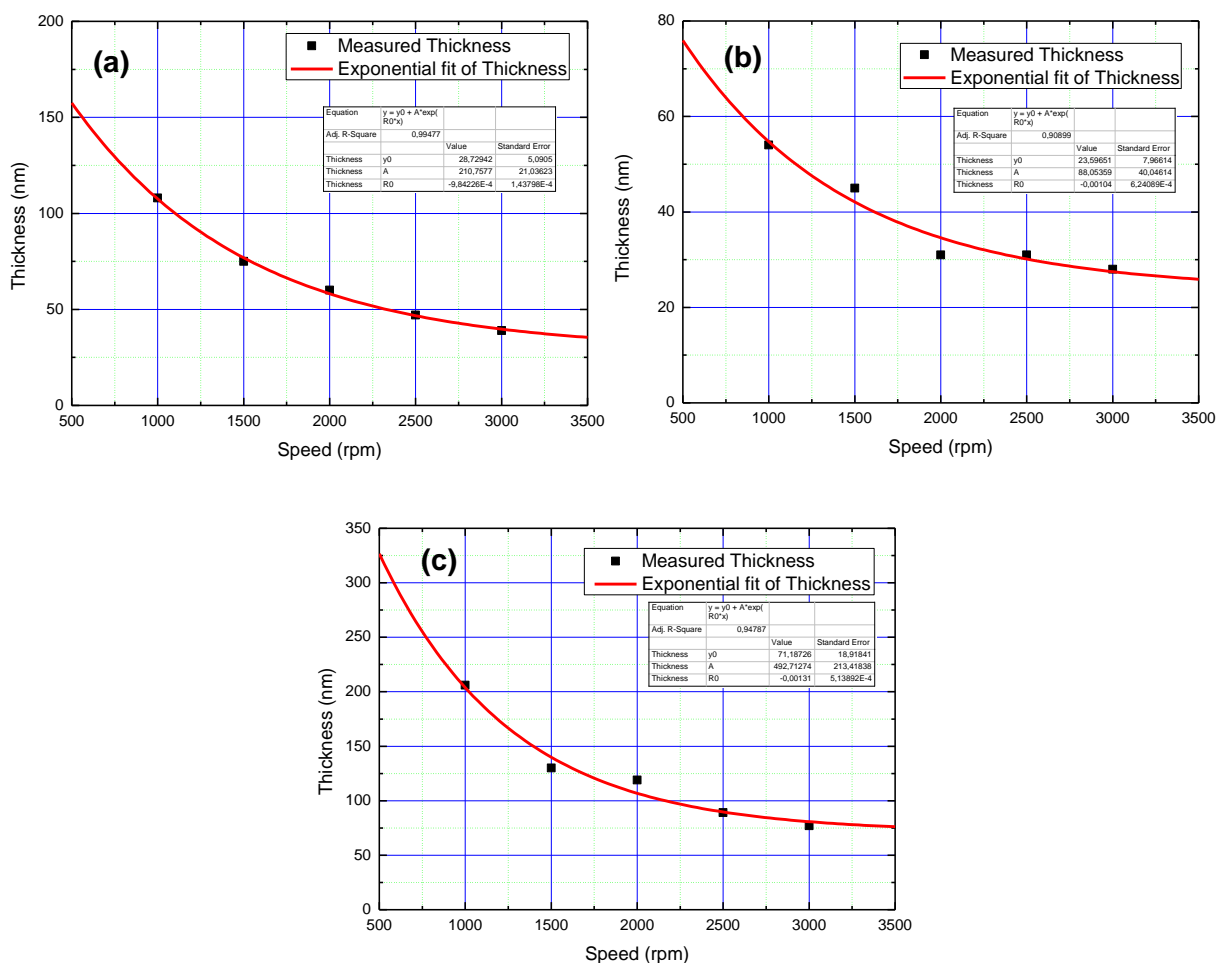


Figure 5.13: Film thickness in dependence of the spin speed for (a) HC-PEDOT, (b) PEDOT:PSS and (c) PLEXCORE. Samples were spun for 40 s after 15 s wetting time

On the basis of Figure 5.13, 2500 rpm, 1500 rpm and 2500 rpm were determined as the ideal rotation speeds for HC-PEDOT, PEDOT:PSS and PLEXCORE, respectively. It has to be noted that although the results suggested to use only about 1500 rpm in case of PEDOT:PSS, rotation speeds of 2500 rpm were used since in former experiments carried out by our group films spin cast with this rotation speeds tended to be very inhomogeneous.

Benchmarking of HC-PEDOT, PLEXCORE and PEDOT:PSS was done with PFO (see chapter 6.2) in an ITO/HIL/PFO/Ca/Al geometry. The thickness of the PFO layers was controlled by profilometer measurements and was at about 55 nm for all devices. The benchmarking results are depicted in Figure 5.14 where luminescence, current density and luminous efficiency are shown as a function of the applied bias voltage. Additionally, current dependent EL spectra as a function of the wavelength are also displayed.

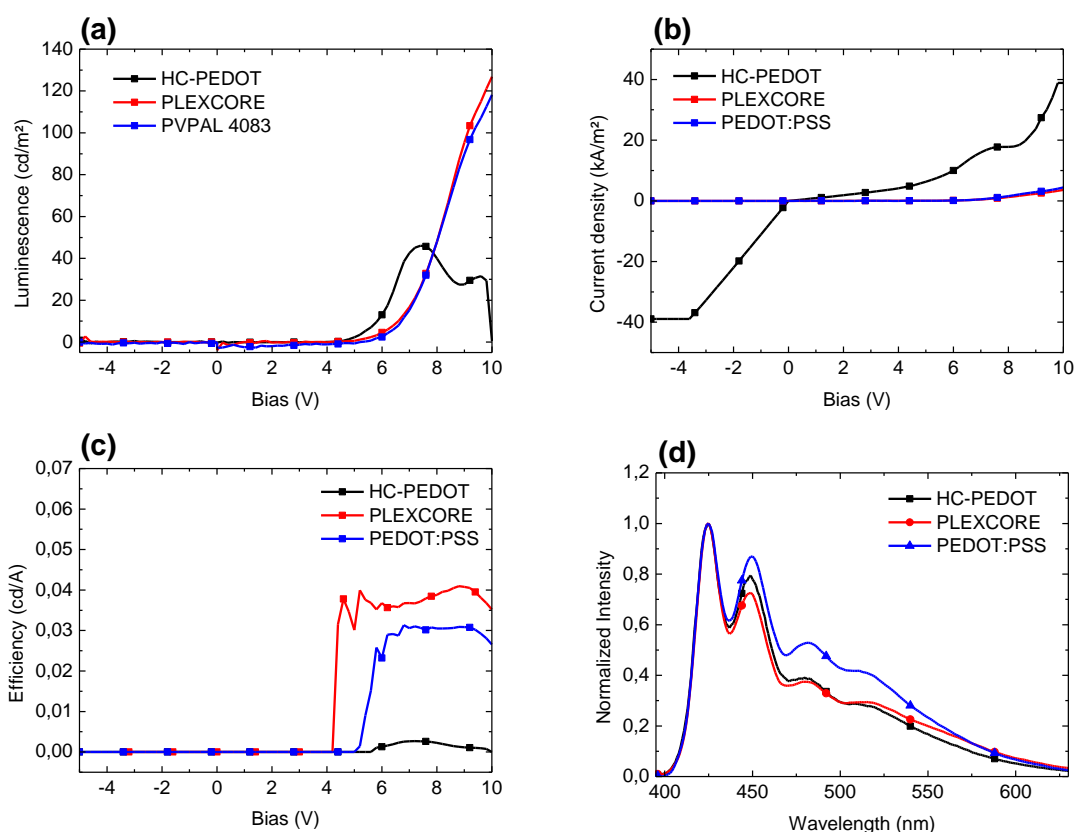


Figure 5.14: (a) Luminescence, (b) current density, (c) luminous efficiency and (d) EL spectra for PLEXCORE, PEDOT:PSS and for HC-PEDOT. EL spectra for PLEXCORE and PEDOT:PSS were taken at current densities of 1 kA/m² while HC-PEDOT EL spectra were acquired at 6 kA/m²

Starting with the EL spectra, devices based on HC-PEDOT, PLEXCORE and PEDOT:PSS displayed an EL characteristic for PFO (see Chapter 6.2). While HC-PEDOT and PLEXCORE exhibited a remarkably similar emission profile, the EL spectrum of the PEDOT:PSS based

device featured a more pronounced second vibronic compared to them combined with more intense emission in the range of 470 nm to 550 nm.

Regarding the current density (see Figure 5.14, graph b), the current was measured in forward as well as in reverse bias. In case of the HC-PEDOT based device the current density in reverse bias constituted a straight line until the compliance level was reached at about -3 V. Since this observation meant that a short circuit was formed, HC-PEDOT had to be excluded as a suitable candidate. The current density characteristics for PLEXCORE and PEDOT:PSS were to a large extent the same and showed no current in reverse bias. The similarities of PLEXCORE and PEDOT:PSS were also observable in regard to luminescence characteristics (shown in Figure 5.14, graph c) where both reached similar maximum values at a bias voltage of 10 V. For PLEXCORE 126 cd/m² were recorded in comparison to 118 cd/m² for PEDOT:PSS. These findings then resulted in a maximum luminous efficiency of about 0.04 cd/A at 4.5 V attained by PLEXCORE that stayed about the same until 9 V where an efficiency roll-off was observed. Starting at 6 V applied bias voltage, the luminous efficiency of PEDOT:PSS on the other hand reached 0.03 cd/A at 6 V until 9 V from where it experienced a similar efficiency roll-off as observed for PLEXCORE.

These results indicated that PLEXCORE was an ideal HIL in this device assembly. However, since the performance of PLEXCORE was only marginally better than that of PEDOT:PSS, PEDOT:PSS was used as the HIL from this point forward, because it featured a significantly better price to performance ratio than PLEXCORE.

5.4.2 HTL Optimization

The next step towards an optimized device structure constituted a proper choice concerning the hole transporting layer (HTL). The polymer poly(9,9-dioctyl-fluorene-co-N-(4-butylphenyl)-diphenylamine) (TFB) (ADS259BE, American Dye Source), a co polymer of poly(9,9-dioctylfluorene) (PFO) that contained a hole-transporting TPA group with the ratio 1:1 in the backbone of the polymer is depicted in Figure 5.15. First reported by Redecker et al.¹¹⁰ in 1999, it combines the beneficial hole transport properties of arylamine glasses with the solution processability of polymers. Choulis et al.⁶⁸ reported the formation of smooth and insoluble layers with a thickness of a few nanometers after an annealing step with temperatures between 180-200°C that was followed by a spin-rinse procedure. The possible use of these properties to significantly improve the performance of an OLED has also been demonstrated recently by Trattng et al. in combination with a novel pyrene based polymer¹¹¹.

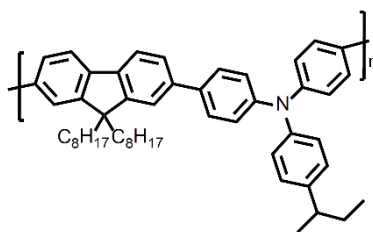


Figure 5.15: Chemical structure of TFB

The measured absorption and PL emission characteristics are illustrated in Figure 5.16. Absorption in thin film as well as in solution was characterized by a broad structureless profile in the UV-region with a maximum of 385 nm. The absorption stretched from below 300 nm to 425 nm in THF solution and to 450 nm in thin film. Like the absorption spectra, the PL spectra for solution and thin film were also devoid of any structure with the emission maxima being situated at 443 nm and 429 nm in solution and thin film, respectively.

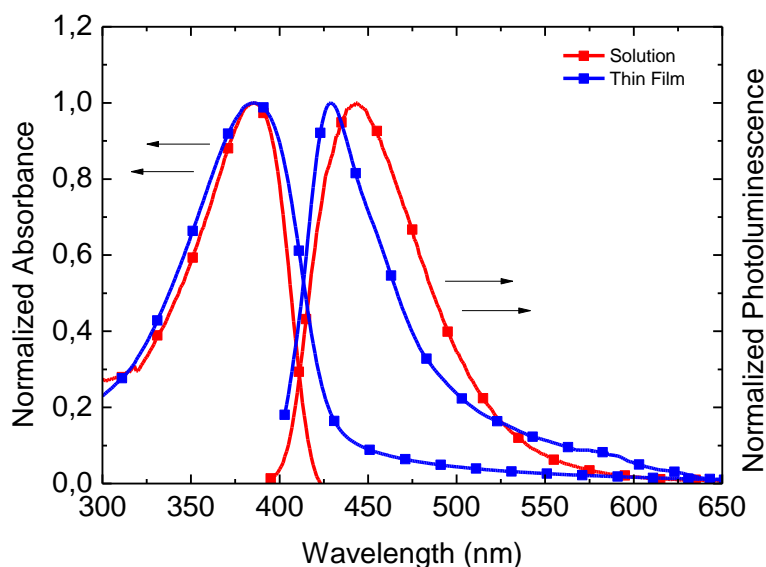


Figure 5.16: UV-visible absorption and PL emission spectra of TFB in solution (0.001 g/L; THF) and in thin film

To measure the impact TFB had on the performance of PYTPAG1 in a device, one device with TFB as a HTL in an ITO/PEDOT:PSS/TFB/PYTPAG1/Ca/Al and another device without TFB were fabricated. The TFB layer was processed from a 20 g/L toluene solution followed by a “hard-baking” step at 220°C for one hour in Ar atmosphere. Afterwards, the substrate was allowed to cool down below 50°C before it was subjected to a spin-rinse step with toluene to remove any soluble parts of the formed TFB layer away. Apart from the TFB layer, both substrates were fabricated and stored under the same conditions before the characterization began. To eliminate variations in the film thickness of PYTPAG1 as a cause for better/worse efficiency, the thickness of the emitting layer of both devices was determined via profilometer measurements. The obtained current density, luminescence and luminous efficiency

characteristics, as well as the EL spectra of the devices with and without TFB are depicted in Figure 5.17.

Comparing the current densities of both devices, it was observed that the device with TFB as a HTL displayed higher current densities until reaching the compliance level at a bias of 8 V. In case of the device without TFB a shoulder in the current density characteristics was noticeable, while at the same time the current density did not exceed the compliance level. Regarding the maximum attainable luminance values, 299 cd/m^2 at 7.8 V for the device with TFB versus 112 cd/m^2 at 9.4 V for the device without TFB were recorded. The onset with TFB as HTL was 4.6 V versus 4.9 V for the device without TFB. This resulted in a luminous efficiency of 0.032 cd/A at 5.2 V for the device with TFB compared to 0.006 cd/A at 9.2 V for the device without. However, it should be noted that the spike in the luminance characteristic for the device without TFB at a bias of 8 V was probably attributable to a device degradation process since the current density was decreasing at the same time. Therefore, the efficiency maximum at 9.2 V for the device without TFB could not be compared to the one of the device with TFB. More reasonable was a value of 0.0024 cd/A , which was the luminous efficiency on average from the onset to about 8 V of applied bias.

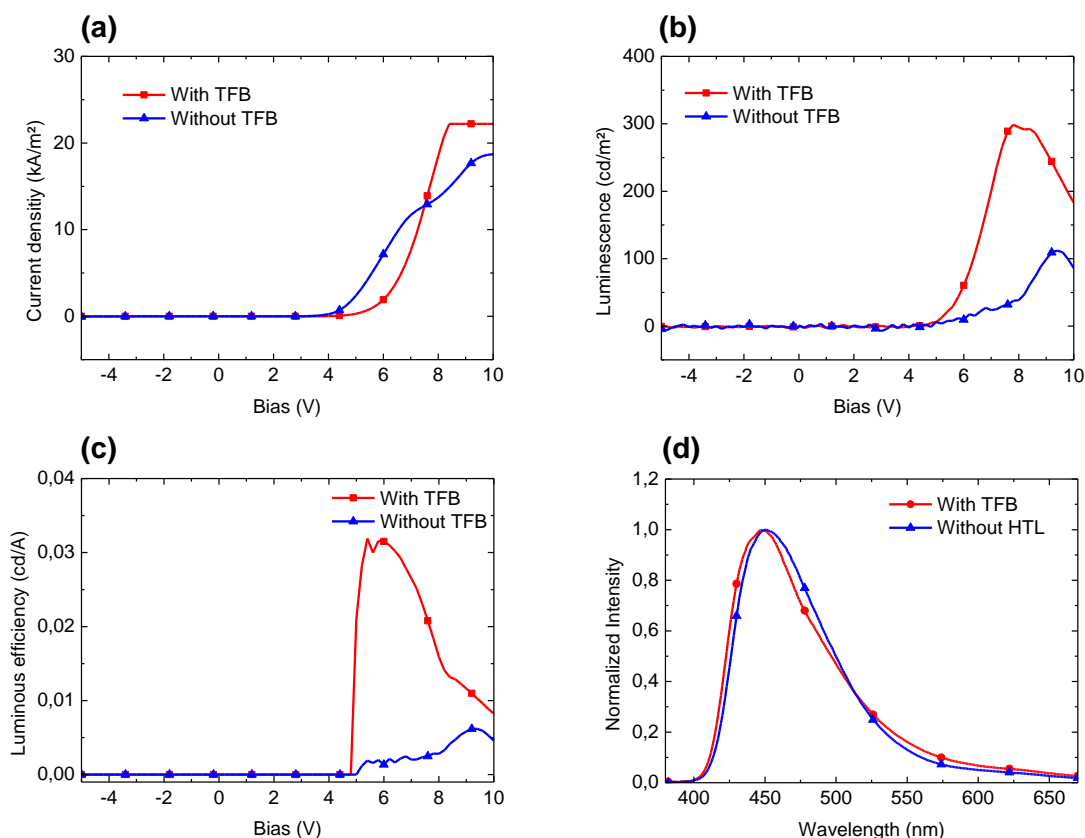


Figure 5.17: (a) Current density, (b) luminescence, (c) luminous efficiency and (d) current dependent EL spectra (taken at 10 kA/m^2) for an ITO/PEDOT:PSS/TFB/PYTPAG1/Ca/Al and ITO/PEDOT:PSS/PYTPAG1/Ca/Al structure.

Another important aspect for the incorporation of an additional layer is its contribution to the overall EL emission spectrum. The spectrum for the device with and without a TFB layer are depicted in Figure 5.17, graph d. Both spectra demonstrated an emission maximum of 450 nm. However, while both devices emitted in the range between about 400 nm and 600 nm, a contribution from TFB was visible in a minor shoulder at 475 nm, which was not present for the device without TFB. With an increase in efficiency by one order of magnitude and only a very minor contribution to the emission behavior of the device, TFB appeared to be well suited to function as a HTL in optimized device design.

5.4.3 ETL Optimization

With TFB identified as a suitable hole transporting material, a compound that fulfills the same tasks as TFB, but for electrons, needed to be chosen. Commonly used electron transporting materials (ETL) are 1,3,5-tris(2-N-phenylbenzimidazolyl)-benzene (TPBi) ¹¹²⁻¹¹⁴ or bathophenanthroline (BPhen) ^{83,115}, which are applied via thermal evaporation processes on top of the preceding layer. However, like the other layers optimized so far, the ETL should be deposited from solution as well. Therefore, the two mentioned materials had to be discarded and a polyfluorene compound with poly(ethylene glycol) (PEG) side chains (PEGPF) was chosen instead. PEGPF is a promising solution-processable material that does not dissolve the preceding layers. It was used before as an ETL by Trattnig et al. ¹¹¹. For PEGPF material properties, like chemical structure and UV-Vis as well as PL spectra see chapter 7.

As in chapter 5.4.2 the impact of PEGPF as an ETL on the overall device performance was assessed. In particular, a device where PEGPF was implemented as ETL (ITO/PEDOT:PSS/PYTPAG1/PEGPF/Ca/Al) was compared to a reference device without containing the ETL (ITO/PEDOT:PSS/PYTPAG1/Ca/Al). The equality of the thickness of PYTPAG1 was verified with a profilometer to avoid differences in the performance characteristics caused by different layer thicknesses.

PEGPF was processed from a 1 g/L MeOH solution forming a layer of about 10 nm thickness. Current density, luminance, luminous efficiency and EL spectra, as results of this benchmark, are demonstrated in Figure 5.18. The current density characteristics unveiled a huge difference between the devices with and without PEGPF. While the device with PEGPF attained a maximum current density of about 5 kA/m² at an applied bias voltage of 8.2 V before dropping to lower values, the device without PEGPF exhibited a continuous increase towards 20 kA/m² at 10 V. Luminance characteristics also showed a dramatic increase in luminance values for the device with PEGPF as opposed to the one without, reaching close to 1100 cd/m² at 8.8 V while the maximum luminance attained by the reference device was 110 cd/m² at 9.2 V. The

onset of the device with PEGPF was also reduced to 3.6 V compared to 4.9 V in the case of the device without.

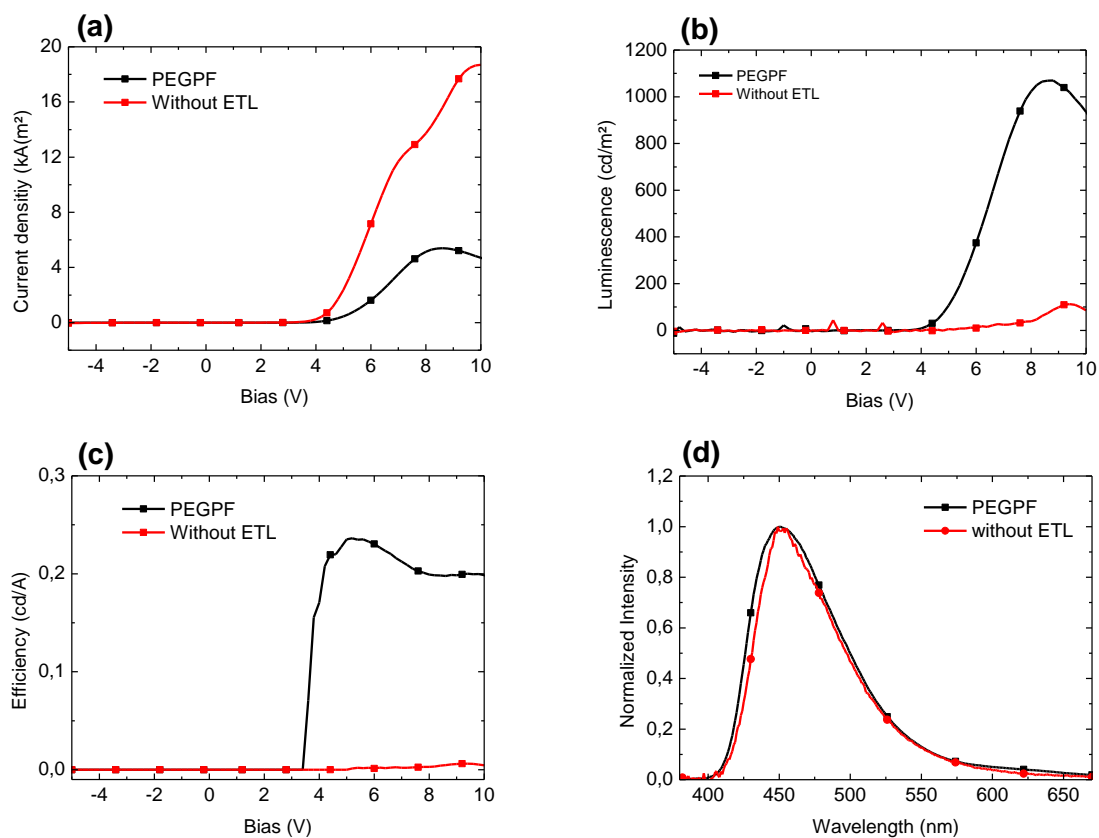


Figure 5.18: (a) Current density, (b) luminescence, (c) luminous efficiency and (d) EL spectra for ITO/PEDOT:PSS/PYTPAG1/PEGPF/Ca/Al and ITO/PEDOT:PSS/PYTPAG1/Ca/Al structures. EL spectra were acquired at a current density of 10 kA/m²

These findings resulted in a dramatically increased efficiency of 0.24 cd/A for the device with the ETL compared to the 0.006 cd/A observed at 7.8 V for the reference device. The device with the ETL reached its maximum luminous efficiency already at 5 V and experienced only a minor roll-off to 0.2 cd/A at 8 V after which it remained largely the same until 10 V. For the reference device without PEGPF the maximum in luminous efficiency at 7.8 V was a result of a degradation process. Therefore, the average efficiency, which yielded 0.003 cd/A, was a better measure for the actual device efficiency.

Comparing the current dependent EL spectra of the reference device and the PEGPF containing device, it could be seen that both had the maximum of their EL at 450 nm and a similar structureless emission profile ranging from 400 nm to approximately 600 nm. This indicated that the emission was originating from PYTPAG1. The dramatic increase in luminance as well as luminous efficiency combined with virtually identical emission spectra made PEGPF a suitable solution processable electron transporting material.

5.4.4 Cathode Optimization

The last step towards an optimized device design was the proper selection of an electron injection layer (EIL). The introduction of an EIL reduces the energy barrier present for the injection of electrons into most common organic semiconductors. Commonly used are insulating materials that form low work function contacts in connection with Al, like LiF^{116–118}, CsF¹¹⁹, CsF₂¹²⁰, MgF₂¹²¹, NaCl¹²² and CsCl¹²³. For this work, however, cesium carbonate (Cs₂CO₃)¹²⁴, a new and highly efficient low work function material¹²⁴, was used and optimized. Interestingly, up to date the electron injecting mechanism of the thermally deposited Cs₂CO₃ layer is unknown and heavily debated in literature. While some groups ascribe the increased electron injecting capabilities to the formation of a Cs complex^{124,125}, other groups have found indications that Cs₂CO₃ thermally decomposes during the evaporation process leading to a n-doping of the organic layer beneath with free Cs atoms¹²⁶. Compared to LiF, which is used in many high performance OLED designs, Cs₂CO₃ does not require Al to develop its highly efficient electron injection mechanism and, therefore, also works in connection with noble metals like Ag or Au¹²⁷. Also, the thickness of the Cs₂CO₃ layer was found to influence the electron injection mechanism^{128,129}. Ideal layer thickness are dependent on the device assembly, but typically range between 1 Å to 2 nm^{128,129}.

Since there is a dependence on the layer thickness of the fabricated EIL, two devices of an ITO/PEDOT:PSS/TFB/PYTPAG1/PEGPF/Cs₂CO₃/Al structure, where the Cs₂CO₃ layer was 1.5 Å and 1.5 nm, respectively, were fabricated.

The current density, luminance, luminous efficiency as well as current dependent EL spectra of the two devices are depicted in Figure 5.19. Regarding the current density, it was observed that the device with 1.5 nm of EIL applied reached a higher current density value with 5.5 kA/m² compared to 4.5 kA/m² for only 1.5 Å EIL thickness. Also, the device with a larger EIL reached its maximum current density already at 8.4 V, compared to 9.8 V for the other device. Luminance characteristics showed a similar trend with a maximum luminance value of 2250 cd/m² achieved at 8.2 V for the device with 1.5 nm EIL thickness versus 1550 cd/m² at 8.8 V for the thinner EIL. Onsets were observed at 3.8 V and 4.4 V for 1.5 Å and 1.5 nm of EIL thickness, respectively. These findings resulted in a luminous efficiency characteristic that gradually improved from the onset to the maximum (except for a minor kink in the trend of the device with 1.5 nm EIL) luminous efficiency values of 0.42 cd/A at 8 V for 1.5 nm and 0.41 cd/A at 7.2 V for the 1.5 Å.

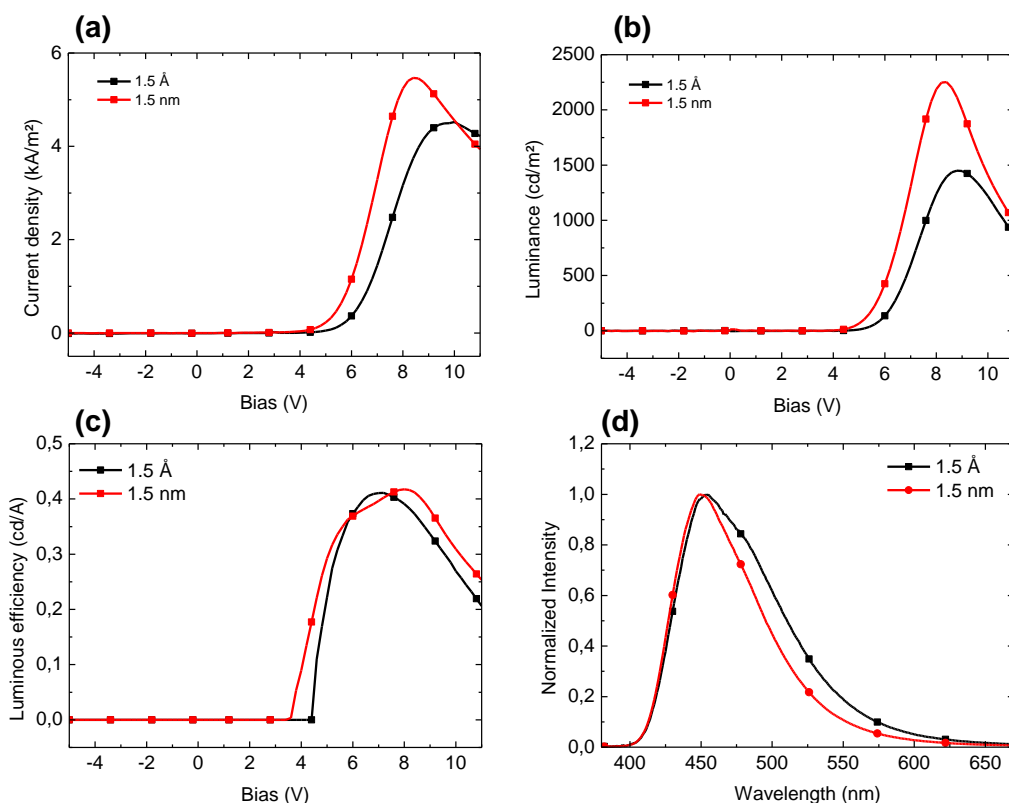


Figure 5.19: (a) Current density, (b) luminance, (c) luminous efficiency as well as (d) EL spectra (acquired at 1 kA/m²) for ITO/PEDOT:PSS/TFB/PYTPAG1/PEGPF/Cs₂CO₃/Al structures with 1.5 Å and 1.5 nm of Cs₂CO₃ evaporated on top of PEGPF.

The current dependent EL spectra taken at 10 mA revealed that both devices featured an emission with a slightly different shape in the range from 400 nm to 600 nm as well as a similar emission maximum (450 nm with 1.5 Å versus 453 nm with 1.5 nm). This pointed towards an emission originating from PYTPAG1. In case of the device exhibiting an EIL of 1.5 nm, the emission waist was narrower compared to the device with 1.5 Å of EIL thickness. The emission spectrum corresponded to the CIE1931 coordinates of (0.156, 0.139) for 1.5 nm EIL thickness compared to (0.164, 0.187) for 1.5 Å. The appearance of a shoulder at approximately 475 nm was likely the result of a shift of the recombination zone to the border of PYTPAG1/PEGPF since the second vibronic of PEGPF was located around 475 nm (as demonstrated later in chapter 7). Because electron injection at thinner EIL was less efficient, the recombination zone shifted away from the center of the emissive PYTPAG1 layer towards the cathode^{130–132}.

Concluding this subchapter, it was found that a layer of 1.5 nm of Cs₂CO₃ led to a substantial increase in luminance to 2250 cd/m² compared to 1550 cd/m² for the device with only 1.5 Å of Cs₂CO₃ while retaining the efficiency observed for the device with only 1.5 Å of Cs₂CO₃. Furthermore, 1.5 nm of Cs₂CO₃ caused the recombination zone to be positioned away from the interface with PEGPF, leading to a blue shift of the emission color compared to 1.5 Å of Cs₂CO₃. Cs₂CO₃ was therefore found to be an excellent electron injecting material when applied with a layer thickness of 1.5 nm.

5.4.5 Formation of Agglomerates

Using the optimized device assembly presented in the preceding chapter, a luminous efficiency of 0.42 cd/A was achieved (see Chapter 5.4.4), which is more than an order of magnitude away of the 9.7 cd/A of luminous efficiency with the CIE1931 coordinates of (0.144, 0.129) reported on a multilayer polymer OLED by Nau et al.¹³³. Besides possible intrinsic limitations, the most glaring issue was that no films of PYTPAG1 without agglomerates could be fabricated. As demonstrated by microscope images in Figure 5.20, even filtering of a 10 g/L PYTPAG1 toluene solution with a 200 nm polyamide (PA) filter shortly before processing was not able to reduce the amount of agglomerates found in the fabricated films to a tolerable amount. Changing the solvent to THF yielded the same results. Unfortunately, the usage of a potent solvent like chlorobenzene was not possible, because chlorobenzene was found to dissolve the hard-baked TFB layer.

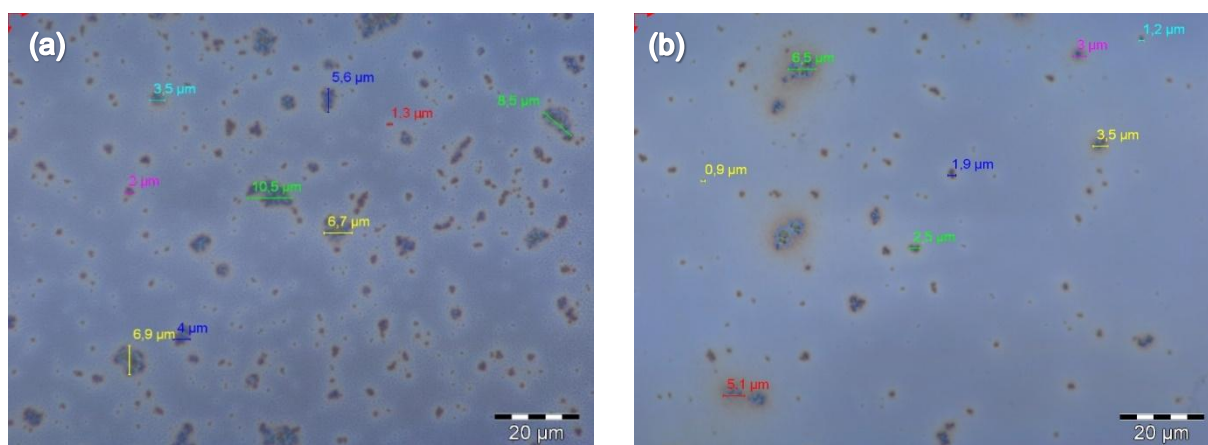


Figure 5.20: Microscope images taken for PYTPAG1 spin cast from a 10 g/L toluene solution. Image (a) is unfiltered, while (b) was filtered with a 200 nm PA filter before spin coating

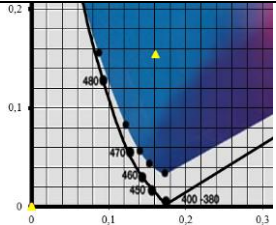
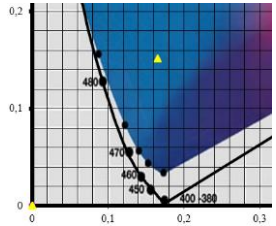
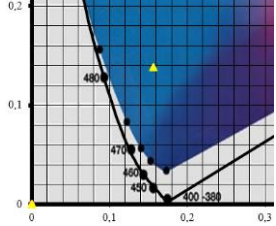
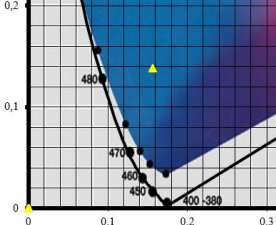
5.4.6 Optimization of PYTPAG1 - Summary

In this chapter, the systematic improvement of the performance of PYTPAG1 by introducing carefully selected layers fulfilling functions, such as hole- and electron transport and the injection of hole and electrons at the anode and cathode, respectively, was presented. The best result of each optimization step starting from the single layer assembly towards the fully optimized triple layer stack is summarized in Table 5.2

After adding TFB as a hole transport layer, PEGPF as an electron transport layer and a 1.5 nm thick Cs_2CO_3 as an electron injection layer, the maximum luminance could be increased to 2210 cd/m² with a maximum luminous efficiency of 0.41 cd/A compared to 112 cd/m² and a maximum luminous efficiency of 0.006 cd/A before. In order to further enhance the efficiency

of PYTPAG1, its film forming capabilities need to be improved by addressing the solubility issues in common organic solvents like Toluene and THF.

Table 5.2: Device data of the best device after each optimization step from the single layer to the fully optimized triple layer stack containing PYTPAG1 as emissive layer

	organic layer geometry ^a	onset voltage ^b [V]	η^c [cd/A]	max. luminance [cd/m ²]	EL Peak ^d [nm]	CIE1931 coordinates ^d (x,y)
a	PYTPAG1/Ca/Al	5	0.003	112	449	 (0.161, 0.155)
b	TFB/PYTPAG1/Ca/Al	4.6	0.031	298.7	450	 (0.165, 0.152)
c	PYTPAG1/PEGPF/Ca/Al	4.1	0.36	1480	450	 (0.156, 0.139)
d	TFB/PYTPAG1/PE GPF/Cs ₂ CO ₃ (1.5 nm)/Al	2.5	0.41	2210	449	 (0.156, 0.139)

^a on ITO/PEDOT:PSS; ^b at 1 cd/m²; ^c value of maximum luminous efficiency; ^d acquired at a current of 10 mA

5.5 Conclusion

In this chapter compounds belonging to the novel material class of dendrimers were presented. All investigated materials followed a core-shell-surface design principle with a highly efficient blue emitting pyrene core and different shell and surface configurations. The impact of the different surface groups and shell structures on the photophysical properties of the compounds was assessed by detailed photophysical studies. With one exception (PYNPA), UV-Vis spectra recorded in solution unveiled that the absorption behavior could be divided into two zones, where one zone in the range of 355 nm to approximately 405 nm was ascribable to the absorption of the pyrene core, while the other zone was heavily dependent on the incorporated surface moieties. Investigations of the corresponding thin films revealed similar absorption characteristics. All compounds demonstrated a PL emission in the range between 428 nm to 424 nm in solution which was assignable to pyrene and indicates the presence of an efficient energy transfer from the redox active surface groups to the core. As a consequence of a bathochromic shift in the range of 14 nm – 31 nm, the PL emission of all compounds ranged between 438 nm and 455 nm in thin film. The different magnitudes of the shift for individual compounds was explained by the varying effectiveness of the shielding provided by the shell as well as by the interaction between the individual dendrimer units. Direct excitation of pyrene in the different compounds yielded PLQY ranging from 54% to 77%. These differences were traced back to the amount of shielding provided by the shell and the magnitude of deplanarization of the core due to the shell configuration. Excitation of the surface groups yielded results in the range of 32% to 65% PLQY, depending on the distance from the core as well as on the incorporated surface group itself. Photophysical investigations of four dendrimers (PYTPG2, PYTPG3, PYTPAG1, PYTPAG2) revealed that an additional generation of polyphenylenes in the shell could induce more sterical stress that concurrently negated the beneficial effects of increased shielding. Investigations of the occurring energy transfer revealed a FRET in case of PYTPAG1 and PYTPAG2, while a transfer with a linear distance-efficiency relationship was observed for the dendrimers PYTPG2 and PYTPG3. Representative for all investigated dendrimers, the suitability of PYTPAG1 for the application in OLEDs was studied in an ITO/PEDOT:PSS/PYTPAG1/Ca/Al single layer assembly. However, low luminous efficiencies of 0.006cd/A combined with low luminance values of only 112 cd/m² indicated further room for improvements. The addition of TFB as a HTL and PEGPF as an ETL combined with an EIL consisting of Cs₂CO₃ yielded a tremendously increased luminous efficiency as well as a maximum luminance of 0.41 cd/A and 2210 cd/m². To further improve the device efficiencies, the observed formation of agglomerates in the spin cast films needs to be prevented.

6 Polyfluorenes with Linear and Branched Semiperfluorinated Side Chains

Contents of this chapter are submitted for publication in: Leonid Pevzner, Manuel Auer, Roman Trattnig, Markus Klapper, Emil J. W. List-Kratochvil and Klaus Müllen; "Polyfluorenes with Branched Semi-perfluorinated Side Chains for Polymer Light Emitting Diodes"; Macromolecules.

As mentioned in chapter 1, the factors that prevent solution processed OLEDs to enter the market are on the one hand performance issues of solution processable organic materials and on the other hand issues concerning the solution based assembly of devices with more than one layer.

The need for multi-layer structures is explained by the requirement of a balanced charge carrier injection and transport ¹³⁴ in order to increase device efficiencies. The possibility to deposit multiple layers on top of each other allows for the implementation of heterostructures, a concept which originates from inorganic solid-state semiconductors. A careful choice of the involved materials then enables multilayer heterostructures to provide an efficient injection and transport of charge carriers drift-diffusing from the electrodes to the emitting layer. At the same time they provide an energy barrier for charge carriers, confining them within the EML. The created barriers can then lead to increased charge carrier densities and in turn higher exciton formation probabilities. While realizing these multilayer heterostructures by thermal vacuum deposition techniques is straight forward in case of small molecules, it proves to be quite the opposite in solution processed polymer light emitting diodes (PLEDs), since most light emitting polymers are soluble in the same organic solvents and deposition of subsequent layers leads to dissolution of previously deposited layers. Thus, one has to ensure that the preceding layers do not dissolve. Several approaches that deal with this issue have already been demonstrated and are mostly based on crosslinking reactions ^{135,136}, the use of orthogonal solvents ^{137,138}, a layer-stabilizing "hard-bake" process ⁶⁸ as well as on liquid buffer layers in between the subsequent polymer layers ¹³⁹. This chapter deals with orthogonal processing realized by a novel polyfluorene type polymer with perfluorated side chains for orthogonal processing using fluorinated solvents. Here, orthogonal processing means that two compounds are not dissolvable in the same solvent and, therefore, one material can be applied on top of the other without any occurring dissolution.

6.1 Motivation and Investigated Compounds

The orthogonal solubility approach is usually performed with combinations of non-polar and polar solvents with polyelectrolyte or PEG substituted conjugated polymers as the polar soluble component. However, even small amounts of polar solvent residues, such as alcohols or water, are detrimental to the lifetimes of organic electronic devices and should therefore be avoided. Fluorinated emitting materials, on the other hand, have several advantageous properties like high hydrophobicity, lipophobicity and chemical stability. Recently, the first PF with highly fluorinated side chains (fPF) soluble in fluorinated solvents was synthesized and tested in PLEDs, but no devices with high efficiencies could be realized¹⁴⁰. PFs with altered fluorinated linear side chain configurations synthesized by Prof. Klaus Müllen and his group from MPI showed a similar, though slightly better behavior. Poor film formation was identified as a possible reason for the low efficiencies since only very thin films with up to 10 nm thickness were formed.

The favorable optical and electronic properties of PFs are due to the backbones of the polymer whereas other properties like solubility, polarity, film formation properties and aggregation behavior can be adjusted by their side chains. However, although very useful for tuning the overall properties of the target compound, side chains also dilute the optically active moieties, thus potentially lowering the output per mass of the polymer. Therefore, finding an optimal size and structure of the side chains is a perpetual goal in side chain design. To study the influence of the fluorine content and degree of branching, 3,5-di- and a 3,4,5-tri-functionalized aromatic branching agents with 1*H*,1*H*-perfluorobutyl groups have been designed and synthesized. These branching agents were used to synthesize PFs with branched, partially fluorinated side chains. The chemical structure of the synthesized polymers can be found in Figure 6.1.

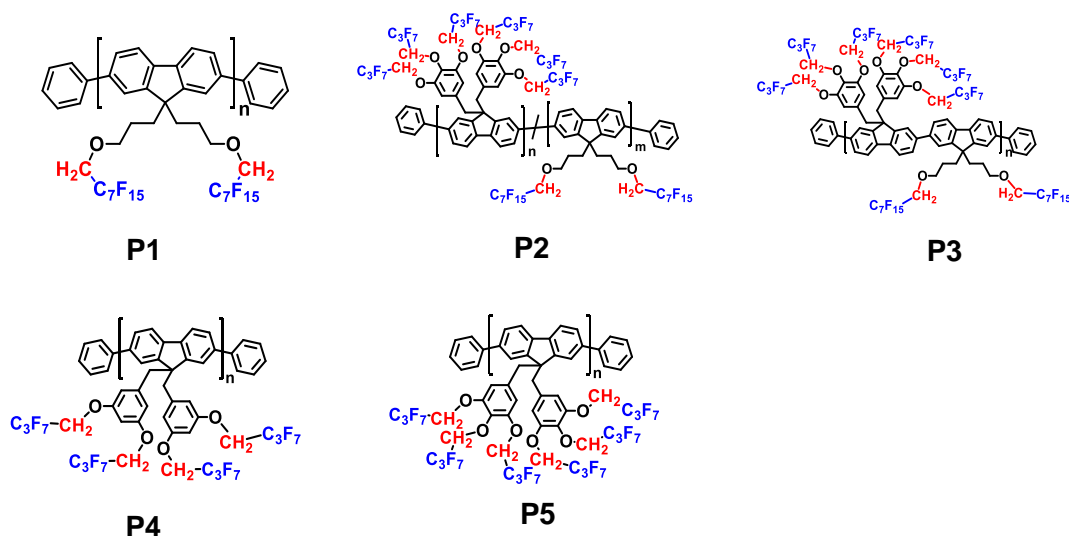


Figure 6.1: Chemical structures of the synthesized compounds with their names from top left to bottom right: **P1** [fPF-lin], **P2** [fPf-stat], **P3** [fPF-alt], **P4** [fPF-bra(3,5)], **P5** [fPF-bra(3,4,5)]

6.2 Properties of PFO

As a reference for the later on demonstrated orthogonally processable PFOs, a Poly(9,9-dioctylfluorenyl-2,7-diyl) end-capped with dimethylphenyl (PFO) (ADS129BE, American Dye Source Inc.) was chosen. PFO was heavily investigated as a promising conjugated polymer for application in blue light emitting diodes ¹⁴¹.

6.2.1 Photophysical Properties

Figure 6.2 shows the UV-Vis and PL spectra of PFO in THF solution (0.001 g/L) and in thin film. In solution as well as in solid state all absorption spectra showed a broad and structureless absorption feature in the range between 320 nm and 425 nm with the corresponding peak maxima being located at 391 nm in solution and 387 nm in thin film, which can be ascribed to a π - π^* transition in the polymer. PL spectra in contrast displayed significantly structured emission characteristics exhibiting a main peak at 418 nm in solution and at 428 nm in solid state, accompanied by two vibrational progression bands at higher wavelengths.

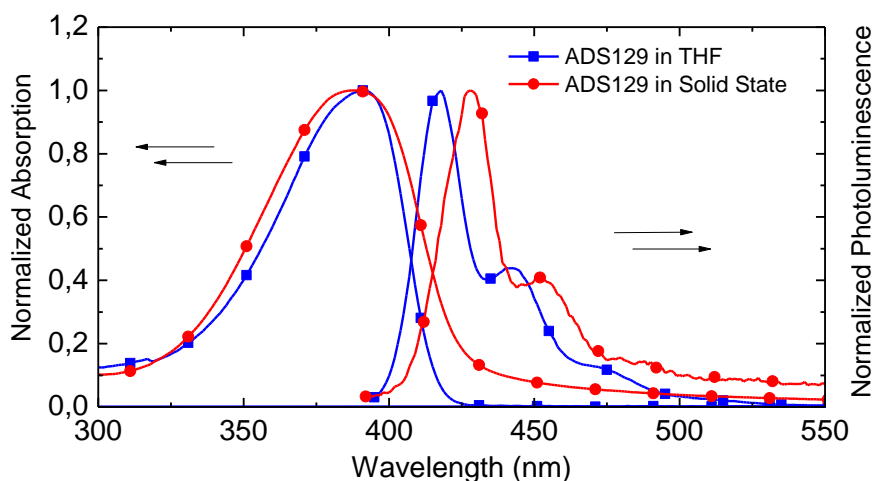


Figure 6.2: UV-Vis and PL spectra of PFO in THF (solid blue line with boxes) and in thin film (solid red line with dots)

6.2.2 Device Performance

J-V-L characteristics for a standard single layer geometry (ITO/PEDOT:PSS/PFO/Ca/Al) device are presented in Figure 6.3. The PLEDs showed a deep blue electroluminescent emission profile with maximum luminance values of up to 200 cd/m² at a bias of 6 V. The onset was determined to be at approximately 3.5 V while exhibiting a maximum luminous efficiency of 0.05 cd/A at 4.2 V. Figure 6.3 depicts time- and current dependent spectra of PFO in the same single layer geometry. The spectra showed an emission characteristic quite similar to

the previously presented PL spectra in thin film with a maximum at 422 nm. The color coordinates of the emission characteristics are located in the deep-blue region with CIE1931 coordinates of (0.17, 0.10). The stability of PFO was verified via time-dependent spectra taken at a current density of 2 kA/m². Over time, the spectra stayed perfectly unaltered with the only noticeable shift being an increase of the emission from 460 nm to 550 nm one minute after turn on.

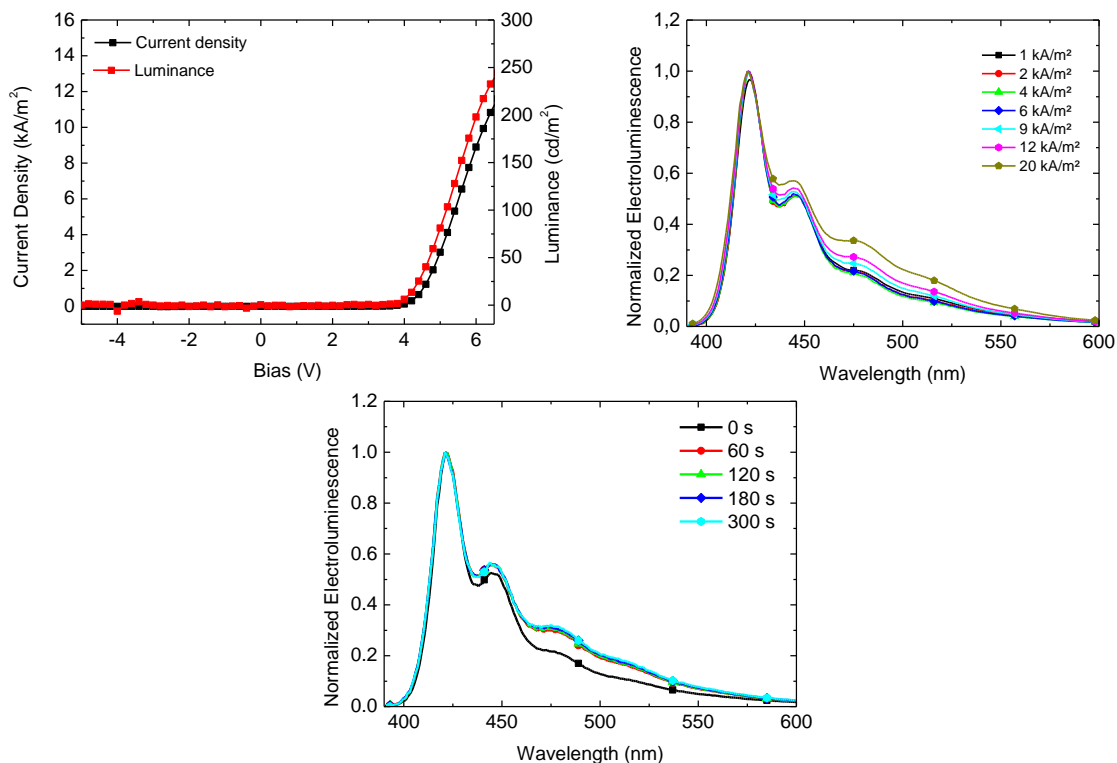


Figure 6.3: J-V-L characteristics (top left), current- (top right) and time dependent (bottom center; recorded at 2 kA/m²) EL spectra of an ITO/PEDOT:PSS/PFO/Ca/Al device

6.3 Photophysical Characterization

UV-Vis and PL characteristics of polymers **P1-P5** in hexafluorobenzene (C₆F₆) as well as in thin films – fabricated by spin coating of the respective solutions on quartz substrates – are listed in Table 6.1. It can be observed that all materials exhibited an absorption and emission behavior as typical for PF^{141,142}. In solution, all absorption spectra showed a broad and structureless absorption feature in the range between 320 nm and 412 nm with the corresponding peak maxima located between 371 nm and 386 nm, which can be ascribed to π - π^* transitions in the respective polymers. PL spectra, in contrast, displayed significantly

structured emission characteristics exhibiting a main peak between 405 nm and 412 nm, accompanied by two vibrational progression bands at higher wavelengths.

Table 6.1. Absorption and emission data of P1-P5 dissolved in C₆F₆ and thin film

		Solution				Thin film		
		λ_{abs}^{max} [nm]	λ_{em}^{max} [nm]	Stokes shift [nm]	ϕ_{PL}^b [%]	λ_{abs}^{max} [nm]	λ_{em}^{max} [nm]	Stokes shift [nm]
P1	<i>fPF-lin</i>	386	412	26	68	388	420	32
P2	<i>fPF-stat</i>	384	411	27	73	388	421	33
P3	<i>fPF-alt</i>	379	410	31	81	387	414	27
P4	<i>fPF-bra(3,5)</i>	376	407	31	78	378	411	33
P5	<i>fPF-bra(3,4,5)</i>	371	405	34	85	384	420	36

^b Fluorescence quantum yield

Absorption results displayed well that a substitution of linear side chains by sterically more demanding branched moieties leads to a significant hypsochromic shift of the absorption maximum as well as of the absorption onset. In particular, for the statistical copolymer **P2**, which comprises a monomer feed ratio of threefold branched : linear sidechains of 1 : 3, a hypsochromic shift of 2 nm was observed compared to the exclusively linear substituted semiperfluorinated homopolymer **P1**. A further enhancement of branched semiperfluorinated moieties from **P3** to **P5** resulted in further increments of the hypsochromic shift which peaked at 15 nm in case of polymer **P5** at which the sterically most demanding, threefold branched semiperfluorinated side chains were attached. The systematic hypsochromic shift can be explained by a reduction of the effective conjugation length due to an increasing twisting between adjacent monomer units upon the introduction of sterically more and more demanding side-chain configurations within the series **P1-P5**^{88,143–146}. The altered conformation within the polymers was also a possible reason for the increasingly blue-shifted PL emission when going from **P1** (412 nm) to **P5** (405 nm). The steadily increasing Stokes shift within the series **P1-P5**, which ranged between 26 nm and 34 nm, as well as the in general stronger hypsochromic shift in absorption than in emission spectra further supports the given explanation since it is known that a twisting of the polymer backbone has a larger influence on the absorption than on emission characteristics⁵⁴. Upon excitation the backbone assumes a more planar configuration than in the ground state. This in turn increases the effective conjugation length compared to the ground state and thus leads to a lower hypsochromic shift of the emission spectra compared to the absorption spectra^{147,148}.

Absorption and emission spectra for all polymers in thin film displayed similar features as in solution (Figure 6.4). All compounds experienced a more or less severe bathochromic shift in absorbance as well as in PL due to solid state effects. Their absorption maxima ranged between 378 nm and 388 nm, while the emission peaks were found between 411 nm and 421 nm. In particular, **P1** and **P2** showed almost identical absorption and emission characteristics as in solution with their respective maxima located at 388 nm (**P1**, **P2**) and at 420 nm (**P1**) and 421 nm (**P2**), respectively. These values indicated a bathochromic shift in the solid state of about 2-4 nm in absorption and of 8-10 nm in emission. With their absorption peak maxima located at 387 nm and 378 nm, which compared to solution are red shifted by 8 nm and 4 nm, respectively, the polymers **P3** and **P4** showed a similar behavior as **P1** and **P2**, whereas their emission maxima showed an only minor bathochromic shift of 4 nm to 414 nm and 411 nm. For **P5**, a pronounced bathochromic shift of 13 nm and 15 nm was observed for the respective absorption (384 nm) and emission maxima (420 nm). The Stokes shifts in thin film were determined to be 27-36 nm.

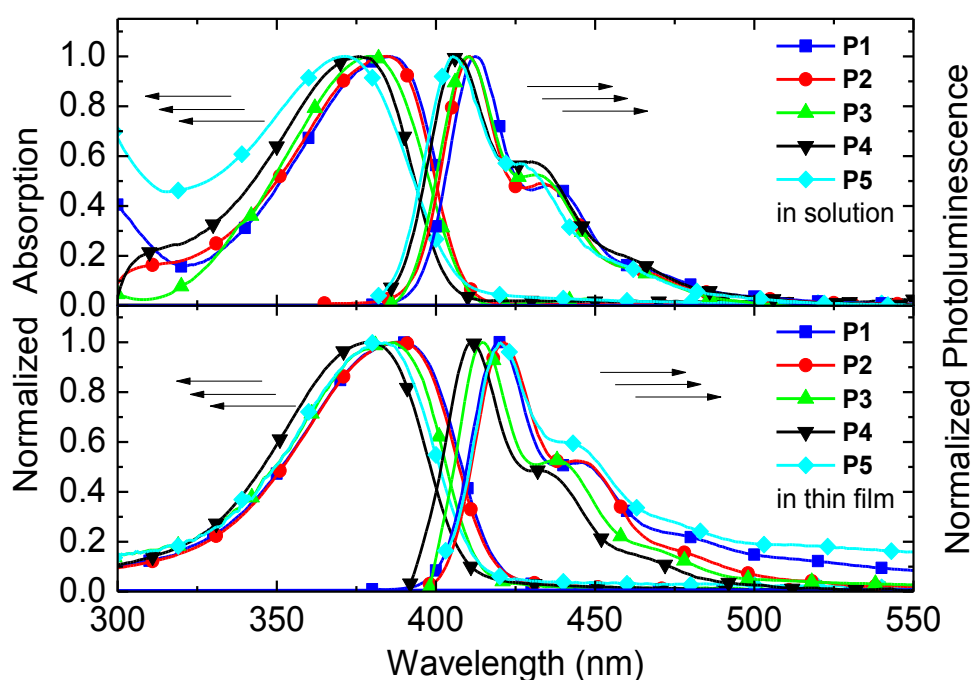


Figure 6.4: Absorption and PL-Emission spectra of P1-P5 in C_6F_6 solution (top) and in thin film (bottom).

The pronounced similarity in thin film between the photophysical characteristics of homopolymer **P1** with linear side chains and the statistical copolymer **P2** containing monomer units with threefold branched side chains at a ratio of 25% can be explained by a similar arrangement of the polymer chains in the solid state. Due to the fact that only a small fraction of the side chains in **P2** were branched, both polymers were expected to exhibit a similar

conformation and the observed bathochromic shift was most likely caused by a planarization of the molecules in the solid state ^{149,150}. In comparison to the thin film spectra of **P1** and **P2**, the emission maximum of **P3** was slightly hypsochromically shifted by 6-7 nm while its absorption maximum was about the same. The reason for this hypsochromic shift only occurring for emission and not in absorption is not completely understood yet. However, Chen et al. made a similar observation while studying the absorption and emission behavior of different crystal structures of PFO. The inconsistent shift between absorption and emission maxima was explained by the existence of crystal domains and it was assumed that, while absorption spectra were influenced by these crystal domains, emission remained largely uninfluenced. The inconsistent shift then arose by different back-bone conformations of the crystalline and the non-crystalline domains ¹⁵¹. The only minor bathochromic shift for **P4** indicated that the polymer exhibited a rather similar conformation in solution as well as in the solid state. Compared to **P1** and **P2** in thin film, **P5** had a similar emission maximum, while in absorption it experienced a minor hypsochromic shift. This was a consequence of the sterically most demanding three-fold branched moieties.

The PLQY for **P1** was found to be 68% which is in line with reported values in literature for PFO ¹⁵². The PLQY improved to 73% for the statistical copolymer **P2**. It further increased to 81% in case of copolymer **P3** but dropped to 78% for **P4** containing the two-fold branched side chains. Polymer **P5** containing the threefold-branched side chains showed the highest PLQY of 85%. There was a tendency of an increasing PLQY with increasing sterical stress exerted by increasingly complex moieties. This indicated that they were more effective in shielding the excited backbone from dynamic quenching with solvent molecules than less bulky ones ³⁷.

6.4 Wettability and Orthogonal Processing

Several investigations were carried out in order to assess the suitability of fPF for orthogonal processing in OLEDs. It should be noted that the following investigations were carried out with the compound **P4**. At first, contact angle measurements were conducted on thin films of fPF, non-fluorinated PF (ADS232GE, American Dye Sources INC.) as well as polar soluble PF (PEGPF) on PEDOT:PSS covered ITO substrates, spin-cast from C₆F₆, toluene and methanol solution, respectively. To determine the contact angles and also the surface energies, measurements with water, diiodomethane, toluene, ethanol and C₆F₆ were conducted. The results of these measurements and the respective surface energies can be found in Table 6.2. From the table it can be seen that fPF exhibited a significantly reduced surface energy of 21.09 mN/m compared to 36.55 mN/m for PF and 58.14 mN/m for PEGPF, while at the same time the contact angles on fPF experienced a noticeable increase for all solvents except C₆F₆.

It was already reported elsewhere ¹⁵³, that the enhanced hydrophobicity and oleophobicity of fluorinated polymers were the reason for this observed behavior. It was further demonstrated that the lower surface energy was a direct consequence of the lowered London dispersion forces caused by the high electronegativity of fluorine ^{154,155}. These facts were supported by increasing contact angles for various non-fluorinated solvents on fPF, which could be attributed to strong surface dipoles in the polymer ¹⁵⁶. Another important observation was that the contact angles for toluene and methanol on fPF were still far below 90° and, therefore, a coating of polymers dissolved in either of these solvents should be possible.

Table 6.2. Contact angles of various solvents on a regular PF derivative, PEGPF and on fPF as well as the corresponding surface energies of the materials.

substrate	Contact angle [°]					Surface energy [mN/m] ¹		
	water	Diiodomethane	toluene	ethanol	C6F6	total	Dispersive part	Polar part
PEGPF	56.3	25.7	12.1	17.6	9.3	58.14	45.91	12.23
PF	89.3	49.0	16.4	35.6	10.4	36.55	34.85	1.07
fPF	92.4	83.2	24.9	37.7	6.2	21.09	15.91	5.18

¹ evaluated by the method of Owens and Wendt ¹⁵⁷.

Besides wettability, another aspect, namely the processability of fPF in combination with the other two polymers on top of each other had to be investigated. First, a possible dissolution of the previously applied film by the solvent of the subsequent applied film had to be excluded. Therefore, thin films of the three polymers were treated with three different solvents, particularly toluene, ethanol and C₆F₆. As a result a rough understanding of the processability of different layer configurations was obtained. In detail, a goniometer was used to deposit drops of the different solvents on top of the thin films of the three polymers. Following that, the thin films were irradiated by UV light at a wavelength of 360 nm and pictures were taken. The results are displayed in Figure 6.5. It is clearly evident that toluene not only dissolved non-polar PF but to some extent PEGPF and fPF as well. Thus, one can expect that successive deposition of a toluene-based solution on an already existing fPF layer is going to partially dissolve the latter. In the case of ethanol no dissolution of the already applied fPF film and non-polar PF film was observed. As expected the dissolution of PEGPF was evident. C₆F₆ dissolved fPF but constituted a poor solvent for non-polar PF and PEGPF. This suggests that fPF which is dissolved in C₆F₆ can be processed on top of non-polar PF and PEGPF. Furthermore, an application of PEGPF on top of fPF seems possible. The partial dissolution of fPF by toluene probably does not allow for the successful formation of well-defined layers.

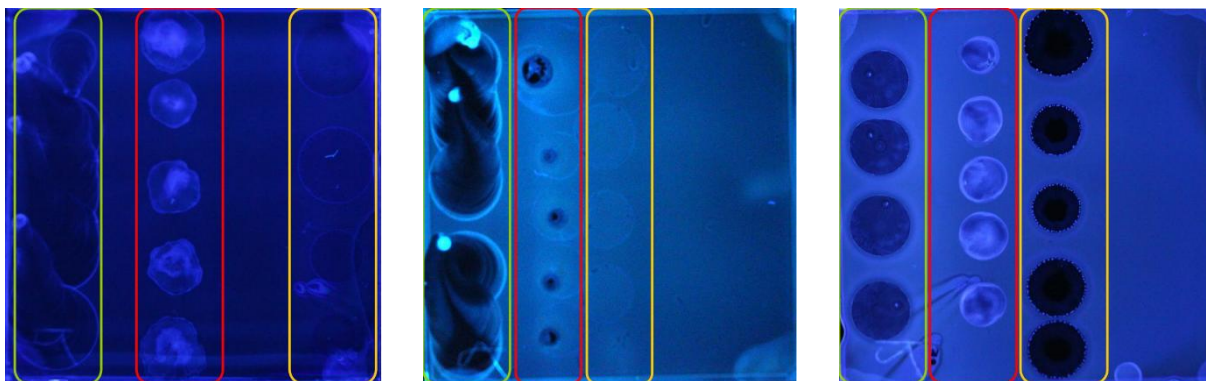


Figure 6.5: Pictures of non-polar PF, PEGPF and fPF films taken during illumination with UV light at 360 nm. The marked areas indicate the positions where the films were stressed with droplets of Toluene (green box), Ethanol (red box), C₆F₆ (yellow box).

The above used method, however, only provided a rough estimate of the possible solvent combinations for the fabrication of multi-layer structures involving fPF. Thus, the formation of smooth and well-defined films had to be confirmed via Atomic Force Microscopy (AFM) height measurements of fPF deposited on top of PEGPF as well as non-polar PF and vice versa. Figure 6.6 shows AFM height images of bilayer structures fPF/PF, fPF/PEGPF, PF/fPF, PEGPF/PF and Table 6.3 contains measured as well as calculated film thickness values. The calculations were performed by subtracting the PEDOT:PSS thickness and the measured thickness for the first layer applied from the total thickness obtained by AFM height measurements. For PEGPF/fPF and PF/fPF the calculated values were in good agreement with those obtained from single layer configurations on PEDOT:PSS, which indicates that, as expected, no dissolution of the preceding layer took place. From the AFM height images in Figure 6.6 it becomes apparent that fPF on PEGPF was able to form a defect free layer similar to a single layer on PEDOT:PSS. However, in case of PF/fPF the formation of distinct holes was observed which could be the result of possible aggregate formation of fPF in solution, since perfluorinated species are known for this behavior in order to minimize interactions with nonfluorinated compounds¹⁵³.

For non-polar PF and PEGPF on fPF, the calculated thickness of the last processed layers was significantly lower than the value measured in a single layer on PEDOT:PSS. In the case of PF, the calculated thickness was negative and, therefore, the overall thickness of the fPF/PF bilayer was lower than the thickness of a fPF single layer. The observed rough surface topography of the fPF/PF bilayer pointed towards a partial dissolution of the already applied fPF layer as the cause for the calculated negative thickness values of the PF layer. For PEGPF on fPF the calculated thickness of PEGPF was only 7 nm. AFM height images revealed that almost no polymer remained on the surface and the formation of small PEGPF islands on fPF was detected. The limited coating ability of fPF by PEGPF was explained by the hydrophobic and oleophobic characteristics of fluorinated compounds.

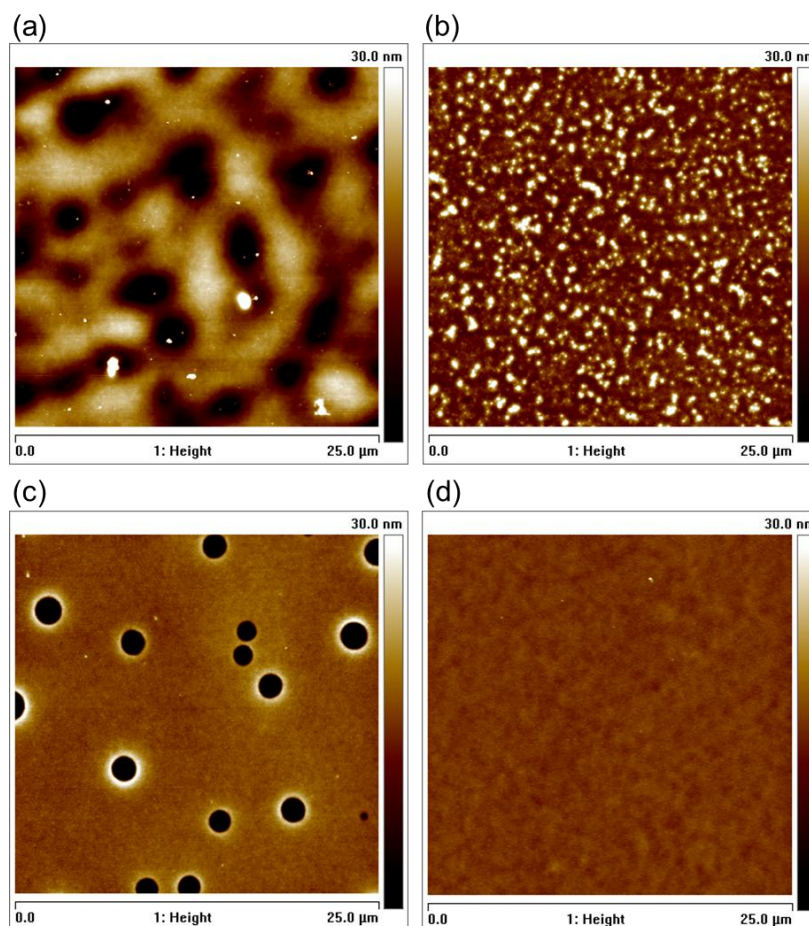


Figure 6.6 AFM surface topography images ($25 \times 25 \mu\text{m}^2$) of fPF/PF (a), fPF/PEGPF (b), PF/fPF (c) as well as of PEGPF/fPF (d) bilayer structures. The surface roughness R_q is 7.3 nm, 4.7 nm, 8.7 nm and 0.7 nm, respectively.

Table 6.3 Measured (**bold**) and calculated thickness values for different layer configurations.

Layer configuration	PEDOT:PSS [nm]	fPF [nm]	PEGPF [nm]	PF [nm]	Thickness [nm]
fPF	64	55	-	-	119
PF	64	-	-	38	102
PEGPF	64	-	76	-	140
fPF/PF	64	55	-	7	126
fPF/PEGPF	64	55	-	-5	114
PF/fPF	64	54	-	38	156
PEGPF/fPF	64	68	76	-	208

6.5 Fluorinated PF as Active Layer in OLEDs

Since the synthesis of **P3** and **P5** in quantities needed for device fabrication proved to be difficult, only **P2** and **P4** were investigated. The EL properties were studied in a standard sandwich geometry: ITO/PEDOT:PSS/**P2,P4**/Ca/Al. Current density and luminance as a function of bias voltage as well as current density dependent spectra for **P2** and **P4** are depicted in Figure 6.7 and Figure 6.8, respectively.

P2 showed a maximum luminance of 37 cd/m^2 at a bias voltage of 7.6 V and a peak efficiency of 0.035 cd/A , while **P4** had its maximum luminance at only 1.8 cd/m^2 at a bias voltage of 8.5 V and a peak efficiency of 0.015 cd/A . Both devices displayed an emission profile similar to the PL spectra in the solid state, with **P2** showing its emission peak at 421 nm and a shoulder at 445 nm and **P4** having the emission peak at 412 nm with a shoulder at 432 nm. The spectra correspond to CIE1931 coordinates of (0.17, 0.11) for **P2** and (0.17, 0.08) for **P4**.

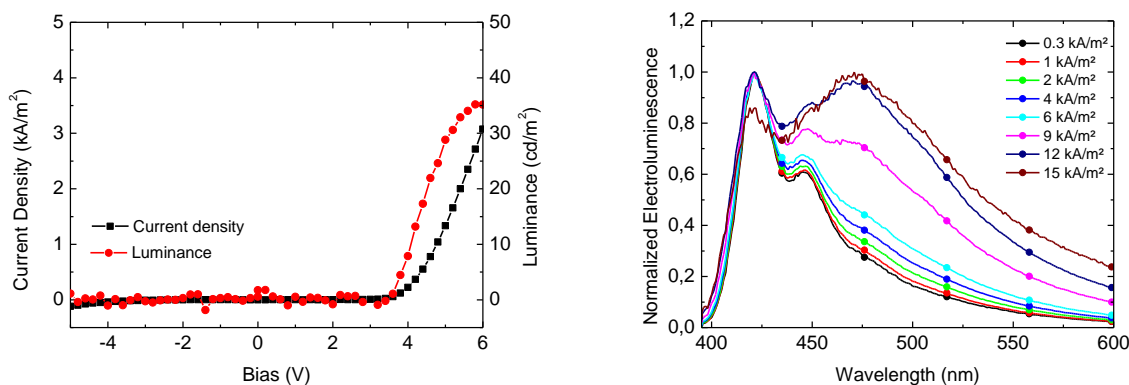


Figure 6.7 J-V-L characteristics of compound **P2** in an ITO/PEDOT:PSS/**P2**/Ca/Al sandwich geometry (left); Current density dependent spectra (right)

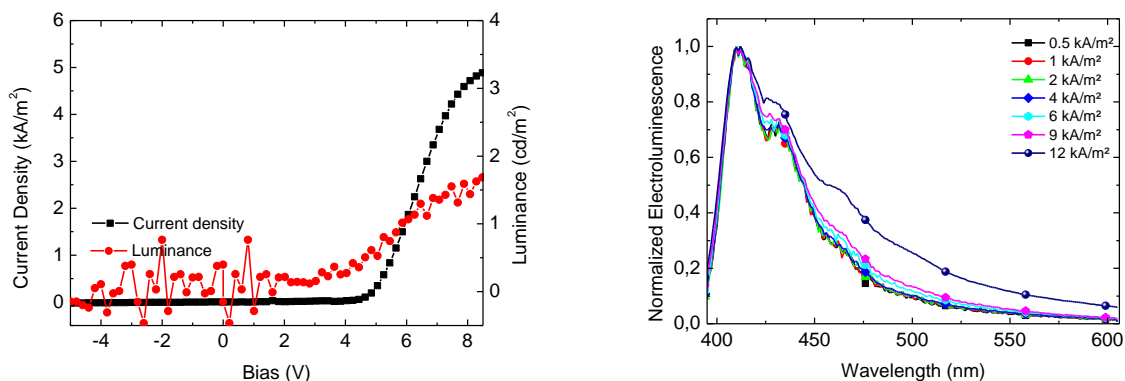


Figure 6.8 J-V-L characteristics of compound **P4** in an ITO/PEDOT:PSS/**P4**/Ca/Al geometry (left); Current density dependent spectra at different applied current densities (right)

The performance with respect to luminance, efficiency and spectral stability, however, was quite poor. Additionally, fast device degradation made the recording of time-dependent spectra almost impossible. One reason for the poor luminance values could be that the emissive layers were too thin. Indeed, profilometer measurements of the two substrates showed that the thickness of **P2** and **P4** was only about 15 nm. Interestingly, both devices displayed similar efficiency values as the reference PFO substrate demonstrated in chapter 6.2.2 which featured about 50 nm of emitting layer thickness. Spectral stability, however, was rather unlikely to be influenced by layer thickness and was an intrinsic material property. To exclude the low thickness values as a reason for poor device performance and distinct spectral instabilities, improved bilayer stack devices were built with the following configuration: ITO/PEDOT:PSS/TFB/**P2**/Ca/Al. TFB was used at the anode side as a hole transporting layer⁶⁸ (see chapter 5.4.2). Profilometer measurements verified that the thickness of **P2** amounted to 40 nm. J-V-L characteristics, as well as current and time dependent spectra are displayed in Figure 6.9.

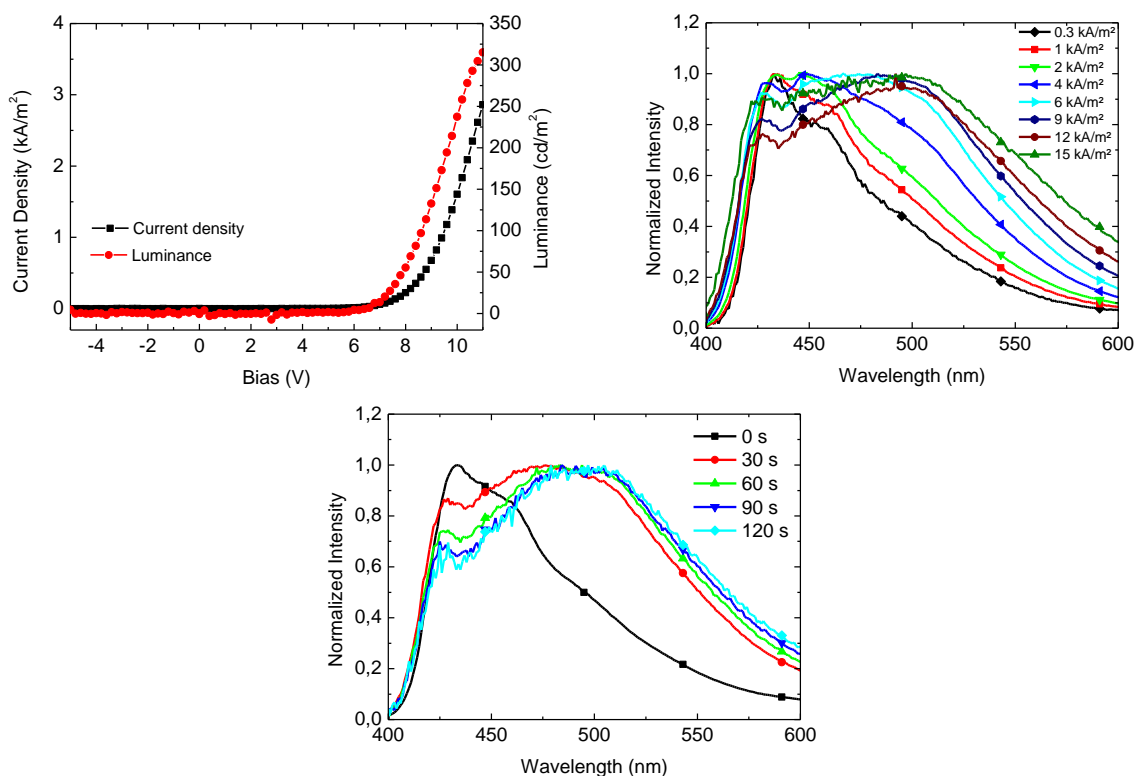


Figure 6.9 J-V-L characteristics of P2 in an ITO/PEDOT:PSS/TFB/P2/Ca/Al bilayer stack (top left); Current density dependent spectra for P2 in a bilayer stack for various current densities (top right); Time dependent spectra taken at a current density of 1 kA/m² over the course of 2 min (bottom)

As illustrated in Figure 6.9 and Table 6.4, the devices were able to achieve a maximum luminance of 315 cd/m² at a bias voltage of 11 V. The best recorded luminous efficiency was about 0.3 cd/A. Compared to the EL spectra observed for single layer devices, a clear contribution of TFB (see chapter 5.4.2) to the spectra for the bilayer device is visible. This

contribution led to a significantly altered emission profile with the peak maximum located at 432 nm and the first shoulder appearing at 457 nm. This emission profile corresponded to the CIE1931 coordinates of (0.18, 0.17). The observed spectral shift to the green at least partially contributes to the enhanced luminance and luminous efficiency values. Even though luminance and luminous efficiency improved drastically, spectral stability remained poor. Time-dependent spectra (see Figure 6.9) showed the appearance of a broad unstructured emission centered around 500 nm already after 30 s. The fact that even at a thickness of 40 nm of **P2** poor spectral stability and fast degradation were observable, eliminated low thickness values as their cause. Lee et al.¹⁵⁸ and Alvey et al.¹⁵⁹ observed a fast degradation for compounds with semiperfluorinated side-chains as well. Within their work the fast degradation of the investigated compounds was attributed to the accumulation of trapped charges and the accompanied induced electrochemical degradation of the polymer.

Table 6.4: Performance characteristics of investigated single- and bilayer devices

organic layer geometry	onset voltage ^a [V]	η^b [cd/A]	max. luminance [cd/m ²]	EL peak ^c [nm]	CIE1931 coordinates ^c x,y
P2	3.6	0,035	37	421	0.165 , 0.105
P4	5.9	0.015	1.8	411	0.166 , 0.077
TFB/P2	5.5	0.293	315	432	0.179 , 0.171

^a voltage at a luminance of 1 cd/m²; ^b value of maximum efficiency; ^c at a current of 10 mA

6.6 Charging Effects as Source for Spectral Instabilities

In order to verify if the observed degradation is caused by charging effects in the materials, pulsed charging as described in chapter 4.3.3 was performed on ITO/PEDOT:PSS/**P2**/Ca/Al and ITO/PEDOT:PSS/PFO/Ca/Al devices. The results are shown in Figure 6.10. Green lines indicate pulses with a -10 V bias, while brown lines mark +10 V biased pulses. +10 V pulses directly following -10 V pulses are marked with the same symbol. From Figure 6.10 it is evident that applying the pulses led to a degradation of the device pulse by pulse in case of PFO. Degradation between successive pulses was also observed for **P2**. However, it can be seen that the second -10 V pulse yielded a higher relative EL than the first +10 V pulse. The same trend can be observed in the case of the third -10 V pulse which again showed higher EL values opposed to the second +10 V pulse. In order to exclude that the results stem from an uncertainty caused by the measurement setup, a check with two further devices was conducted. They demonstrated a similar behavior, thus ruling measurement uncertainty out as the cause for this behavior.

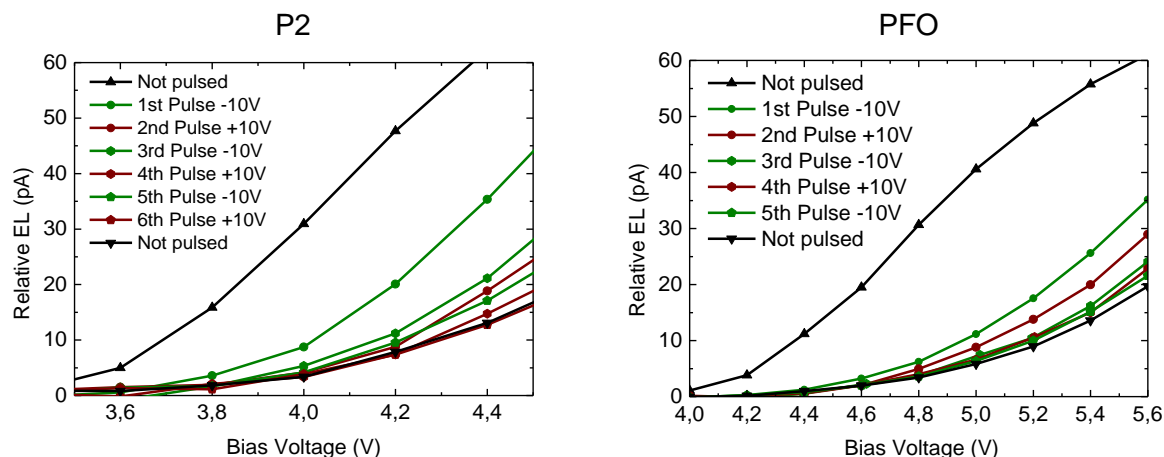


Figure 6.10: Relative EL versus bias for pulsed characterizations performed for compound P2 (left) and PFO (right) in an ITO/PEDOT:PSS/P2,PFO/Ca/Al device geometry. -10 V pulses (green) and +10 V pulses (brown) were applied consecutively.

The explanation given by Lee et al.¹⁵⁸ who stated that fluorinated side-chains form effective electron-traps seems to confirm the attained results. However, Giebeler et al.¹⁶⁰ found that charging of bulk traps leads to the buildup of a counter field. The improvement in relative luminescence in this case is explained by a discharging of the bulk that leads to the disappearance of the electric counter field and, thus, to a more favorable energy level alignment at the electrode interfaces. Since both explanations do not exclude each other, it seems likely that charging of the side chains occurred. This charging not only led to an electron-trap induced degradation but also to a less favorable energy level alignment. From that perspective, it becomes obvious that discharging the trapped electrons restores the energy level alignment to the condition prevalent before charging, at least temporarily.

6.7 Conclusion

In this chapter a series of linear and branched semiperfluorinated side chain configurations of PFs were characterized by photo physical, morphological and optoelectronic studies. All polymers within this series had an emission profile similar to PFO. In solution it was shown that polymers with sterically more demanding side chain configurations showed a blue-shifted emission and absorption behavior compared to the less demanding configurations. The blue-shifting tendency in case of more demanding side-chains was also observable in thin film. Additionally, it was observed that sophisticated side chains showed higher PLQY values compared to the less sophisticated configurations. The suitability of the investigated polymers in an orthogonal solution process was revealed by contact angle and AFM measurements, where fPF was found to form smooth and sufficiently thick films when applied to a layer of PEGPF. Electro-optical studies were carried out with single and bilayer devices built from **P2** and **P4**. Single layer devices demonstrated a deep-blue EL emission similar to PL in thin film

while luminescence, efficiency as well as stability were less satisfying. Bilayer devices with increased emitting layer thickness values showed better luminescence and luminous efficiency values compared to single layer devices, but at the cost of a green shift in emission and without improving the poor spectral stability. By introducing pulsed biasing of the devices it was shown that a possible charging, induced by the fluorinated side-chains, is likely to be the reason for the poor luminance and spectral stability. Thus, further work is required before this material class can be employed successfully in orthogonally processed multilayer PLEDs.

7 Investigations on Pegylated Polyfluorene

In the previous chapter, a novel polyfluorene-type polymer with semiperfluorinated side chains for application in an orthogonal solvent process from a fluorinated-/non-fluorinated solvent system was presented. In this chapter PEGPF, a polyfluorene compound with poly(ethylene glycol) (PEG) side chains, is studied. These PEG side chains allow for dissolving the polymer in polar solvents like methanol and make the material suitable for an orthogonal solvent process from a polar/nonpolar solvent system. In addition it was demonstrated by Deng et al.¹⁶¹ that PEG can reduce the electron injection barrier at the cathode side and Niu et al.¹⁶² demonstrated that PEG can be a good surfactant. Moreover, these beneficial properties can compensate for the insulating properties of PEG¹⁶³. These discoveries led to a first successful application of PEGPF as ETL by Trattnig et al.¹¹¹.

The PEGPF (see Figure 7.1) under investigation was of the same structure as the one used by Trattnig et al.¹¹¹, but the number average molecular weight for the presently investigated PEGPF was considerably increased to 66,100 g/mol as opposed to 48,200 g/mol. Compared to the lower molecular weight material, similar photophysical properties can be expected, while solubility and morphological properties¹⁶⁴ might differ due to the longer chain lengths. Studying the applicability of the higher molecular weight PEGPF in an OLED is the scope of this chapter.

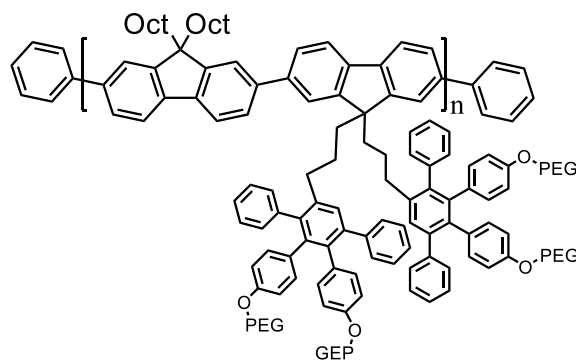


Figure 7.1: Chemical structure of PEGPF

7.1 Photophysical Characterization

UV-Vis and PL spectra of PEGPF in methyl alcohol (MeOH) solution and in thin film are depicted in Figure 7.2. in solution as well as in thin film. PEGPF exhibited a structureless absorption feature in the range of 325 nm to 420 nm peaking at 400 nm, which can be ascribed to a π - π^* transition in the polymer. The emission characteristics were similar to PFO demonstrated in chapter 6.2.1. In MeOH solution, the emission ranged from about 400 nm to

525 nm, displaying a maximum at 423 nm. Vibrational progressions was found at 445 nm and 475 nm in MeOH solution, and similar features were observable in thin film, however, bathochromically shifted by approximately 4 nm. The Stokes shift determined in MeOH solution amounted to approximately 23 nm, while 26 nm was observed in thin film. The PLQY was determined to be 74% in MeOH. A comparison with PFO (see chapter 6.2.1) revealed remarkably similar photophysical characteristics, which is to be expected since PEGPF and PFO had identical backbones.

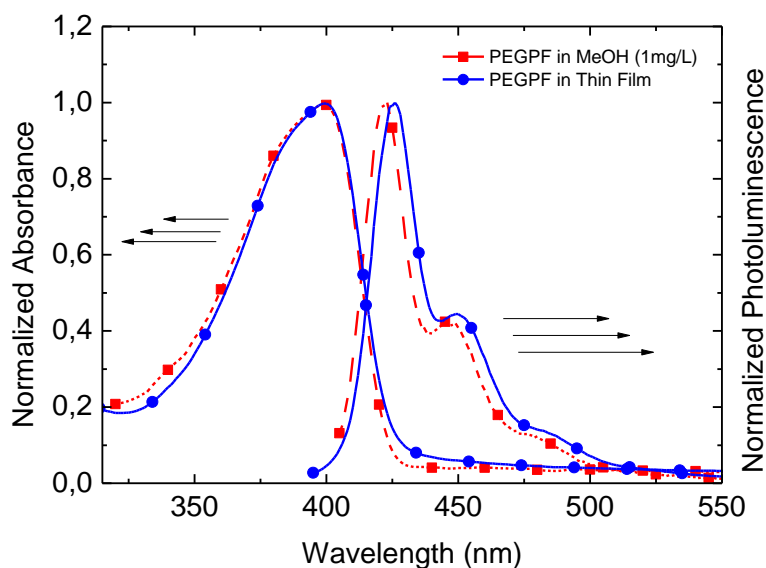


Figure 7.2: UV-Vis and PL spectra of PEGPF in MeOH (dashed red line) and in thin film (blue line)

7.2 Device Characteristics in a Single Layer Assembly

To assess the applicability of PEGPF in an OLED, the EL properties of PEGPF were studied in a standard single layer ITO/PEDOT:PSS/PEGPF/Ca/Al device geometry. For this reason, J-V-L characteristics as well as current density and time dependent EL spectra were recorded. They are depicted in Figure 7.3. The devices exhibited a low onset voltage of approximately 3.2 V with a maximum luminance value of 55 cd/m² achieved at a bias voltage of 5.8 V, while efficiency was rather poor with only 0.005 cd/A. Emissive layer thickness was determined to be 50 nm and was therefore excluded as a cause of the poor efficiency values. Current density dependent EL spectra revealed a similar deep-blue emission profile as found in thin film PL, having the emission maximum located at 424 nm and a shoulder at 448 nm. The emission profile corresponded to CIE1931 coordinates of (0.17, 0.09). Time dependent spectral stability of PEGPF evidenced a gradual increase of emission in the mentioned range between 500 nm and 600 nm over the course of five minutes for PEGPF, which was attributed to the formation of a Keto-Defect emission ¹⁴².

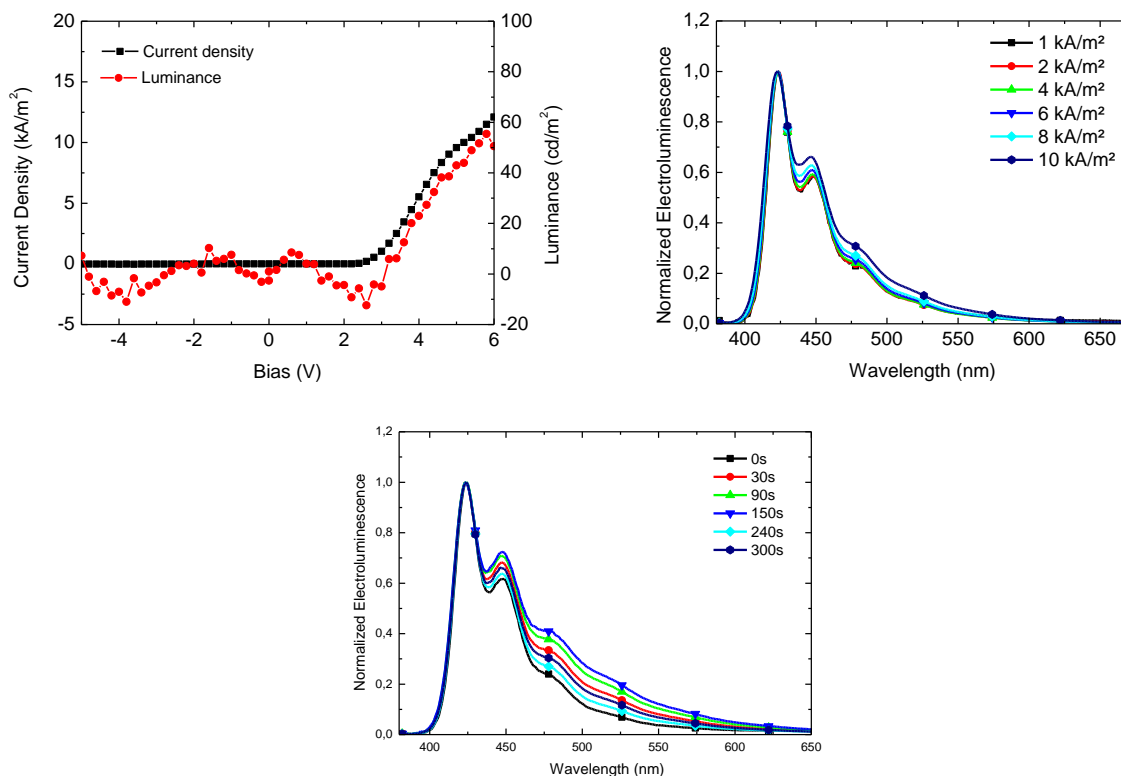


Figure 7.3 J-V-L characteristics (top left), current density dependent EL spectra (top right) and time (bottom center) dependent EL spectra (at 2 kA/m²) in an ITO/PEDOT:PSS/PEGPF/Ca/Al configuration

With an EL located in the desired deep blue region, PEGPF appears to be promising for application in an OLED. At the same time, however, low luminance and efficiency values indicate that further device optimization is required. Spectral stability was found to be in-line with the results obtained for PFO (see chapter 6.2).

7.3 Bilayer devices

While the single layer PEGPF devices demonstrated in the last chapter featured EL emission in the favorable deep-blue spectral range, the observed low luminance values accompanied with high current densities indicate the presence of an unfavorable alignment of the HOMO level of PEGPF with the work function of PEDOT:PSS causing an imbalanced charge carrier injection¹¹¹. Therefore, a thin and insoluble TFB layer which acts as a hole transport layer was applied in a bilayer device with an ITO/PEDOT:PSS/TFB/PEGPF/Ca/Al (**device a**) assembly as specified in Chapter 5.4.2. The thickness of TFB and PEGPF was 4 nm and 60 nm, respectively. As illustrated in Table 7.1, a peak luminance of 1573 cd/m² at an applied bias of 6 V was observed, while the maximum luminous efficiency attained 0.11 cd/A. The onset of the EL emission was detected at 3 V. These findings represent a 28.6-fold enhancement of

the maximum luminance values and even a 36.7-fold increase with regards to the peak luminous efficiency when compared to the ITO/PEDOT:PSS/PEGPF/Ca/Al single layer OLED presented in the last subchapter. At the same time there was a decrease in the onset voltage by 0.2 V. Based on these facts it can be inferred that a more balanced charge carrier injection was prevalent in **device a**.

Current density dependent EL spectra demonstrated a shift of the peak emission from 497 nm at a current density of 0.1 kA/m², to 469 nm at 0.3 kA/m², until it finally approached 438 nm at 4 kA/m² where it remained even if higher current densities were applied. Similarly, the FWHM of the EL spectrum amounted to 127 nm at 0.1 kA/m², 117 nm at 0.3 kA/m² and to 78 nm at a current of 12 kA/m². Compared to the EL spectra demonstrated in chapter 7.2 for an ITO/PEDOT:PSS/PEGPF/Ca/Al single layer OLED where the spectra at different current densities remained largely the same, a clear change in the EL emission behavior was observed for **device a**.

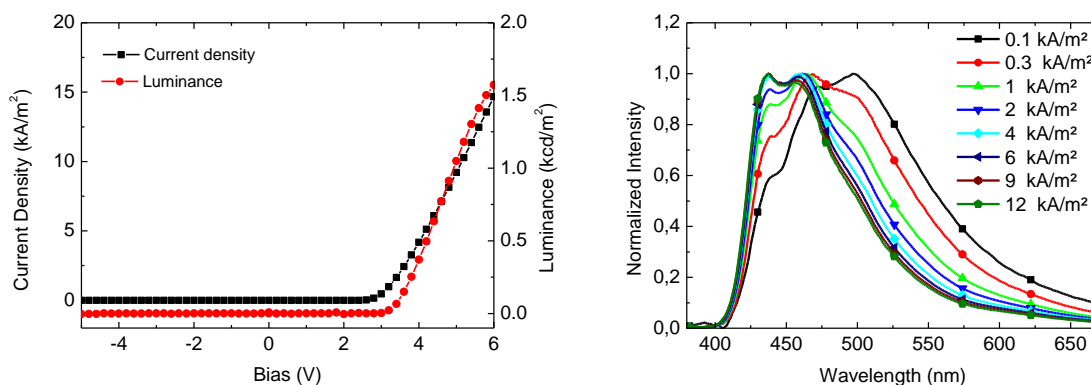


Figure 7.4: J–V–L characteristics (top left) as well as current density dependent EL spectra (top right) of device a

7.3.1 Origin of the Current Density Dependent Change of the Emission Behavior

The exhibited current density dependent EL emission behavior is intriguing and requires a more in depth analysis. For this reason, the current density dependent EL spectra of **device a** were replotted in Figure 7.5. In this figure the individual EL emission maxima are marked by vertical lines. The EL spectra between 2 kA/m² and 12 kA/m² did not exhibit any large changes and were omitted. At higher current densities, an agreement between the vibronic progressions and the observed EL emission peaks, which were recorded at 460 nm and 499 nm for lower current densities, was evident.

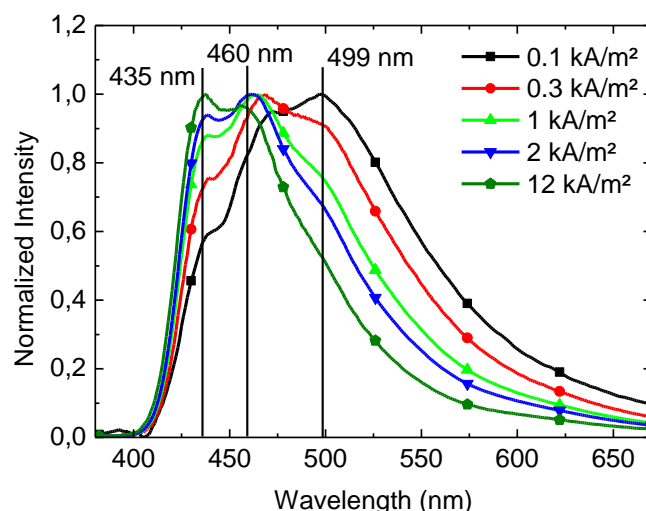


Figure 7.5: Replot of the current density dependent EL spectra of device a where the vertical lines indicate the individual peak emissions

The compliance of the peak emissions at 460 nm and 490 nm at lower current densities with the vibronic progressions observed at higher current densities strongly suggests that TFB and PEGPF were both contributing to the emission, while the shifting emission maxima alluded to a movement of the recombination zone. To confirm a movement of the recombination zone as the origin of the occurring shift of the current density dependent EL spectra, it was necessary to identify if TFB can act as an at least partial filter for emission originating from PEGPF (since TFB is applied before PEGPF). Therefore, a possible spectral overlap between the UV-VIS spectrum of TFB and the PL spectrum of PEGPF in thin film needed to be studied. For this reason, the UV-Vis of TFB and PL spectra of PEGPF in thin film are illustrated in Figure 7.6. A clear overlap between the PL spectrum of PEGPF and the UV-Vis spectrum of TFB in the range of approximately 400 nm to 433 nm is evident. Hence, TFB can act as a filter that attenuates or even extinguishes the peak emission of PEGPF.

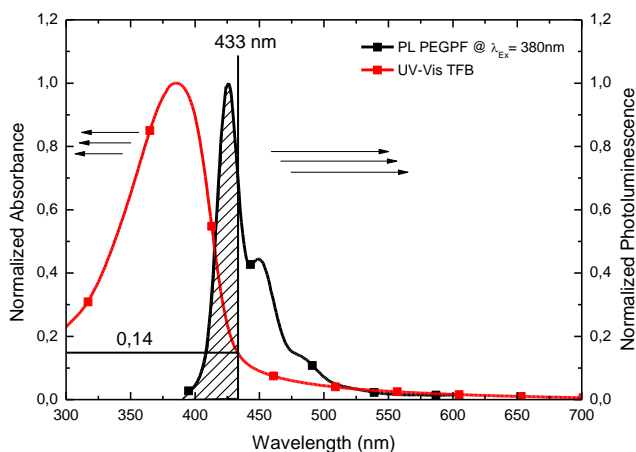


Figure 7.6: UV-Vis and PL spectra of PEGPF and TFB in thin film.

As mentioned before, a comparison between the current density dependent spectra of **device a** and the EL spectra of TFB and PEGPF are required. The EL spectra for an ITO/PEDOT:PSS/TFB or PEGPF/Ca/Al OLED, as well as EL spectra of **device a** acquired at (a) 0.1 kA/m² and (b) 12 kA/m² are depicted in Figure 7.6. The spectrum of **device a** collected at a current density of 0.3 kA/m² featured an EL emission peak at 460 nm and a broad emission characteristic that neither matched the EL emission shape of PEGPF nor of TFB. At a current density of 12 kA/m², the peak EL emission of **device a** occurred at 435 nm which coincided with the peak EL emission of the TFB. Furthermore, the shape of the EL emission of **device a** at 12 kA/m² bore a remarkable resemblance to the shape of the EL spectrum of TFB.

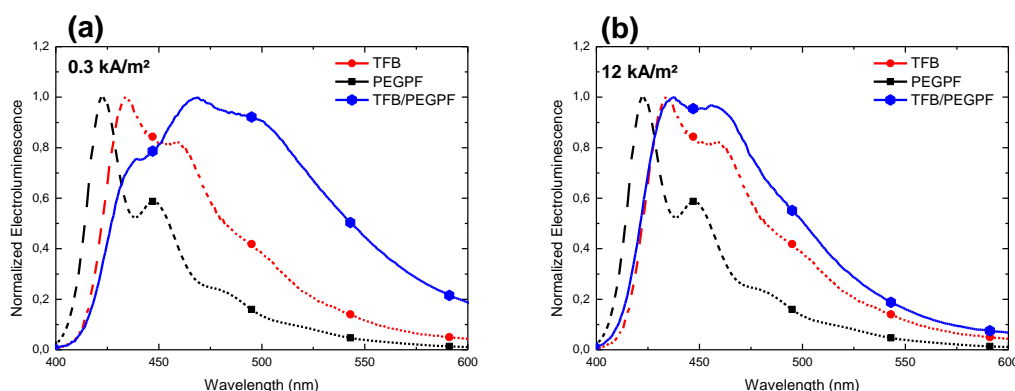


Figure 7.7: EL spectra of TFB (30 nm) and PEGPF (60 nm) in a single-layer assembly taken at a bias voltage of 4 V. Additionally, current density dependent EL spectra of device a taken at (a) 0.3 kA/m² and (b) 12 kA/m² are included

Inferring from the attained results, at low current the recombination zone in **device a** remained to a great extent in PEGPF and the observed filter effect of TFB cut off the peak emission of PEGPF, thereby distorting its EL spectrum. Increasing the current densities led to a shift of the recombination zone from PEGPF into TFB, which in turn caused the shape of the emission to more closely align with the shape of TFB until the peak emission of **device a** finally coincided with the peak emission of TFB. At this point, the recombination zone had moved almost exclusively into TFB and, compared to pure TFB, only minor contributions from PEGPF to the spectrum of **device a** were visible as a slightly broadened emission width.

7.3.2 Factors that Impact the Location and Movement of the Recombination Zone

A device architecture that allows for a partial or even complete shift of the recombination zone between two layers is highly desirable. Therefore, further studies on the factors impacting the observed movement of the recombination zone were warranted. First, it was studied how the movement of the recombination zone depends on the efficiency of the employed EIL, since a

change of the charge carrier balance in the device should pin the recombination zone at a different position. For that reason, the material used as the EIL was changed, replacing Ca by the highly efficient Cs_2CO_3 . The so created **device b**, an ITO/PEDOT:PSS/TFB/PEGPF/ Cs_2CO_3 /Al assembly with J-V-L characteristics as well as current density dependent EL spectra visible in Figure 7.8 and key performance data summarized in Table 7.1.b, was then used to study the impact of the EIL. Layer thicknesses of TFB and PEGPF were verified to amount to 4 nm and 60 nm, respectively, while the evaporated Cs_2CO_3 layer had a thickness of approximately 1.5 Å. J-V-L characteristics revealed a turn-on voltage of 2.7 V and a peak luminance of 6170 cd/m^2 at an applied bias of 7 V. Highest attained luminous efficiency was ascertained at 0.6 cd/A at 7 V. Compared to **device a**, peak luminance and luminous efficiencies experienced a 4- and 6-fold increase, respectively. This confirmed that Cs_2CO_3 was a significantly better EIL. Current density dependent EL spectra revealed a shifting EL emission peak from 462 nm at 0.1 kA/m^2 to 438 nm in case of current densities above 10 mA. The FWHM of the current density EL spectra amounted to 112 nm at 0.1 kA/m^2 , 100 at 0.3 kA/m^2 and remained stable at 87 nm for current densities above 1 kA/m^2 , constituting a systematic decrease with increasing current densities. A comparison with the current density dependent EL spectra of **device a** displayed in Figure 7.4 revealed that, with the exception of the absence of an EL emission peak in the proximity of 499 nm, both shared the same tendency regarding the shift of the peak emission to shorter wavelength and the narrowing of the FWHM with increasing current densities.

The observed absence of an EL emission peak in the vicinity of 499 nm was likely due to the better performing Cs_2CO_3 EIL which resulted in the presence of more electrons in the device even at lower voltages. As a consequence the recombination zone was already closer to the TFB layer at the onset voltage and, therefore, **device b** displayed more emission from TFB at the onset than **device a**. The fact that **device a** and **device b** displayed a similar evolution of the current density dependent EL spectra indicated that both devices experienced a similar movement of the recombination zone, albeit starting at different positions.

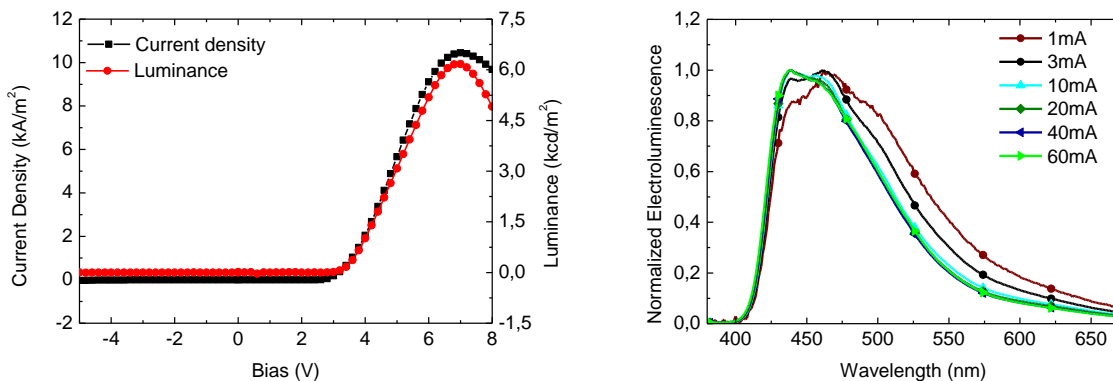


Figure 7.8: J-V-L characteristics and current density dependent EL spectra of device b

In a second step, the dependence of the recombination zone movement on the ratio of the TFB and PEGPF layer thicknesses was investigated by changing the ratio from 15 (4 nm TFB; 60 nm PEGPF) to 1.2 (25 nm TFB; 30 nm PEGPF) (**device c**). **Device c** featured an ITO/PEDOT:PSS/TFB/PEGPF/Cs₂CO₃/Al assembly with corresponding J-V-L characteristics and current density dependent EL spectra depicted in Figure 7.9, with key parameters detailed in Table 7.1.c.

Onset of the EL emission was recorded at 2.6 V, while peak luminance attained 3105 cd/m² at 6V and luminous efficiency achieved 0.37 cd/A at an applied bias of 4.6 V. In comparison to **device b**, this represented a decrease in peak luminance and luminous efficiencies of 50% and 61%, respectively. This dramatic decrease in peak luminance and luminous efficiency for **device c** was rather unexpected and was not solely attributable to the decreased total layer thickness, which amounted to 55 nm, thus only 9 nm less than **device b**. Regarding the current density dependent EL spectra, it was found that the peak emission of the current dependent EL spectra of **device c** moved from 434 nm at 0.05 kA/m² to 430 nm at 12 kA/m². At lower current densities the current dependent EL spectra were characterized by shoulders at approximately 460 nm and 500 nm which started to vanish until they completely disappeared for current densities above 4 kA/m². At the same time, the FWHM of the current dependent EL spectra gradually decreased from 62 nm at 0.05 kA/m² to 44 nm at 12 kA/m². Remarkably, the peak emission at lower current densities observed for **device b** at 460 nm completely vanished. The absence of the peak combined with the disappearing shoulders indicated that even at the onset of the device, the recombination zone was for the most part located in the TFB layer. Consequently, only traces of PEGPF were observable, which disappeared at higher current densities when the recombination zone was completely located in the TFB layer. Knowing that the location of the recombination zone was well within the TFB layer, it was reasonable to attribute the worse than (by the decrease in layer thickness) anticipated performance of **device c** to the close proximity of the recombination zone to PEDOT:PSS, which is known to lead to luminance quenching^{165,166}.

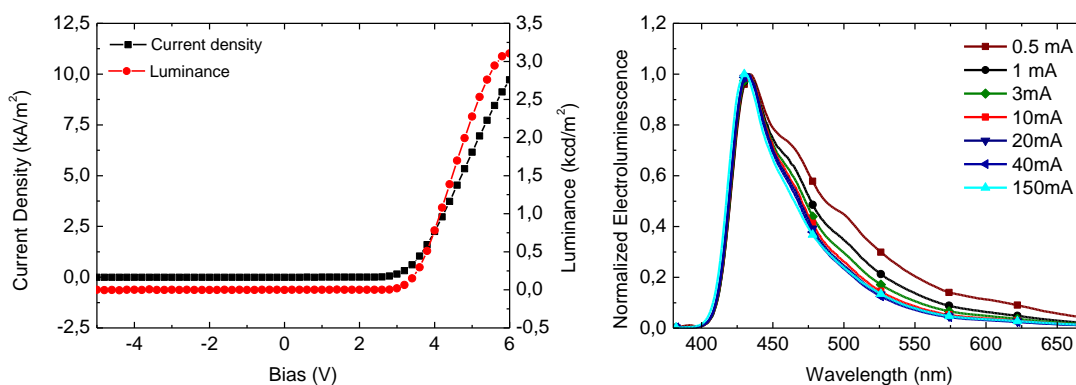


Figure 7.9: J-V-L characteristics and current density dependent EL spectra of device c

7.3.3 Consequence of the Movement of the Recombination Zone

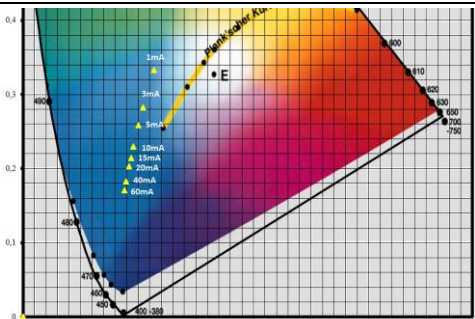
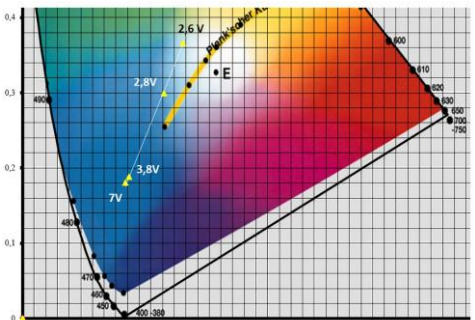
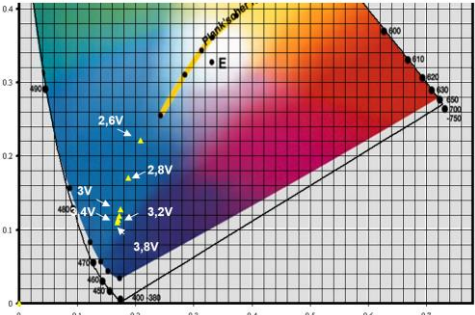
In the last paragraphs, the movement of the recombination zone between the layers of several bilayer devices consisting of TFB and PEGPF was demonstrated by means of detailed studies of recorded current density dependent EL spectra. Significant changes of the emission spectra were observed. As a result, these devices showed an emission color dependent on the current density/applied bias. The associated color of the emission spectra at several biases/current densities for **device a**, **device b** and **device c** is shown in Table 7.1. For all devices the change of the emission color occurs along a line in the CIE1931 diagram. The starting- and end points of this line, which are represented by the first detectable emission and the point where no further change of the emission color was detectable, are specified for all devices in terms of CIE1931 coordinates.

Emission color of **device a** started from (0.208,0.347) and changed to (0.178,0.171), **device b** experienced a change of the emission color from the onset of the emission at (0.275,0.366) to (0.176,0.180) and **device c** exhibited an emission color change from (0.209,0.221) to (0.169,0.110). It is important to note that both, **device a** and **device b**, displayed an initial emission color close to the white point (0.333,0.333). Therefore, in case of **device a** and **device b** the emission color was tunable from close to white to a sky-blue emission color, while **device c** exhibited limited color tuning capabilities that only allowed for a tuning between different shades of blue.

7.3.4 Bilayer devices - Summary

In short it was demonstrated that a mobile recombination zone was realized for bilayer device assemblies featuring TFB and PEGPF. Detailed studies proved that the initial location and the mobility of the recombination could be altered by tuning the amount of injected electrons via a proper EIL as well as by choosing the ratio between the TFB and PEGPF layer thicknesses accordingly. In doing so, the emission color of the investigated devices was tunable in dependence of the applied bias/current density. The range of this tuning capabilities was determined by the respective device assembly. The best device showed a tunable emission color starting from close to white (0.275,0.366) across several shades of blue up to (0.176,0.180).

Table 7.1: Device data for bilayer devices consisting of different TFB and PEGPF configurations

organic layer geometry	onset voltage ^a [V]	η^b [cd/A]	max. luminance [cd/m ²]	CIE1931 coordinates ^c x,y
a TFB(4nm)/PEGPF(60nm)/Ca(10nm)/Al	3	0,1	1573	
b TFB(4nm)/PEGPF(60nm)/Cs ₂ CO ₃ (1,5A)/Al	2,7	0,6	6170	
c TFB(25nm)/PEGPF(30nm)/Cs ₂ CO ₃ (1.5A)/Al	2,6	0,37	3105	

^a voltage at a luminance of 1 cd/m²; ^b value of maximum efficiency; ^c at a current of 10 mA

7.4 Voltage Dependent Color Tuning

In chapter 7.3, different bilayer assemblies comprised of TFB and PEGPF with the capability to move the recombination zone from PEGPF at lower current densities to TFB at higher current densities were demonstrated. Therefore, the investigated device assemblies exhibited the property to tune the emission color in accordance with the applied bias.

In literature, several color-tunable OLEDs manufactured from small molecules¹⁶⁷, polymers^{132,168} or polymer blend systems¹⁶⁹ have been presented. However, to date either maximum luminance remained low, efficiencies were poor or the bias voltage required for a full switch was rather high. To make matters worse, most presented systems rely on specific material

combinations and, therefore, allow the realization of switchable systems between only two colors. Certainly, the availability of a well-performing color tunable OLED stack for application in display and lighting technologies that at the same time is flexible (with regards to the tunable color range) and solution processable is desirable. One way to achieve these requirements would be to design a bilayer device with the capability to switch the recombination zone between the two layers. The flexibility in regard to the tunable color range would then be realized by blending dyes into one of the two layers. Since the OLED stacks introduced in chapter 7.3 demonstrated a moveable recombination zone, it was investigated if the recombination zone is still moveable after the addition of a dye in one layer.

7.4.1 Orange – Blue Emitting PPDB Blend Systems

A first step constituted the addition of poly(perylene-co- diethynylbenzene) (PPDB), an orange-emitting dye, to the TFB layer of an ITO/PEDOT:PSS/TFB/PEGPF/Cs₂CO₃/Al assembly. PPDB was first presented by Tasch et al.^{170,171} who showed that efficient FRET (see chapter 2.5.1) from a blue-emitting host to an orange-dye can be realized by blending the dye at low weight percentages into the polymer matrix. The chemical structure of PPDB is shown in Figure 7.10.

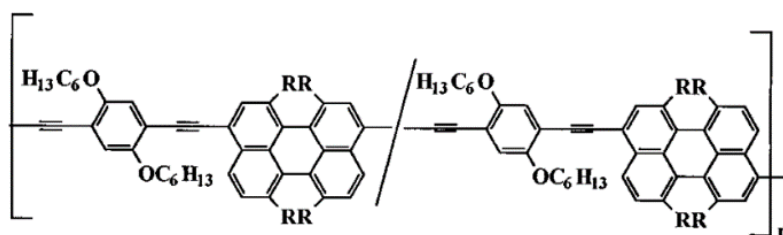


Figure 7.10: Chemical structure of PPDB, where R denotes phenoxy-t-butyl¹⁷²

Photophysical characterization

Figure 7.11 shows UV-Vis and PL characteristics of PPDB in thin film. The UV-Vis spectrum exhibited a structured absorption band ranging from 350 nm to 600 nm, characterized by an absorption peak at 550 nm, a shoulder at 520 nm as well as a local maximum at 390 nm. The PL emission was structureless and started at approximately 550 nm, spanning well into the red region with a peak emission at 596 nm.

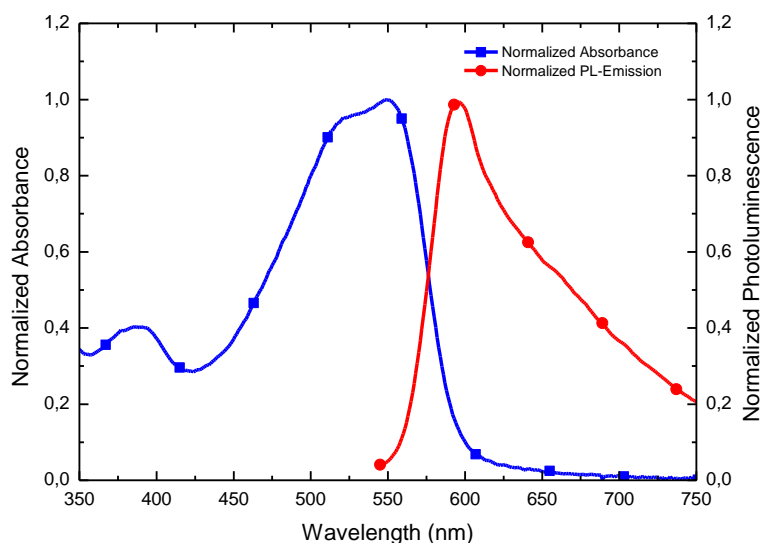


Figure 7.11: UV-Vis and Photoluminescence spectra of PPDB in thin film

The main factors that influence the effectiveness of the FRET in a blend system is the spectral overlap of the emission spectrum of TFB and the absorption spectrum of PPDB. Therefore, absorption and emission characteristics of these materials are depicted in Figure 7.12, where the overlap between the two is indicated by the shaded area. It is evident that there was a good overlap of the absorption of PPDB in the emission range of TFB between 400 nm and 600 nm. Consequently, an efficient energy transfer can be expected.

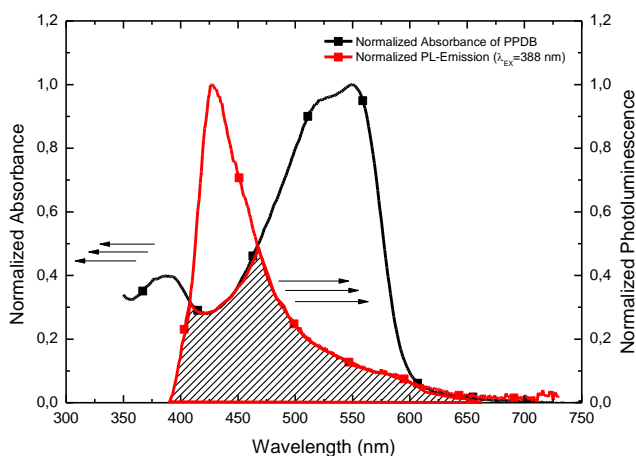


Figure 7.12: UV-Vis and PL spectra of TFB and PPDB respectively in thin film. Spectral overlap is indicated by the shaded area.

Device characterization

In the last chapter about photophysical characterization it was found that an efficient FRET between the donor TFB and the acceptor PPDB can be expected. To investigate if PPDB leads to a voltage/current density dependent tunability between orange and blue, a device with an ITO/PEDOT:PSS/TFB:PPDB/PEGPF/Cs₂CO₃/Al (**device d**) structure was assembled. PPDB was blended into TFB at a concentration of 1 wt% of TFB. The reason for doing so was that Tasch et al.¹⁷⁰ revealed that concentrations of PPDB at 1 wt% of the host material result in a strong attenuation of the host emission, while at the same time strong PPDB emission became apparent. The thickness of the TFB:PPDB and PEGPF layers was measured and amounted to 20 nm and 60 nm, respectively. High TFB layer thickness was achieved by exploiting the fact that TFB is not soluble in MeOH, the solvent of PEGPF. Consequently, no dissolution of the previously applied TFB layer is possible.

Results of J-V-L characterization as well as voltage dependent EL spectra are depicted in Figure 7.13 and important electro-optical properties are summarized in Table 7.2. A turn-on voltage of 2.7 V was recorded and the achieved peak luminance was 2270 cd/m² at a bias voltage of 5.6 V. Peak efficiency was observed at a bias of 4.1 V and amounted to 1.06 cd/A at 4.1 V. Voltage dependent EL spectra exhibited a peak emission of 570 nm at 2.4 V, which moved to 477 nm at 3 V where it remained for higher voltages. Furthermore, a shoulder at 2.4 V was observed at 470 nm. This shoulder moved to 450 nm at 2.6 V and to 439 nm at 3 V where it persisted for higher bias voltages. In addition, the intensity of the emission from the shoulder increased with higher applied voltages until it peaked at 5 V, followed by a decrease. The peak located at 570 nm experienced a steady decrease from 2.4 V to higher voltages, first converting into a shoulder before it completely vanished in case of biases beyond 5 V.

Voltage dependent EL spectra showed a shift from a predominantly red emission at lower voltages to a blue emission at higher voltages. This revealed that a color change between different emission colors is achievable (see CIE1931 diagram in Table 7.2). In analogy to chapter 7.3, the shift of the shoulder to 439 nm accompanied by an increasing intensity indicates that the recombination zone experienced a voltage dependent shift towards TFB.

However, it is important to note that a rather strong emission originating from TFB at 439 nm was detectable at higher voltages while no emission ascribable to PPDB was detected. This was especially troubling, since photophysical investigations revealed that an efficient FRET was to be expected and, in this case, only a weak contribution from the TFB host should have been visible. As a consequence, the observed change in the emission color could not be attributed to the change of the recombination zone and for unknown reasons no FRET occurred.

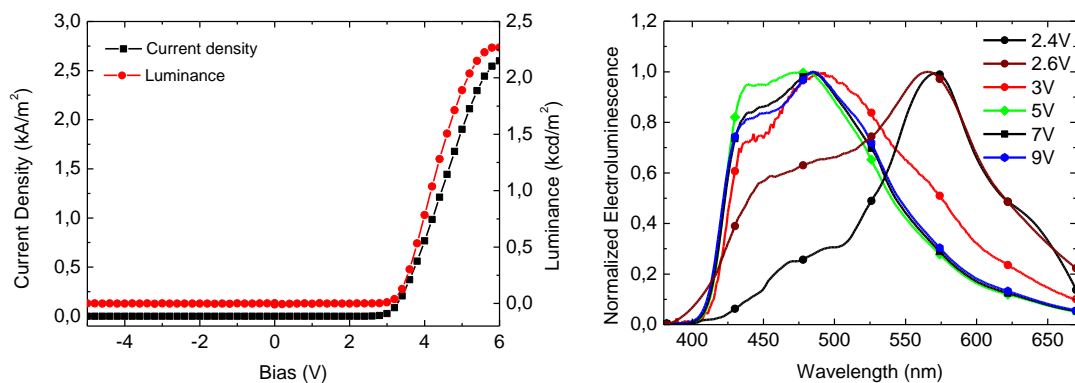


Figure 7.13: J-V-L characteristics and current density dependent EL spectra of device d

Origin of the vanishing red emission

In literature, the formation of isolated islands consisting of the chromophore were observed and identified as a cause for an incomplete exciton energy transfer¹⁶⁹. AFM height images of the topography of pure TFB and a TFB:PPDB (1 wt%) blend are depicted in Figure 7.14. Both images show that smooth and flat surfaces without pinholes or irregularities were formed. RMS roughness values were $R_q = 0.7$ nm for pure TFB and $R_q = 0.5$ nm for the blend. The slight variance in the RMS values is most likely traced back to local discrepancies. Therefore, the formation of isolated islands of PPDB was to be excluded.

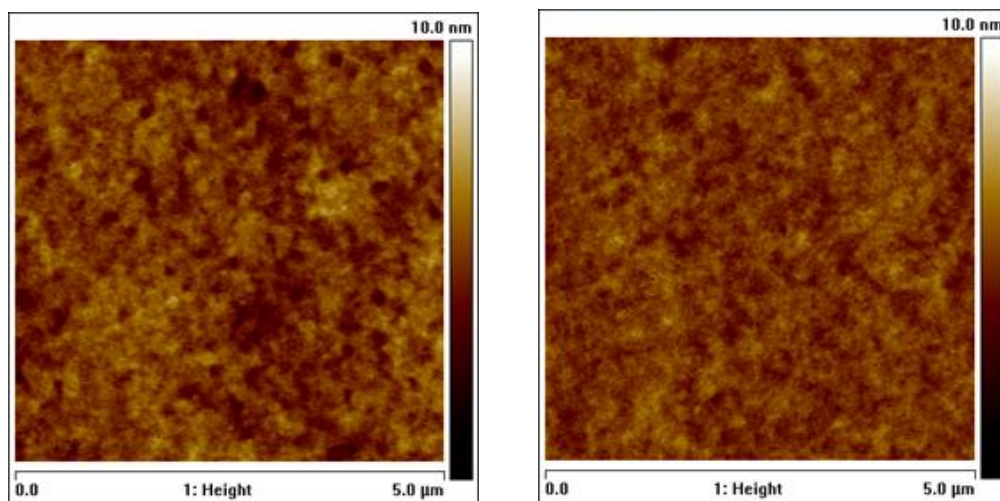


Figure 7.14: AFM height images of a 5 x 5 μm^2 area of TFB (left; $R_q = 0.7$ nm) and TFB:PPDB (1wt%) (right; $R_q = 0.5$ nm)

The impact of a possible saturation of red-emitting chromophores due to their typically low concentrations has been discussed in literature¹⁷³. However, Tasch et al.¹⁷⁰ observed almost no host emission for PPDB concentrations of about 1 wt%. As a consequence, dye saturation was less probable. Unfortunately, to date, several processes causing a saturation or even

quenching of the emission from a red-orange emitting guest were identified. Besides a shift of the recombination zone ¹⁷⁴, electric field dependent recombination on the acceptor dye was also identified ^{175,176}. To complicate matters further, the excitation mechanism of the dye, in this case PPDB, is still under debate. While it was argued that FRET is the major excitation mechanism for red dyes ¹⁷⁷, it was also reported that charge trapping is the major excitation process ^{175,176,178}. To elucidate the working mechanisms behind the disappearance of the red emission of **device d**, a rigorous and time consuming analysis would be required. Since such an analysis is beyond the scope of this work, a description of the necessary steps is given below instead.

To exclude a degradation of the dye as the source for the vanishing red emission, it is necessary to conduct a detailed screening including UV-Vis and PL measurements of the TFB:PPDB host-guest system and the performance of this blend should be assessed in an ITO/PEDOT:PSS/TFB:PPDB/Ca/Al structure as well. Furthermore, the J-V-L characteristics and voltage dependent EL spectra of different device configurations with varying layer thicknesses and varying PPDB concentrations need to be studied. Voltage dependent EL spectra provide valuable information about the contributions from the individual layers. Even though the so collected information is still not enough for an accurate determination of the location of the recombination zone, a correlation between the intensity of the red emission and the relative contribution from the two layers should be detectable. The J-V-L characteristics help in identifying charge trapping because the generated trapping sites adversely affect the current transport through the organic layer. While charge carrier trapping can be detected in this way, any contribution to the excitation process of the dye from FRET needs to be verified by time-dependent PL measurements which detect FRET by a reduction of the excited state lifetimes of the host.

Summary

This subchapter presented a device that combines the voltage dependent color tunable bilayer structure introduced in chapter 7.3 with PPDB, an orange emitting chromophore. Photophysical studies of PPDB revealed a PL emission peaking at 596 nm in thin film. Good spectral overlap between TFB and PPDB was observed. A device with an ITO/PEDOT:PSS/TFB:PPDB/PEGPF/Cs₂CO₃/Al configuration and 1 wt% of PPDB blended into the TFB layer was fabricated and J-V-L characteristics and voltage dependent EL spectra were recorded. The device exhibited a low turn-on voltage of 2.7 V and was able to attain a peak luminance of 2270 cd/m². Luminous efficiency achieved 1.06 cd/A. From the voltage dependent EL spectra, a color shift from orange at lower voltages to blue at higher voltages

was recognizable. However, the origin of this color shift is unknown and requires a more rigorous analysis.

Table 7.2: Device data for a bilayer device with a TFB and PPDB configuration

organic layer geometry	onset voltage ^a [V]	η^b [cd/A]	max. luminance [cd/m ²]	CIE1931 coordinates ^c x,y
d TFB(20nm):PPDB(1wt %)/PEGPF(60nm)/Cs ₂ CO ₃ (1,5A)/Al	2,7	1,06	2270	

^a voltage at a luminance of 1 cd/m²; ^b value of maximum efficiency; ^c at a current of 10 mA

7.4.2 Red-Blue Emitting PtOEP Blend Systems

In the last chapter, PPDB, an orange emitting dye (chapter 7.4), was incorporated into an ITO/PEDOT:PSS/TFB:PPDB/PEGPF/Cs₂CO₃/Al assembly. The capability to switch the emission color from orange to blue in dependence on the applied electric field was demonstrated. However, due to the tremendous experimental effort and the expected low efficiencies achievable by use of PPDB, the origin of this color switch was not investigated any further and as a consequence is still unknown. Better efficiencies are attainable by incorporating an organometallic dye, which allows triplet excitons to contribute to the emission (see chapter 2.3). For this reason, in analogy to chapter 7.4, it was attempted to achieve an OLED tunable between red and blue by incorporating a red emitting organometallic dye into the TFB layer of an ITO/PEDOT:PSS/TFB/PEGPF/Cs₂CO₃/Al bilayer assembly.

The organometallic porphine complex chosen incorporates the heavy metal Platinum (Pt) which allows the optical recombination of triplet excitons due to strong spin-orbit coupling. The compound Platinum(II) 2,3,7,8,12,13,17,18-octaethyl-21H,23H-porphyrin (PtOEP, Sigma Aldrich) was used as provided without any further purification. The chemical structure of PtOEP is depicted in Figure 7.15. PtOEP was among the first dyes employed in a phosphorescent OLEDs and was reported for the first time by Forrest et al.³³ as an acceptor in Tris(8-hydroxyquinolino)aluminum (Alq₃) with different concentrations. Singlet lifetime in PtOEP was determined to be at approximately 1 ps by transient absorption spectrometry³³.

Fluorescent efficiency, however, was found to be rather poor with efficiency values of $2 \times 10^{-5}\%$ ¹⁷⁹. It was observed that PtOEP has a radiative lifetime of about 300 μs for the triplet state^{33,180} which can lead to a saturation of PtOEP at lower concentrations as well as at higher current densities.

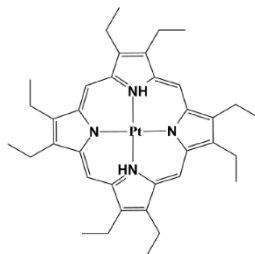


Figure 7.15: Chemical structure of Platinum(II)-Octaethylporphyrin

Photophysical characterization

UV-Vis and PL spectra for PtOEP and a PL spectrum for TFB are shown in Figure 7.16. The absorption of PtOEP showed two distinct absorption bands. The first absorption zone, stretching between 350 nm and 525 nm, had its maximum at 377 nm, with most of the absorption occurring between 350 nm and 430 nm. The second absorption zone was distinctly smaller, starting at 545 nm and ending at 585 nm and had its absorption maximum at 550 nm. PL emission was characterized by a sharp emission band that ranged from 610 nm to well beyond 650 nm, with a peak maximum at 650 nm. From Figure 7.16 it can be observed that the PtOEP absorption- and the TFB emission spectrum displayed only a small overlap. Because of that, an efficient FRET from the TFB host to the PtOEP guest was not to be expected.

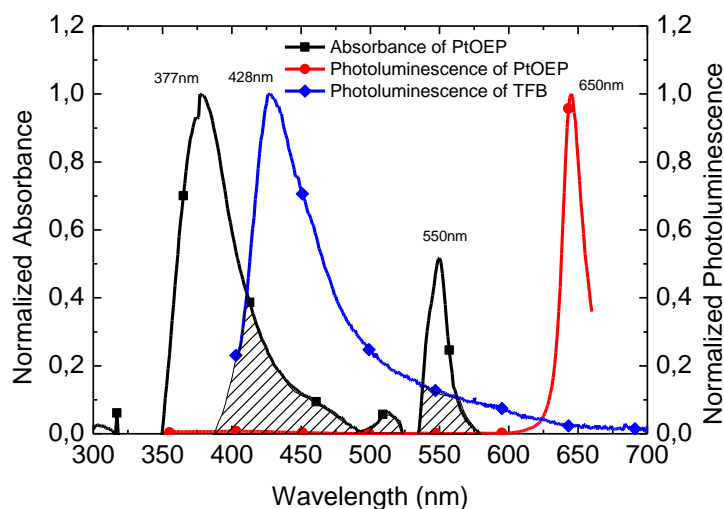


Figure 7.16: UV-Vis and PL spectra of PtOEP and PL spectrum of TFB. PL spectra of PtOEP were acquired embedded in PVK (courtesy of Stefan Sax)

Device characteristics

In this chapter, devices of an ITO/PEDOT:PSS/TFB:PtOEP/PEGPF/Cs₂CO₃/Al assembly are fabricated in order to verify if voltage dependent color tuning between red and blue is possible. The first device, **device e**, had a concentration of 1 wt% of PtOEP blended into the TFB layer. The layer thickness of the TFB:PtOEP and PEGPF layers was 34 nm and 60 nm, respectively.

J-V-L characteristics as well as voltage dependent EL spectra of **device e** were recorded and the results are depicted in Figure 7.17. Important electro-optical data is listed in Table 7.3. Turn on voltage was observed at 2.7 V and peak luminance was 1506 cd/m² at 7 V. Luminous efficiency attained a maximum value of 0.55 cd/A. Voltage dependent EL spectra revealed the presence of an emission peak at 650 nm at all voltages. Starting at 3.6 V, the emergence of an emission in the range of approximately 400 nm to 570 nm was detected. While the shape of the blue emission largely remained the same, a steady increase in intensity was observable at higher voltages with a persistent local peak at 438 nm. Furthermore, the formation of a feature at 483 nm was visible which additionally became more pronounced at higher voltages. The emergence of the aforementioned feature can be explained by a defect formation in PEGPF as observed in chapter 7.2. From the voltage dependent EL spectra it was apparent, that a voltage dependent shift from red at lower biases to pink-blue at higher biases was achieved (also demonstrated in CIE1931 diagram Table 7.3).

Contrary to the bilayer devices presented in chapter 7.3, the change of the emission color was not attributable to a change of the recombination zone. This was justified by the following argumentation. The absolute emission peak in the normalized EL spectra was at all recorded voltages located at 650 nm, which represented red emission originating from PtOEP. Assuming that a move of the recombination zone from the TFB:PtOEP layer into PEGPF occurred, a decline of the red emission and an increase of the emission resulting from PEGPF – identifiable as features or even peaks at around 470 nm – would be the result. However, this behavior was not observed. In case the recombination zone was moving from the PEGPF into the TFB:PtOEP layer, emission from PtOEP had to increase – in the normalized spectra detectable as a drop in the blue emission around 438 nm (ascribable to TFB). This was also not the case, but it could be argued that PtOEP became saturated³³ at higher current densities, causing the blue emission originating from TFB to increase. While the increase around 438 nm was indeed observed, it is known from chapter 7.3 that a move of the recombination zone changes the spectral composition of the blue emission, resulting in a decrease of the emission around 470 nm. Thus, such a movement of the recombination zone would have been identifiable as an emission peak in the vicinity of 470 nm (attributable to the majority of the emission stemming from PEGPF) at lower voltages which moves to 438 nm (assignable to TFB) at higher voltages. However, the emission maximum in the blue range of the spectrum

remained at 438 nm for all voltages. Additionally, with the exception of the identified defect formation of PEGPF, the shape of the emission from TFB and PEGPF did not change. Therefore, a movement of the recombination zone was excluded.

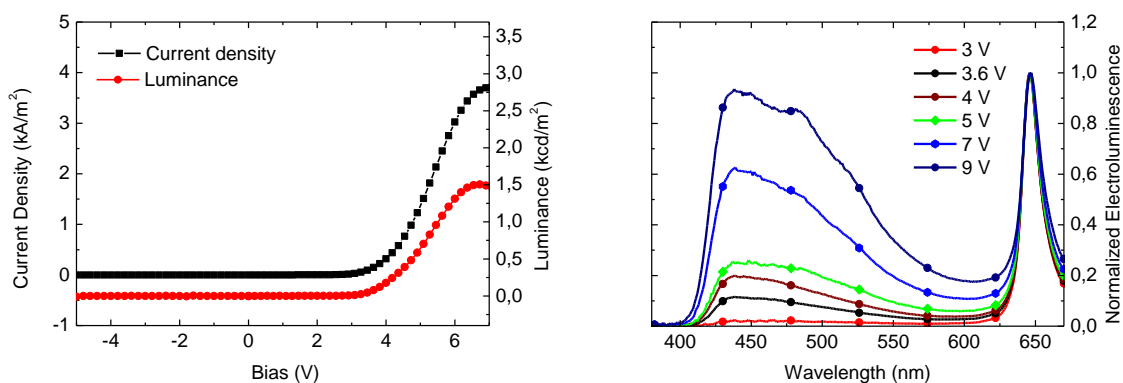


Figure 7.17: J-V-L characteristics and voltage-dependent EL spectra for device e

It is remarkable, that a strong red emission was present despite the fact that only an inefficient Förster- and Dexter type of energy transfer between TFB and PtOEP was to be expected. In literature it has been demonstrated that PtOEP can act as an efficient charge trap and recombination center^{45,181} when the HOMO level of PtOEP is above the level of the host or when the LUMO level of PtOEP is below the level of the host. It is however not important that both conditions are fulfilled. For example, if the HOMO level of PtOEP is above that of the host, holes will be efficiently trapped on PtOEP and form a cationic excited state of PtOEP. In this state, PtOEP then transforms to an electron trap. To estimate if either of the aforementioned conditions can exist in the TFB:PtOEP host-guest system, UPS data for PtOEP and TFB were taken from Cleave et al.¹⁸² and Trattnig et al.¹¹¹, respectively, and is depicted in Figure 7.18. From this illustration it can be seen that the HOMO levels of PtOEP and TFB aligned, while the LUMO level of PtOEP was about 0.7 eV below that of TFB. The energy difference was quite significant and, therefore, PtOEP probably acted as an efficient electron trap.

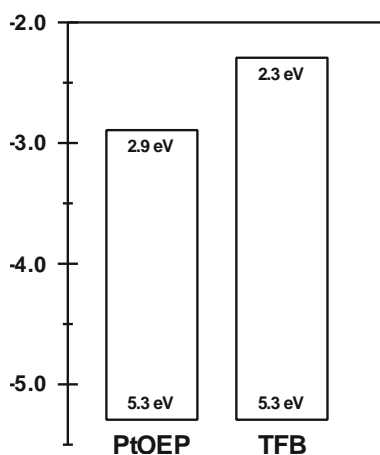


Figure 7.18: HOMO and LUMO levels for TFB and PtOEP (data for PtOEP and TFB taken from Ref¹⁸² and Ref¹¹¹)

Consequently, the observed color shift was explained by the fact that PtOEP, as a triplet emitter, featured dramatically longer lifetimes of the excited triplet state (about 300 μs ^{33,180}) than fluorescent emitters (in the range of several ps¹⁸³). The tremendously increased lifetimes then resulted in a saturation of PtOEP¹⁸¹, which prevented the negative charges to hop onto a PtOEP site. Therefore, the negative charges resided on TFB long enough to recombine with a hole there, instead of transferring to PtOEP. This explains the increasing emission originating from TFB. The absence of a distinctive feature at 470 nm ascribable to PEGPF at all voltages was probably caused by the fact, that the majority of the recombination zone was located in the TFB:PtOEP layer.

Summary

In this chapter PtOEP was investigated for the purpose to change the color-tunable range of the devices presented in chapter 7.3 from white-blue to red-blue. Therefore, basic photophysical characterization was performed and besides a favorable sharp red emission peaking at 650 nm, a poor spectral overlap between TFB and PtOEP was ascertained. Proof of principle was performed by blending PtOEP into the TFB layer of an ITO/PEDOT:PSS/TFB:PtOEP/PEGPF/Cs₂CO₃/Al device at a concentration of 1 wt%. Even though the EL emission color changed as a function of the applied bias from red at lower voltages to a blue-pink hue at higher voltages, the change of the recombination zones could be excluded as the cause. Instead, the shift of the emission color was attributed to a saturation of PtOEP at higher voltages. Finally, the origin of the strong red emission in the absence of an efficient Förster- and Dexter type energy transfer was attributed to charge trapping of electrons on PtOEP.

Table 7.3: Device data for bilayer devices consisting of different TFB and PtOEP configurations

organic layer geometry	onset voltage ^a [V]	η^b [cd/A]	max. luminance [cd/m ²]	CIE1931 coordinates ^c x,y
e TFB:PtOEP(1wt%) (34nm)/PEGPF(60 nm)/Cs ₂ CO ₃ /Al	2.5	0.55	1506	

^a voltage at a luminance of 1 cd/m²; ^b value of maximum efficiency; ^c at an applied bias of 4 V

7.5 Conclusion

In conclusion, a novel polyfluorene with PEG side chains, PEGPF, soluble in polar solvents was demonstrated in this chapter. Photophysical investigations confirmed that the addition of the PEG side chains did not impact the well-known deep blue emission behavior of PFO. A maximum PLQY of 74% was recorded in MeOH solution. Characterization in the device yielded a low onset voltage of 3.2 V, a maximum luminance of 55 cd/m² and luminous efficiencies of only 0.005 cd/A in an ITO/PEDOT:PSS/PEGPF/Ca/Al assembly. Imbalanced charge carrier injection was identified as the cause for the poor performance observed and as a result a device with an ITO/PEDOT:PSS/TFB/PEGPF/Ca/Al structure where TFB was added as a HTL was assembled. Onset voltage improved by 0.2 V, while luminance and luminous efficiencies experienced a 20-fold and 28.6-fold increase compared to the single layer assembly. While the previously identified charge carrier imbalance was confirmed as the cause for the poor performance, a current density dependent shift of the EL emission spectra was observed. The dependence on the current density of the EL spectra was pinned on the movement of the recombination zone from PEGPF into the TFB layer. Color shifts from white at lower voltages to blue at higher voltages were demonstrated. The suitability of the presented layer configuration for flexible multi-color tunable OLEDs was investigated by means of PPDB, a fluorescent orange emitter, and PtOEP, a phosphorescent red emitter. Both emitters were incorporated in the TFB layer of an ITO/PEDOT:PSS/TFB/PEGPF/Cs₂CO₃/Al structure. In both instances, a voltage-dependent color switch between orange to blue (PPDB) and red to pink-blue (PtOEP) was possible. The cause for the color shift could not be explained in the case of PPDB, while the color shift exhibited by the device incorporating PtOEP was successfully described by a saturation of PtOEP instead of a movement of the recombination zone. Even though the ITO/PEDOT:PSS/TFB/PEGPF/Cs₂CO₃/Al structure did not yield a universal voltage-dependent color tunable OLED stack, it appeared to be a promising starting point for further investigations into that matter.

8 Conclusion

The scope of this master thesis was the investigation of novel solution processable blue light-emitting materials. The assessment of the respective photophysical and electro-optical properties was performed by means of absorption and photoluminescence spectroscopy, atomic force microscopy as well as by electro-optical characterization in OLED assemblies.

At first (chapter 5), materials belonging to the class of dendrimers were presented. All investigated materials followed a core-shell-surface design principle with a highly efficient blue emitting pyrene core and different shell and surface configurations. The impact of different surface groups and shell structures on the photophysical properties of the compounds under investigation was assessed by detailed photophysical studies. In general, UV-Vis spectra unveiled an absorption behavior separable into two zones, where one zone was ascribed to the absorption of the pyrene core, while the other zone was associated with the incorporated surface moieties. All compounds demonstrated a PL emission assignable to pyrene in the range between 428 nm and 424 nm in solution and between 438 nm and 455 nm in thin film, indicating the presence of an efficient energy transfer from the redox active surface groups. Studies of the energy transfer mechanism revealed that a FRET was not the only possible transfer mechanism in these materials but also an energy transfer with a linear distance-efficiency relationship. Depending on the shielding and the deplanarization caused by the dendrons, high PLQYs of up to 77% upon excitation at the core were attained. PLQYs obtained by an excitation of the surface groups yielded up to 65% and a dependence of the PLQY on the distance and the surface moieties was detected. Investigations into the effects of an additional generation of polyphenylenes revealed that while better shielding, and therefore higher PLQY, can be provided, care has to be taken regarding an eventual increase in sterical stress. Representative for all investigated dendrimers, the suitability of one dendrimer for the application in OLEDs was studied in an ITO/PEDOT:PSS/PYTPAG1/Ca/Al single layer assembly. However, low luminous efficiencies and low luminance indicated further room for improvements. By the insertion of a HTL and an ETL as well as the improvement of the EIL and the HIL, luminous efficiencies increased 68-fold and luminance increased 19.7-fold, compared to the single layer structure, yielding a luminous efficiency as well as a maximum luminance of 0.41 cd/A and 2210 cd/m².

Chapter 6 covered the studies of a series of polyfluorenes with different perfluorinated side chain configurations soluble in fluorinated solvents. Photophysical characterization revealed that even though the investigated polymers featured dramatically different side chain configurations, they exhibited an emission behavior similar to a standard polyfluorene. While all polymers featured a similarly structured PL emission spectrum, a systematic blue shift of the absorption and emission maxima with the increase in sterical stress exerted by more

complex perfluorinated side chains was observed in solution and to a lesser extent even in thin film. PLQYs of up to 85 % were recorded and an increase of the PLQY with more demanding side chain configurations was attributed to the thereby increased shielding of the backbone of the polymer. In spite of the favorable results obtained by the photophysical investigations, the promising performance could not be replicated in single- and bilayer device designs. Maximum luminance values for the single- and bilayer devices amounted to 37 cd/m² and 315 cd/m², respectively. Likewise, luminous efficiencies remained low at only 0.035 cd/A for the single layer and 0.293 cd/A for the bilayer devices. In addition to the disappointing device performance, severe spectral instabilities were observed for all fabricated devices. These instabilities as well as the poor device performance were investigated by pulsed characterization that identified a charging of the perfluorinated side chains as the likely cause. To complement the investigations on these novel polymers, their suitability for an orthogonal solvent process for the assembly of multi-layer structures was investigated. However, the formation of smooth multilayer structures was only observed in conjunction with PEGPF.

Last but not least a novel polyfluorene with PEG side chains, PEGPF, soluble in polar solvents, was demonstrated chapter 7. Photophysical investigations confirmed the presence of the well-known deep blue emission behavior of PFO and revealed a PLQY of 74%. Electro-optical characterization in an ITO/PEDOT:PSS/PEGPF/Ca/Al single layer device yielded low luminance and luminous efficiency values. An imbalanced charge carrier injection was identified as the reason and was addressed in a device where a HTL was added in the following configuration ITO/PEDOT:PSS/TFB/PEGPF/Ca/Al. Onset voltage improved by 0.2 V, while luminance and luminous efficiencies experienced a 20-fold and 28.6-fold increase, respectively, compared to the single layer assembly. Furthermore, a current density dependent shift of the EL emission spectra caused by a movement of the recombination zone from PEGPF into the TFB layer was observed. As a consequence, emission color shifts from white at lower voltages to blue at higher voltages were demonstrated. The possibility to exploit the moveable recombination zone for red-blue and orange-blue color tunable OLEDs was investigated by incorporating PPDB, a fluorescent orange emitter, and PtOEP, a phosphorescent red emitter in the TFB layer of an ITO/PEDOT:PSS/TFB/PEGPF/Cs₂CO₃/Al structure. While color shifts were observed in both devices, the cause for it was only explained in case of the device incorporating PtOEP where the color shift was successfully described by a saturation of PtOEP instead of a movement of the recombination zone.

9 References

1. Tang, C. W. & VanSlyke, S. a.; "Organic electroluminescent diodes", *Appl. Phys. Lett.* **51**, 913 (1987), DOI:10.1063/1.98799
2. Burroughes, J. H., Bradley, D. D. C., Brown, A. R., Marks, R. N., Mackay, K., Friend, R. H., Burns, P. L. & Holmes, A. B.; "Light-emitting diodes based on conjugated polymers", *Nature* **347**, 539–541 (1990), DOI:10.1038/347539a0
3. Xiao, L., Chen, Z., Qu, B., Luo, J., Kong, S., Gong, Q. & Kido, J.; "Recent progresses on materials for electrophosphorescent organic light-emitting devices.", *Adv. Mater.* **23**, 926–52 (2011), DOI:10.1002/adma.201003128
4. Huang, T.; "Global AMOLED market analysis and forecast, 2011-2015", <http://www.digitimes.com/news/a20130702RS400.html>, (accessed October 24, 2013)
5. Mulliken, R. S.; "Spectroscopy, Molecular Orbitals, and Chemical Bonding", *Science (80-.)*. **157**, 13–24 (1967), DOI:10.1126/science.157.3784.13
6. Pauling, L.; "THE NATURE OF THE CHEMICAL BOND. APPLICATION OF RESULTS OBTAINED FROM THE QUANTUM MECHANICS AND FROM A THEORY OF PARAMAGNETIC SUSCEPTIBILITY TO THE STRUCTURE OF MOLECULES", *J. Am. Chem. Soc.* **53**, 1367–1400 (1931), DOI:10.1021/ja01355a027
7. Nau, S.; "Efficiency and Stability of Poly (indenofluorene) -based Homo- and Copolymers", Diploma thesis, Graz University of Technology, 2011
8. Fréchet, J. M. J.; "Functional Polymers and Dendrimers: Reactivity, Molecular Architecture, and Interfacial Energy", *Science (80-.)*. **263**, 1710–1715 (1994), DOI:10.2307/2883555
9. Tomalia, D. A., Baker, H., Dewald, J., Hall, M., Kallos, G., Martin, S., Roeck, J., Ryder, J. & Smith, P.; "A New Class of Polymers: Starburst-Dendritic Macromolecules", *Polym. J.* **17**, 117–132 (1985), DOI:10.1295/polymj.17.117
10. Leo, P. D. K.; "Bonding of sp²-hybridised carbon in benzene", <http://www.orgworld.de/>, (accessed October 16, 2013)
11. Heeger, A. J.; "Semiconducting and Metallic Polymers: The Fourth Generation of Polymeric Materials †", *J. Phys. Chem. B* **105**, 8475–8491 (2001), DOI:10.1021/jp011611w
12. Brédas, J., Thémans, B., Fripiat, J., André, J. & Chance, R.; "Highly conducting polyparaphenylene, polypyrrole, and polythiophene chains: An ab initio study of the geometry and electronic-structure modifications upon doping", *Phys. Rev. B* **29**, 6761–6773 (1984), DOI:10.1103/PhysRevB.29.6761
13. Michael H. M. Pienn; "Application of Blue-Emitting Ladder- Type Poly(para-phenylene)s for Solid State Lighting: Efficiency Improvement and Colour Tuning", Diploma thesis, Graz University of Technology, 2008

References

14. R. E. Peierls; "*More Surprises in Theoretical Physics*," Princeton University Press, Princeton, 1991
15. Chiang, C., Fincher, C., Park, Y., Heeger, A., Shirakawa, H., Louis, E., Gau, S. & MacDiarmid, A.; "Electrical Conductivity in Doped Polyacetylene", *Phys. Rev. Lett.* **39**, 1098–1101 (1977), DOI:10.1103/PhysRevLett.39.1098
16. Duan, L., Hou, L., Lee, T.-W., Qiao, J., Zhang, D., Dong, G., Wang, L. & Qiu, Y.; "Solution processable small molecules for organic light-emitting diodes", *J. Mater. Chem.* **20**, 6392 (2010), DOI:10.1039/b926348a
17. Aziz, H. & Popovic, Z. D.; "Degradation Phenomena in Small-Molecule Organic Light-Emitting Devices", *Chem. Mater.* **16**, 4522–4532 (2004), DOI:10.1021/cm040081o
18. Lo, S.-C. & Burn, P. L.; "Development of dendrimers: macromolecules for use in organic light-emitting diodes and solar cells.", *Chem. Rev.* **107**, 1097–1116 (2007), DOI:10.1021/cr050136l
19. Fréchet, J. M. J.; "Dendrimers and other dendritic macromolecules: From building blocks to functional assemblies in nanoscience and nanotechnology", *J. Polym. Sci. Part A Polym. Chem.* **41**, 3713–3725 (2003), DOI:10.1002/pola.10952
20. Wang, P.-W., Liu, Y., Devadoss, C., Bharathi, P. & Moore, J. S.; "Electroluminescent diodes from a single component emitting layer of dendritic macromolecules", *Adv. Mater.* **8**, 237–241 (1996), DOI:10.1002/adma.19960080311
21. Bernhardt, S., Kastler, M., Enkelmann, V., Baumgarten, M. & Müllen, K.; "Pyrene as chromophore and electrophore: encapsulation in a rigid polyphenylene shell.", *Chemistry* **12**, 6117–28 (2006), DOI:10.1002/chem.200500999
22. Wang, J.-L., Yan, J., Tang, Z.-M., Xiao, Q., Ma, Y. & Pei, J.; "Gradient shape-persistent pi-conjugated dendrimers for light-harvesting: synthesis, photophysical properties, and energy funneling.", *J. Am. Chem. Soc.* **130**, 9952–62 (2008), DOI:10.1021/ja803109r
23. Furuta, P. & Fréchet, J. M. J.; "Controlling solubility and modulating peripheral function in dendrimer encapsulated dyes.", *J. Am. Chem. Soc.* **125**, 13173–81 (2003), DOI:10.1021/ja037133f
24. Cornil, J., Beljonne, D., Calbert, J.-P. & Brédas, J.-L.; "Interchain Interactions in Organic π -Conjugated Materials: Impact on Electronic Structure, Optical Response, and Charge Transport", *Adv. Mater.* **13**, 1053–1067 (2001), DOI:10.1002/1521-4095(200107)13:14<1053::AID-ADMA1053>3.0.CO;2-7
25. Trattinig, R.; "Organic Light Emitting Devices based on Phosphorescent Organometallic Complexes in Blend- and Onchain Polymer Systems", Diploma thesis, Graz University of Technology, 2009
26. Franck, J. & Dymond, E. G.; "Elementary processes of photochemical reactions", *Trans. Faraday Soc.* **21**, 536 (1926), DOI:10.1039/tf9262100536
27. Condon, E.; "Nuclear Motions Associated with Electron Transitions in Diatomic Molecules", *Phys. Rev.* **32**, 858–872 (1928), DOI:10.1103/PhysRev.32.858

-
28. Henderson, B. & Imbusch, G. F.; "*Optical Spectroscopy of Inorganic Solids*," Oxford University Press, 1989
 29. Huang, K. & Rhys, A.; "Theory of Light Absorption and Non-Radiative Transitions in F-Centres", *Proc. R. Soc. A Math. Phys. Eng. Sci.* **204**, 406–423 (1950), DOI:10.1098/rspa.1950.0184
 30. Kasha, M.; "Characterization of electronic transition in complex molecules", *Discuss. Faraday Soc.* **9**, 14–19 (1950), DOI:10.1039/DF9500900014
 31. Stokes, G. G.; "On the Change of Refrangibility of Light", *Philos. Trans. R. Soc. London* **142**, 463–562 (1852), DOI:10.1098/rstl.1852.0022
 32. Heimel, G., Daghofer, M., Gierschner, J., List, E. J. W., Grimsdale, A. C., Müllen, K., Beljonne, D., Brédas, J.-L. & Zojer, E.; "Breakdown of the mirror image symmetry in the optical absorption/emission spectra of oligo(para-phenylene)s.", *J. Chem. Phys.* **122**, 54501 (2005), DOI:10.1063/1.1839574
 33. Baldo, M. A., O'brien, D., You, Y. & Forrest, S. R.; "Highly efficient phosphorescent emission from organic electroluminescent devices", *Nature* **395**, 151–154 (1998), DOI:10.1038/25954
 34. Lo, S., Shipley, C. P., Bera, R. N., Harding, R. E., Cowley, A. R., Burn, P. L. & Samuel, I. D. W.; "Blue Phosphorescence from Iridium(III) Complexes at Room Temperature", *Chem. Mater.* **18**, 5119–5129 (2006), DOI:10.1021/cm061173b
 35. Qin, T., Ding, J., Baumgarten, M., Wang, L. & Müllen, K.; "Red-emitting dendritic iridium(III) complexes for solution processable phosphorescent organic light-emitting diodes.", *Macromol. Rapid Commun.* **33**, 1036–41 (2012), DOI:10.1002/marc.201100657
 36. Neuhold, A.; "Polymer Heterostructure Based Light Emitting Devices and Light Emitting Organic Sensors", Diploma thesis, Graz University of Technology, 2009
 37. Lakowicz, J. R.; "*Principles of Fluorescence Spectroscopy*," 3rd edition; Springer, New York, 2006
 38. Wilson, J. S., Dhoot, a S., Seeley, a J., Khan, M. S., Köhler, A. & Friend, R. H.; "Spin-dependent exciton formation in pi-conjugated compounds.", *Nature* **413**, 828–31 (2001), DOI:10.1038/35101565
 39. Reufer, M., Walter, M. J., Lagoudakis, P. G., Hummel, A. B., Kolb, J. S., Roskos, H. G., Scherf, U. & Lupton, J. M.; "Spin-conserving carrier recombination in conjugated polymers.", *Nat. Mater.* **4**, 340–6 (2005), DOI:10.1038/nmat1354
 40. Sirringhaus, H. *et al.*; "Two-dimensional charge transport in self-organized, high-mobility conjugated polymers", *Nature* **401**, 685–688 (1999), DOI:10.1038/44359
 41. Marcus, R. a.; "On the Theory of Electron-Transfer Reactions. VI. Unified Treatment for Homogeneous and Electrode Reactions", *J. Chem. Phys.* **43**, 679 (1965), DOI:10.1063/1.1696792
-

-
42. Förster, T.; "Zwischenmolekulare Energiewanderung und Fluoreszenz", *Ann. Phys.* **437**, 55–75 (1948), DOI:10.1002/andp.19484370105
 43. Damien, M.; "FRET distance", <http://commons.wikimedia.org/wiki/File:FRET-Abstand.png>, (accessed October 19, 2013)
 44. Dexter, D. L.; "A Theory of Sensitized Luminescence in Solids", *J. Chem. Phys.* **21**, 836 (1953), DOI:10.1063/1.1699044
 45. Lane, P., Pallis, L., O'Brien, D., Giebeler, C., Cadby, A., Lidzey, D., Campbell, A., Blau, W. & Bradley, D.; "Origin of electrophosphorescence from a doped polymer light emitting diode", *Phys. Rev. B* **63**, 235206 (2001), DOI:10.1103/PhysRevB.63.235206
 46. Trattng, R.; "Solution Processed Organic Multilayer Devices for Light Emitting and Photovoltaic Applications", Dissertation, Graz University of Technology, 2013
 47. Mott, N. F.; "The Theory of Crystal Rectifiers", *Proc. R. Soc. A Math. Phys. Eng. Sci.* **171**, 27–38 (1939), DOI:10.1098/rspa.1939.0051
 48. Schottky, W.; "Abweichung vom Ohmschen Gesetz in Halbleitern", *Phys. Zeitschrift* **41**, 570–573 (1940),
 49. Koch, N.; "Electronic structure of interfaces with conjugated organic materials", *Phys. status solidi - Rapid Res. Lett.* **6**, 277–293 (2012), DOI:10.1002/pssr.201206208
 50. Ishii, H., Sugiyama, K., Ito, E. & Seki, K.; "Energy Level Alignment and Interfacial Electronic Structures at Organic/Metal and Organic/Organic Interfaces", *Adv. Mater.* **11**, 605–625 (1999), DOI:10.1002/(SICI)1521-4095(199906)11:8<605::AID-ADMA605>3.0.CO;2-Q
 51. Tengstedt, C., Osikowicz, W., Salaneck, W. R., Parker, I. D., Hsu, C.-H. & Fahlman, M.; "Fermi-level pinning at conjugated polymer interfaces", *Appl. Phys. Lett.* **88**, 053502 (2006), DOI:10.1063/1.2168515
 52. Flämmich, M.; "Optical Characterization of OLED Emitter Properties by Radiation Pattern Analyses", Dissertation, Friedrich-Schiller-Universität Jena, 2011
 53. Nowy, S., Krummacher, B. C., Frischeisen, J., Reinke, N. A. & Brütting, W.; "Light extraction and optical loss mechanisms in organic light-emitting diodes: Influence of the emitter quantum efficiency", *J. Appl. Phys.* **104**, 123109 (2008), DOI:10.1063/1.3043800
 54. Meerheim, R., Furno, M., Hofmann, S., Lüssem, B. & Leo, K.; "Quantification of energy loss mechanisms in organic light-emitting diodes", *Appl. Phys. Lett.* **97**, 253305 (2010), DOI:10.1063/1.3527936
 55. Purcell, E. M., Pound, R. V.; "Theory of Magnetic Resonance Absorption by Nuclear Moments in Solids.", *Proc. Am. Phys. Soc.* **69**, 680 (1946), DOI:10.1103/PhysRev.69.674.2
 56. Hofmann, S., Thomschke, M., Lüssem, B. & Leo, K.; "Top-emitting organic light-emitting diodes.", *Opt. Express* **19**, A1250–64 (2011), DOI:10.1364/OE.19.0A1250
-

-
57. Crosby, G. A. & Demas, J. N.; "Measurement of photoluminescence quantum yields. Review", *J. Phys. Chem.* **75**, 991–1024 (1971), DOI:10.1021/j100678a001
 58. Parker, C. a. & Rees, W. T.; "Correction of fluorescence spectra and measurement of fluorescence quantum efficiency", *Analyst* **85**, 587 (1960), DOI:10.1039/an9608500587
 59. Melhuish, W. H.; "QUANTUM EFFICIENCIES OF FLUORESCENCE OF ORGANIC SUBSTANCES: EFFECT OF SOLVENT AND CONCENTRATION OF THE FLUORESCENT SOLUTE", *J. Phys. Chem.* **65**, 229–235 (1961), DOI:10.1021/j100820a009
 60. Schuh, S.; "Application of Blue-Light-Emitting Polyfluorene Derivatives in Solution processed Multi Layer Devices fabricated from Orthogonal Solvents", Diploma thesis, Graz University of Technology, 2012
 61. Liu, D. *et al.*; "Fluorescence and Intramolecular Energy Transfer in Polyphenylene Dendrimers", *Macromolecules* **36**, 5918–5925 (2003), DOI:10.1021/ma0344801
 62. Langenegger, S. M. & Häner, R.; "Excimer formation by interstrand stacked pyrenes.", *Chem. Commun. (Camb)*. 2792–3 (2004), DOI:10.1039/b412831a
 63. Qin, T., Zhou, G., Scheiber, H., Bauer, R. E., Baumgarten, M., Anson, C. E., List, E. J. W. & Müllen, K.; "Polytriphenylene dendrimers: a unique design for blue-light-emitting materials.", *Angew. Chem. Int. Ed. Engl.* **47**, 8292–6 (2008), DOI:10.1002/anie.200802854
 64. Dawson, W. R. & Windsor, M. W.; "Fluorescence yields of aromatic compounds", *J. Phys. Chem.* **72**, 3251–3260 (1968), DOI:10.1021/j100855a027
 65. Qin, T. *et al.*; "Core, shell, and surface-optimized dendrimers for blue light-emitting diodes.", *J. Am. Chem. Soc.* **133**, 1301–3 (2011), DOI:10.1021/ja109734e
 66. Ego, C., Grimsdale, A. C., Uckert, F., Yu, G., Srdanov, G. & Müllen, K.; "Triphenylamine-Substituted Polyfluorene—A Stable Blue-Emitter with Improved Charge Injection for Light-Emitting Diodes", *Adv. Mater.* **14**, 809 (2002), DOI:10.1002/1521-4095(20020605)14:11<809::AID-ADMA809>3.0.CO;2-8
 67. Bellmann, E., Shaheen, S. E., Thayumanavan, S., Barlow, S., Grubbs, R. H., Marder, S. R., Kippelen, B. & Peyghambarian, N.; "New Triarylamine-Containing Polymers as Hole Transport Materials in Organic Light-Emitting Diodes: Effect of Polymer Structure and Cross-Linking on Device Characteristics", *Chem. Mater.* **10**, 1668–1676 (1998), DOI:10.1021/cm980030p
 68. Choulis, S. a. A., Choong, V.-E., Patwardhan, A., Mathai, M. K. K. & So, F.; "Interface Modification to Improve Hole-Injection Properties in Organic Electronic Devices", *Adv. Funct. Mater.* **16**, 1075–1080 (2006), DOI:10.1002/adfm.200500443
 69. Huang, F., Cheng, Y.-J., Zhang, Y., Liu, M. S. & Jen, A. K.-Y.; "Crosslinkable hole-transporting materials for solution processed polymer light-emitting diodes", *J. Mater. Chem.* **18**, 4495 (2008), DOI:10.1039/b804977g
-

-
70. Sun, Q., Subramanyam, G., Dai, L., Check, M., Campbell, A., Naik, R., Grote, J. & Wang, Y.; "Highly efficient quantum-dot light-emitting diodes with DNA-CTMA as a combined hole-transporting and electron-blocking layer.", *ACS Nano* **3**, 737–43 (2009), DOI:10.1021/nn8009079
71. Fong, H. H., Lun, K. C. & So, S. K.; "Hole transports in molecularly doped triphenylamine derivative", *Chem. Phys. Lett.* **353**, 407–413 (2002), DOI:10.1016/S0009-2614(02)00053-2
72. Schwab, M. G. *et al.*; "Molecular triangles: synthesis, self-assembly, and blue emission of cyclo-7,10-tris-triphenylenyl macrocycles.", *Chem. Asian J.* **6**, 3001–10 (2011), DOI:10.1002/asia.201100258
73. Chung, S.-J., Kwon, K., Lee, S., Jin, J.-I., Lee, C. H., Lee, C. E. & Park, Y.; "Highly Efficient Light-Emitting Diodes Based on an Organic-Soluble Poly(p-phenylenevinylene) Derivative Carrying the Electron-Transporting PBD Moiety", *Adv. Mater.* **10**, 1112–1116 (1998), DOI:10.1002/(SICI)1521-4095(199810)10:14<1112::AID-ADMA1112>3.0.CO;2-P
74. Zhang, P., Xia, B., Zhang, Q., Yang, B., Li, M., Zhang, G. & Tian, W.; "New 1,3,4-oxadiazole containing materials with the effective leading substituents: The electrochemical properties, optical absorptions, and the electronic structures", *Synth. Met.* **156**, 705–713 (2006), DOI:10.1016/j.synthmet.2006.03.011
75. Kulkarni, A. P., Tonzola, C. J., Babel, A. & Jenekhe, S. a.; "Electron Transport Materials for Organic Light-Emitting Diodes", *Chem. Mater.* **16**, 4556–4573 (2004), DOI:10.1021/cm049473l
76. Liu, Z.-Y., Tseng, S.-R., Chao, Y.-C., Chen, C.-Y., Meng, H.-F., Horng, S.-F., Wu, Y.-H. & Chen, S.-H.; "Solution-processed small molecular electron transport layer for multilayer polymer light-emitting diodes", *Synth. Met.* **161**, 426–430 (2011), DOI:10.1016/j.synthmet.2010.12.021
77. Tamoto, N., Adachi, C. & Nagai, K.; "Electroluminescence of 1,3,4-Oxadiazole and Triphenylamine-Containing Molecules as an Emitter in Organic Multilayer Light Emitting Diodes", *Chem. Mater.* **9**, 1077–1085 (1997), DOI:10.1021/cm960391+
78. Schrögel, P., Tomkevičienė, A., Strohriegl, P., Hoffmann, S. T., Köhler, A. & Lennartz, C.; "A series of CBP-derivatives as host materials for blue phosphorescent organic light-emitting diodes", *J. Mater. Chem.* **21**, 2266 (2011), DOI:10.1039/c0jm03321a
79. Grigalevicius, S., Ma, L., Xie, Z. & Scherf, U.; "Synthesis and characterization of new carbazole/fluorene-based derivatives for blue-light-emitting devices", *J. Polym. Sci. Part A Polym. Chem.* **44**, 5987–5994 (2006), DOI:10.1002/pola.21660
80. Yang, W., Chen, Y., Jiang, W., Ban, X., Huang, B., Dai, Y. & Sun, Y.; "A carbazole-based dendritic host material for efficient solution-processed blue phosphorescent OLEDs", *Dye. Pigment.* **97**, 286–290 (2013), DOI:10.1016/j.dyepig.2012.12.030
81. Brütting, W., Berleb, S. & Mückl, A. G.; "Device physics of organic light-emitting diodes based on molecular materials", *Org. Electron.* **2**, 1–36 (2001), DOI:10.1016/S1566-1199(01)00009-X
-

-
82. Köhler, a. & Bäessler, H.; "Triplet states in organic semiconductors", *Mater. Sci. Eng. R Reports* **66**, 71–109 (2009), DOI:10.1016/j.mser.2009.09.001
83. Pfeiffer, M., Leo, K., Zhou, X., Huang, J. ., Hofmann, M., Werner, A. & Blochwitz-Nimoth, J.; "Doped organic semiconductors: Physics and application in light emitting diodes", *Org. Electron.* **4**, 89–103 (2003), DOI:10.1016/j.orgel.2003.08.004
84. Kwong, R. C., Lamansky, S. & Thompson, M. E.; "Organic Light-emitting Devices Based on Phosphorescent Hosts and Dyes", *Adv. Mater.* **12**, 1134–1138 (2000), DOI:10.1002/1521-4095(200008)12:15<1134::AID-ADMA1134>3.0.CO;2-1
85. Koch, N., Kahn, a., Ghijsen, J., Pireaux, J.-J., Schwartz, J., Johnson, R. L. & Elschner, a.; "Conjugated organic molecules on metal versus polymer electrodes: Demonstration of a key energy level alignment mechanism", *Appl. Phys. Lett.* **82**, 70 (2003), DOI:10.1063/1.1532102
86. Park, Y. H., Rho, H. H., Park, N. G. & Kim, Y. S.; "Theoretical investigation of tetra-substituted pyrenes for organic light emitting diodes", *Curr. Appl. Phys.* **6**, 691–694 (2006), DOI:10.1016/j.cap.2005.04.021
87. Kim, H. M., Lee, Y. O., Lim, C. S., Kim, J. S. & Cho, B. R.; "Two-photon absorption properties of alkynyl-conjugated pyrene derivatives.", *J. Org. Chem.* **73**, 5127–30 (2008), DOI:10.1021/jo800363v
88. Setayesh, S., Grimsdale, A. C., Weil, T., Enkelmann, V., Müllen, K., Meghdadi, F., List, E. J. W. & Leising, G.; "Polyfluorenes with Polyphenylene Dendron Side Chains: Toward Non-Aggregating, Light-Emitting Polymers", *J. Am. Chem. Soc.* **123**, 946–953 (2001), DOI:10.1021/ja0031220
89. Akcelrud, L.; "Electroluminescent polymers", *Prog. Polym. Sci.* **28**, 875–962 (2003), DOI:10.1016/S0079-6700(02)00140-5
90. Murphy, L., Brulatti, P., Fattori, V., Cocchi, M. & Williams, J. a G.; "Blue-shifting the monomer and excimer phosphorescence of tridentate cyclometallated platinum(II) complexes for optimal white-light OLEDs.", *Chem. Commun. (Camb)*. **48**, 5817–9 (2012), DOI:10.1039/c2cc31330h
91. Massuyeau, F., Faulques, E., Lefrant, S., Majdoub, M., Ghedira, M., Alimi, K. & Wéry, J.; "Photoluminescence properties of new PPV derivatives", *J. Lumin.* **131**, 1541–1544 (2011), DOI:10.1016/j.jlumin.2011.02.010
92. Jordens, S., De Belder, G., Lor, M., Schweitzer, G., Van der Auweraer, M., Weil, T., Reuther, E., Müllen, K. & De Schryver, F. C.; "Energy transfer within perylene-terrylene dendrimers evidenced by polychromatic transient absorption measurements This paper is dedicated to Professor Jean Kossanyi on the occasion of his 70th birthday.", *Photochem. Photobiol. Sci.* **2**, 177 (2003), DOI:10.1039/b210261g
93. Astruc, D., Boisselier, E. & Ornelas, C.; "Dendrimers designed for functions: from physical, photophysical, and supramolecular properties to applications in sensing, catalysis, molecular electronics, photonics, and nanomedicine.", *Chem. Rev.* **110**, 1857–959 (2010), DOI:10.1021/cr900327d
-

-
94. Duhamel, J.; "Internal Dynamics of Dendritic Molecules Probed by Pyrene Excimer Formation", *Polymers (Basel)*. **4**, 211–239 (2012), DOI:10.3390/polym4010211
 95. De Schryver, F. C., Vosch, T., Cotlet, M., Van der Auweraer, M., Müllen, K. & Hofkens, J.; "Energy dissipation in multichromophoric single dendrimers.", *Acc. Chem. Res.* **38**, 514–22 (2005), DOI:10.1021/ar040126r
 96. Bansal, a. K. & Penzkofer, a.; "Linear and nonlinear optical spectroscopic characterisation of triphenylamine and 1,2,3-tris(3-methylphenylphenylamino)benzene", *Chem. Phys.* **352**, 48–56 (2008), DOI:10.1016/j.chemphys.2008.05.006
 97. Maus, M. *et al.*; "Intramolecular Energy Hopping and Energy Trapping in Polyphenylene Dendrimers with Multiple Peryleneimide Donor Chromophores and a Terryleneimide Acceptor Trap Chromophore", *J. Am. Chem. Soc.* **123**, 7668–7676 (2001), DOI:10.1021/ja010570e
 98. Wiesenhofer, H., Beljonne, D., Scholes, G. D., Hennebicq, E., Brédas, J.-L. & Zojer, E.; "Limitations of the Förster Description of Singlet Exciton Migration: The Illustrative Example of Energy Transfer to Ketonic Defects in Ladder-type Poly(para-phenylenes)", *Adv. Funct. Mater.* **15**, 155–160 (2005), DOI:10.1002/adfm.200400108
 99. Friend, R. H. *et al.*; "Electroluminescence in conjugated polymers", *Nature* **397**, 121–128 (1999), DOI:10.1038/16393
 100. List, E. J. W., Kim, C. H., Graupner, W., Leising, G. & Shinar, J.; "Singlet exciton quenching by polarons in π -conjugated wide bandgap semiconductors: a combined optical and charge transport study", *Mater. Sci. Eng. B* **85**, 218–223 (2001), DOI:10.1016/S0921-5107(01)00588-8
 101. List, E., Scherf, U., Müllen, K., Graupner, W., Kim, C.-H. & Shinar, J.; "Direct evidence for singlet-triplet exciton annihilation in π -conjugated polymers", *Phys. Rev. B* **66**, 235203 (2002), DOI:10.1103/PhysRevB.66.235203
 102. Schmidbauer, S., Hohenleutner, A. & König, B.; "Chemical degradation in organic light-emitting devices: mechanisms and implications for the design of new materials.", *Adv. Mater.* **25**, 2114–29 (2013), DOI:10.1002/adma.201205022
 103. Yakimov, a. ., Savvate'ev, V. . & Davidov, D.; "The role of traps in polymer-based light-emitting devices", *Synth. Met.* **115**, 51–56 (2000), DOI:10.1016/S0379-6779(00)00300-3
 104. Brütting, W., Riel, H., Beierlein, T. & Riess, W.; "Influence of trapped and interfacial charges in organic multilayer light-emitting devices", *J. Appl. Phys.* **89**, 1704 (2001), DOI:10.1063/1.1332088
 105. Traub, M. C., Vogelsang, J., Plunkett, K. N., Nuckolls, C., Barbara, P. F. & Vanden Bout, D. a; "Unmasking bulk exciton traps and interchain electronic interactions with single conjugated polymer aggregates.", *ACS Nano* **6**, 523–9 (2012), DOI:10.1021/nn203860u
 106. Groenendaal, L., Jonas, F., Freitag, D., Pielartzik, H. & Reynolds, J. R.; "Poly(3,4-ethylenedioxythiophene) and Its Derivatives: Past, Present, and Future", *Adv. Mater.*
-

-
- 12**, 481–494 (2000), DOI:10.1002/(SICI)1521-4095(200004)12:7<481::AID-ADMA481>3.0.CO;2-C
107. Heraeus Clevios GmbH; "Clevios™ P VP AL 4083", http://www.heraeus-clevios.com/media/webmedia_local/media/datenblaetter/81075812_CLEVIOS_P_VP_AI_4083__20101222.pdf, (accessed September 06, 2013)
108. Sigma-Aldrich; "TECHNICAL BULLETIN Plexcore OC RG-1100 and OC RG-1200", <http://www.sigmaaldrich.com/content/dam/sigma-aldrich/docs/Aldrich/Bulletin/699799bul.pdf>, (accessed September 06, 2013)
109. Heraeus Clevios GmbH; "Clevios™ PH 1000", http://www.heraeus-clevios.com/media/webmedia_local/media/datenblaetter/81076210_Clevios_PH_1000__20101222.pdf, (accessed September 06, 2013)
110. Redecker, M., Bradley, D. D. C., Inbasekaran, M., Wu, W. W. & Woo, E. P.; "High Mobility Hole Transport Fluorene-Triarylamine Copolymers", *Adv. Mater.* **11**, 241–246 (1999), DOI:10.1002/(SICI)1521-4095(199903)11:3<241::AID-ADMA241>3.0.CO;2-J
111. Trattinig, R. *et al.*; "Bright Blue Solution Processed Triple-Layer Polymer Light-Emitting Diodes Realized by Thermal Layer Stabilization and Orthogonal Solvents", *Adv. Funct. Mater.* **23**, 4897–4905 (2013), DOI:10.1002/adfm.201300360
112. Hwang, S.-H., Moorefield, C. N. & Newkome, G. R.; "Dendritic macromolecules for organic light-emitting diodes.", *Chem. Soc. Rev.* **37**, 2543–57 (2008), DOI:10.1039/b803932c
113. Figueira-Duarte, T. M. & Müllen, K.; "Pyrene-based materials for organic electronics.", *Chem. Rev.* **111**, 7260–314 (2011), DOI:10.1021/cr100428a
114. Su, H.-J., Wu, F.-I., Tseng, Y.-H. & Shu, C.-F.; "Color Tuning of a Light-Emitting Polymer: Polyfluorene-Containing Pendant Amino-Substituted Distyrylarylene Units", *Adv. Funct. Mater.* **15**, 1209–1216 (2005), DOI:10.1002/adfm.200400269
115. Yang, J. S., Choo, D. C., Kim, T. W., Jin, Y. Y., Seo, J. H. & Kim, Y. K.; "Electron injection mechanisms of green organic light-emitting devices fabricated utilizing a double electron injection layer consisting of cesium carbonate and fullerene", *Thin Solid Films* **518**, 6149–6152 (2010), DOI:10.1016/j.tsf.2010.04.061
116. Hung, L. S., Zhang, R. Q., He, P. & Mason, G.; "Contact formation of LiF/Al cathodes in Alq-based organic light-emitting diodes", *J. Phys. D. Appl. Phys.* **35**, 103–107 (2002), DOI:10.1088/0022-3727/35/2/302
117. Heil, H., Steiger, J., Karg, S., Gastel, M., Ortner, H., von Seggern, H. & Stößel, M.; "Mechanisms of injection enhancement in organic light-emitting diodes through an Al/LiF electrode", *J. Appl. Phys.* **89**, 420 (2001), DOI:10.1063/1.1331651
118. He, P., Wang, S. D., Lee, S. T. & Hung, L. S.; "Vibrational study of tris-(8-hydroxyquinoline) aluminum/LiF/Al interfaces", *Appl. Phys. Lett.* **82**, 3218 (2003), DOI:10.1063/1.1573353
-

-
119. Jabbour, G. E., Kippelen, B., Armstrong, N. R. & Peyghambarian, N.; "Aluminum based cathode structure for enhanced electron injection in electroluminescent organic devices", *Appl. Phys. Lett.* **73**, 1185 (1998), DOI:10.1063/1.122367
 120. Lee, J., Park, Y., Lee, S. K., Cho, E.-J., Kim, D. Y., Chu, H. Y., Lee, H., Do, L.-M. & Zyung, T.; "Tris-(8-hydroxyquinoline)aluminum-based organic light-emitting devices with Al/CaF₂ cathode: Performance enhancement and interface electronic structures", *Appl. Phys. Lett.* **80**, 3123 (2002), DOI:10.1063/1.1474602
 121. Lee, C. H.; "Enhanced efficiency and durability of organic electroluminescent devices by inserting a thin insulating layer at the Alq₃/cathode interface", *Synth. Met.* **91**, 125–127 (1997), DOI:10.1016/S0379-6779(98)80071-4
 122. Kang, S. J., Park, D. S., Kim, S. Y., Whang, C. N., Jeong, K. & Im, S.; "Enhancing the electroluminescent properties of organic light-emitting devices using a thin NaCl layer", *Appl. Phys. Lett.* **81**, 2581 (2002), DOI:10.1063/1.1511817
 123. Yi, Y., Kang, S. J., Cho, K., Koo, J. M., Han, K., Park, K., Noh, M., Whang, C. N. & Jeong, K.; "Origin of the improved luminance-voltage characteristics and stability in organic light-emitting device using CsCl electron injection layer", *Appl. Phys. Lett.* **86**, 213502 (2005), DOI:10.1063/1.1935773
 124. Huang, J., Xu, Z. & Yang, Y.; "Low-Work-Function Surface Formed by Solution-Processed and Thermally Deposited Nanoscale Layers of Cesium Carbonate", *Adv. Funct. Mater.* **17**, 1966–1973 (2007), DOI:10.1002/adfm.200700051
 125. Briere, T. R. & Sommer, a. H.; "Low-work-function surfaces produced by cesium carbonate decomposition", *J. Appl. Phys.* **48**, 3547 (1977), DOI:10.1063/1.324152
 126. Li, Y., Zhang, D.-Q., Duan, L., Zhang, R., Wang, L.-D. & Qiu, Y.; "Elucidation of the electron injection mechanism of evaporated cesium carbonate cathode interlayer for organic light-emitting diodes", *Appl. Phys. Lett.* **90**, 012119 (2007), DOI:10.1063/1.2429920
 127. Chen, F.-C., Wu, J.-L., Yang, S. S., Hsieh, K.-H. & Chen, W.-C.; "Cesium carbonate as a functional interlayer for polymer photovoltaic devices", *J. Appl. Phys.* **103**, 103721 (2008), DOI:10.1063/1.2937202
 128. Hong, J.-W., Kim, C.-H., Han, H.-S., Kang, Y.-G., Lee, J.-Y. & Kim, T.-W.; "Dependence of the efficiency improvement of organic light-emitting diodes on the thickness of the Cs₂CO₃ electron-injection layer", *J. Korean Phys. Soc.* **60**, 1611–1615 (2012), DOI:10.3938/jkps.60.1611
 129. Wu, C.-I. C.-C., Lin, C.-T., Chen, Y.-H., Chen, M.-H. & Lu, Y.-J.; "Electronic structures and electron-injection mechanisms of cesium-carbonate-incorporated cathode structures for organic light-emitting devices", *Appl. Phys. Lett.* **88**, 152104 (2006), DOI:10.1063/1.2192982
 130. Sung, H.-H. & Lin, H.-C.; "Novel Alternating Fluorene-Based Conjugated Polymers Containing Oxadiazole Pendants with Various Terminal Groups", *Macromolecules* **37**, 7945–7954 (2004), DOI:10.1021/ma0489927
-

-
131. Chen, S., Wu, Q., Kong, M., Zhao, X., Yu, Z., Jia, P. & Huang, W.; "On the origin of the shift in color in white organic light-emitting diodes", *J. Mater. Chem. C* **1**, 3508 (2013), DOI:10.1039/c3tc00766a
132. Huang, C. C., Meng, H. F., Ho, G. K., Chen, C. H., Hsu, C. S., Huang, J. H., Horng, S. F., Chen, B. X. & Chen, L. C.; "Color-tunable multilayer light-emitting diodes based on conjugated polymers", *Appl. Phys. Lett.* **84**, 1195 (2004), DOI:10.1063/1.1645983
133. Nau, S., Schulte, N., Winkler, S., Frisch, J., Vollmer, A., Koch, N., Sax, S. & List, E. J. W.; "Highly Efficient Color-Stable Deep-Blue Multilayer PLEDs: Preventing PEDOT:PSS-Induced Interface Degradation.", *Adv. Mater.* **25**, 4420–4 (2013), DOI:10.1002/adma.201300832
134. Malliaras, G. G. & Scott, J. C.; "The roles of injection and mobility in organic light emitting diodes", *J. Appl. Phys.* **83**, 5399 (1998), DOI:10.1063/1.367369
135. Zuniga, C. a., Barlow, S. & Marder, S. R.; "Approaches to Solution-Processed Multilayer Organic Light-Emitting Diodes Based on Cross-Linking †", *Chem. Mater.* **23**, 658–681 (2011), DOI:10.1021/cm102401k
136. Niu, Y.-H., Liu, M. S., Ka, J.-W., Bardeker, J., Zin, M. T., Schofield, R., Chi, Y. & Jen, a. K.-Y.; "Crosslinkable Hole-Transport Layer on Conducting Polymer for High-Efficiency White Polymer Light-Emitting Diodes", *Adv. Mater.* **19**, 300–304 (2007), DOI:10.1002/adma.200502769
137. Huang, F., Wu, H. & Cao, Y.; "Water/alcohol soluble conjugated polymers as highly efficient electron transporting/injection layer in optoelectronic devices.", *Chem. Soc. Rev.* **39**, 2500–21 (2010), DOI:10.1039/b907991m
138. Sax, S., Rugen-Penkalla, N., Neuhold, A., Schuh, S., Zojer, E., List, E. J. W. & Müllen, K.; "Efficient blue-light-emitting polymer heterostructure devices: the fabrication of multilayer structures from orthogonal solvents.", *Adv. Mater.* **22**, 2087–91 (2010), DOI:10.1002/adma.200903076
139. Tseng, S.-R., Li, S.-Y., Meng, H.-F., Yu, Y.-H., Yang, C.-M., Liao, H.-H., Horng, S.-F. & Hsu, C.-S.; "High-efficiency blue multilayer polymer light-emitting diode based on poly(9,9-dioctylfluorene)", *J. Appl. Phys.* **101**, 084510 (2007), DOI:10.1063/1.2721830
140. Fong, H. H., Lee, J.-K., Lim, Y.-F., Zakhidov, A. a, Wong, W. W. H., Holmes, A. B., Ober, C. K. & Malliaras, G. G.; "Orthogonal processing and patterning enabled by highly fluorinated light-emitting polymers.", *Adv. Mater.* **23**, 735–9 (2011), DOI:10.1002/adma.201002986
141. Scherf, U. & List, E. J. W.; "Semiconducting Polyfluorenes—Towards Reliable Structure-Property Relationships", *Adv. Mater.* **14**, 477–487 (2002), DOI:10.1002/1521-4095(20020404)14:7<477::AID-ADMA477>3.0.CO;2-9
142. List, E. J. W., Guentner, R., Scanducci de Freitas, P. & Scherf, U.; "The Effect of Keto Defect Sites on the Emission Properties of Polyfluorene-Type Materials", *Adv. Mater.* **14**, 374 (2002), DOI:10.1002/1521-4095(20020304)14:5<374::AID-ADMA374>3.0.CO;2-U
-

-
143. Woody, K. B., Nambiar, R., Brizius, G. L. & Collard, D. M.; "Synthesis and Properties of Amphiphilic Poly(1,4-Phenylene Ethynylene)s Bearing Alkyl and Semifluoroalkyl Substituents", *Macromolecules* **42**, 8102–8111 (2009), DOI:10.1021/ma901442j
144. Pogantsch, A., Gadermaier, C., Cerullo, G., Lanzani, G., Scherf, U., Grimsdale, A. C., Müllen, K. & List, E. J. W.; "Photophysics of poly(fluorenes) with dendronic side chains", *Synth. Met.* **139**, 847–849 (2003), DOI:10.1016/S0379-6779(03)00256-X
145. Grimme, J., Kreyenschmidt, M., Uckert, F., Müllen, K. & Scherf, U.; "On the conjugation length in poly(para-phenylene)-type polymers", *Adv. Mater.* **7**, 292–295 (1995), DOI:10.1002/adma.19950070310
146. Rehahn, M., Schlüter, A.-D. & Wegner, G.; "Soluble poly(para-phenylene)s, Variation of the length and the density of the solubilizing side chains", *Makromol. Chem.* **191**, 1991–2003 (1990), DOI:10.1002/macp.1990.021910902
147. Hintschich, S., Dias, F. & Monkman, a.; "Dynamics of conformational relaxation in photoexcited oligofluorenes and polyfluorene", *Phys. Rev. B* **74**, 045210 (2006), DOI:10.1103/PhysRevB.74.045210
148. Li, L. & Collard, D. M.; "Tuning the Electronic Structure of Conjugated Polymers with Fluoroalkyl Substitution: Alternating Alkyl/Perfluoroalkyl-Substituted Polythiophene", *Macromolecules* **38**, 372–378 (2005), DOI:10.1021/ma048510r
149. Liu, B., Yu, W.-L., Lai, Y.-H. & Huang, W.; "Blue-Light-Emitting Fluorene-Based Polymers with Tunable Electronic Properties", *Chem. Mater.* **13**, 1984–1991 (2001), DOI:10.1021/cm0007048
150. Facchetti, A., Yoon, M., Stern, C. L., Hutchison, G. R., Ratner, M. A. & Marks, T. J.; "Building blocks for N-type molecular and polymeric electronics. Perfluoroalkyl- versus alkyl-functionalized oligothiophenes (nTs; n = 2-6). Systematic synthesis, spectroscopy, electrochemistry, and solid-state organization.", *J. Am. Chem. Soc.* **126**, 13480–501 (2004), DOI:10.1021/ja048988a
151. Chen, S. H., Su, A. C., Su, C. H. & Chen, S. a.; "Crystalline Forms and Emission Behavior of Poly(9,9-di-n-octyl-2,7-fluorene)", *Macromolecules* **38**, 379–385 (2005), DOI:10.1021/ma048162t
152. Zhang, T., Deng, L., Wang, R., Zhou, W. & Li, J.; "Novel fluorene/trifluoromethylphenylene copolymers: Synthesis, spectra stability and electroluminescence", *Dye. Pigment.* **94**, 380–385 (2012), DOI:10.1016/j.dyepig.2012.01.019
153. Bertolucci, M., Galli, G., Chiellini, E. & Wynne, K. J.; "Wetting Behavior of Films of New Fluorinated Styrene-Siloxane Block Copolymers", *Macromolecules* **37**, 3666–3672 (2004), DOI:10.1021/ma035934x
154. Hayes, L. J.; "Surface energy of fluorinated surfaces", *J. Fluor. Chem.* **8**, 69–88 (1976), DOI:10.1016/S0022-1139(00)82900-0
155. Newby, C., Lee, J.-K. & Ober, C. K.; "The solvent problem: Redissolution of macromolecules in solution-processed organic electronics", *Macromol. Res.* **21**, 248–256 (2013), DOI:10.1007/s13233-013-1129-z
-

-
156. Lee, S., Park, J.-S. & Lee, T. R.; "The wettability of fluoropolymer surfaces: influence of surface dipoles.", *Langmuir* **24**, 4817–26 (2008), DOI:10.1021/la700902h
157. Krüss; "The Owens, Wendt, Rabel and Kaelble method", <http://www.kruss.de/en/theory/measurements/contact-angle/models/owrk.html>, (accessed October 20, 2013)
158. Lee, J.-K. *et al.*; "Semiperfluoroalkyl Polyfluorenes for Orthogonal Processing in Fluorous Solvents", *Macromolecules* **43**, 1195–1198 (2010), DOI:10.1021/ma902179s
159. Alvey, L. J., Meier, R., Soós, T., Bernatis, P. & Gladysz, J. A.; "Syntheses and Carbonyliridium Complexes of Unsymmetrically Substituted Fluorous Trialkylphosphanes: Precision Tuning of Electronic Properties, Including Insulation of the Perfluoroalkyl Groups", *Eur. J. Inorg. Chem.* **2000**, 1975–1983 (2000), DOI:10.1002/1099-0682(200009)2000:9<1975::AID-EJIC1975>3.0.CO;2-M
160. Giebeler, C., Whitelegg, S. a., Campbell, a. J., Liess, M., Martin, S. J., Lane, P. a., Bradley, D. D. C., Webster, G. & Burn, P. L.; "Optical studies of electric fields in poly(2-methoxy-5-ethyl (2^{sup}]-hexyloxy) para-phenylene vinylene) light-emitting diodes", *Appl. Phys. Lett.* **74**, 3714 (1999), DOI:10.1063/1.123238
161. Deng, X. Y., Lau, W. M., Wong, K. Y., Low, K. H., Chow, H. F. & Cao, Y.; "High efficiency low operating voltage polymer light-emitting diodes with aluminum cathode", *Appl. Phys. Lett.* **84**, 3522 (2004), DOI:10.1063/1.1739510
162. Niu, Y.-H., Ma, H., Xu, Q. & Jen, A. K.-Y.; "High-efficiency light-emitting diodes using neutral surfactants and aluminum cathode", *Appl. Phys. Lett.* **86**, 083504 (2005), DOI:10.1063/1.1865327
163. Huang, F., Niu, Y.-H., Zhang, Y., Ka, J.-W., Liu, M. S. & Jen, a. K.-Y.; "A Conjugated, Neutral Surfactant as Electron-Injection Material for High-Efficiency Polymer Light-Emitting Diodes", *Adv. Mater.* **19**, 2010–2014 (2007), DOI:10.1002/adma.200602967
164. Miller-Chou, B. a. & Koenig, J. L.; "A review of polymer dissolution", *Prog. Polym. Sci.* **28**, 1223–1270 (2003), DOI:10.1016/S0079-6700(03)00045-5
165. Kim, J.-S., Friend, R. H., Grizzi, I. & Burroughes, J. H.; "Spin-cast thin semiconducting polymer interlayer for improving device efficiency of polymer light-emitting diodes", *Appl. Phys. Lett.* **87**, 023506 (2005), DOI:10.1063/1.1992658
166. Van Dijken, a, Perro, a, Meulenkaamp, E. . & Brunner, K.; "The influence of a PEDOT:PSS layer on the efficiency of a polymer light-emitting diode", *Org. Electron.* **4**, 131–141 (2003), DOI:10.1016/j.orgel.2003.08.007
167. Wang, F., Wang, P., Fan, X., Dang, X., Zhen, C., Zou, D., Kim, E. H., Lee, D. N. & Kim, B. H.; "Voltage-controlled multicolor emitting devices", *Appl. Phys. Lett.* **89**, 183519 (2006), DOI:10.1063/1.2382747
168. Zhang, X. & Jenekhe, S. a.; "Electroluminescence of Multicomponent Conjugated Polymers. 1. Roles of Polymer/Polymer Interfaces in Emission Enhancement and Voltage-Tunable Multicolor Emission in Semiconducting Polymer/Polymer Heterojunctions", *Macromolecules* **33**, 2069–2082 (2000), DOI:10.1021/ma991913k
-

-
169. Berggren, M., Inganäs, O., Gustafsson, G., Rasmusson, J., Andersson, M. R., Hjertberg, T. & Wennerström, O.; "Light-emitting diodes with variable colours from polymer blends", *Nature* **372**, 444–446 (1994), DOI:10.1038/372444a0
170. Tasch, S., List, E., Hochfilzer, C., Leising, G., Schlichting, P., Rohr, U., Geerts, Y., Scherf, U. & Müllen, K.; "Efficient red- and orange-light-emitting diodes realized by excitation energy transfer from blue-light-emitting conjugated polymers", *Phys. Rev. B* **56**, 4479–4483 (1997), DOI:10.1103/PhysRevB.56.4479
171. Leising, G. *et al.*; "Efficient full-colour electroluminescence and stimulated emission with polyphenylenes", *Synth. Met.* **91**, 41–47 (1997), DOI:10.1016/S0379-6779(97)03972-6
172. Tasch, S. *et al.*; "Efficient white light-emitting diodes realized with new processable blends of conjugated polymers", *Appl. Phys. Lett.* **71**, 2883 (1997), DOI:10.1063/1.120205
173. Hu, B. & Karasz, F. E.; "Blue, green, red, and white electroluminescence from multichromophore polymer blends", *J. Appl. Phys.* **93**, 1995 (2003), DOI:10.1063/1.1536018
174. Wu, Y.-S., Hwang, S.-W., Chen, H.-H., Lee, M.-T., Shen, W.-J. & Chen, C. H.; "Efficient white organic light emitting devices with dual emitting layers", *Thin Solid Films* **488**, 265–269 (2005), DOI:10.1016/j.tsf.2005.04.032
175. Kuik, M., Nicolai, H. T., Lenes, M., Wetzelaer, G.-J. a. H., Lu, M. & Blom, P. W. M.; "Determination of the trap-assisted recombination strength in polymer light emitting diodes", *Appl. Phys. Lett.* **98**, 093301 (2011), DOI:10.1063/1.3559911
176. Nicolai, H. T., Hof, A. & Blom, P. W. M.; "Device Physics of White Polymer Light-Emitting Diodes", *Adv. Funct. Mater.* **22**, 2040–2047 (2012), DOI:10.1002/adfm.201102699
177. Anni, M., Lattante, S., De Kok, M. M., Cingolani, R. & Gigli, G.; "Intermolecular sequential energy transfer in thin films of a white emitting copolymer", *Appl. Phys. Lett.* **89**, 221903 (2006), DOI:10.1063/1.2387896
178. Gather, M. C., Alle, R., Becker, H. & Meerholz, K.; "On the Origin of the Color Shift in White-Emitting OLEDs", *Adv. Mater.* **19**, 4460–4465 (2007), DOI:10.1002/adma.200701673
179. Ponterini, G., Serpone, N., Bergkamp, M. A. & Netzel, T. L.; "Comparison of radiationless decay processes in osmium and platinum porphyrins", *J. Am. Chem. Soc.* **105**, 4639–4645 (1983), DOI:10.1021/ja00352a020
180. Papkovsky, D. B.; "New oxygen sensors and their application to biosensing", *Sensors Actuators B Chem.* **29**, 213–218 (1995), DOI:10.1016/0925-4005(95)01685-6
181. Higgins, R. W. T., Monkman, a. P., Nothofer, H.-G. & Scherf, U.; "Energy transfer to porphyrin derivative dopants in polymer light-emitting diodes", *J. Appl. Phys.* **91**, 99 (2002), DOI:10.1063/1.1419213
-

References

182. Cleave, V., Yahioglu, G., Le Barny, P., Hwang, D. H., Holmes, A. B., Friend, R. H. & Tessler, N.; "Transfer Processes in Semiconducting Polymer-Porphyrin Blends", *Adv. Mater.* **13**, 44–47 (2001), DOI:10.1002/1521-4095(200101)13:1<44::AID-ADMA44>3.0.CO;2-#
183. Trattig, R. *et al.*; "Deep blue polymer light emitting diodes based on easy to synthesize, non-aggregating polypyrene", *Opt. Express* **19**, A1281–93 (2011), DOI:10.1364/OE.19.0A1281